Multi-Wavelength Kinematics and Mass Modelling of the Spiral Galaxy NGC 6503

Modélisation Multi-Longueur d'Onde de la Cinématique et la Masse de la Galaxie Spirale NGC 6503

A Thesis Submitted

to the Division of Graduate Studies of the Royal Military College of Canada

by

Cameron Alexander Arsenault, BSc, RMC
Second Lieutenant

In Partial Fulfillment of the Requirement for the Degree of

Master of Science

April 2010

Your file Votre référence
ISBN: 978-0-494-64555-0
Our file Notre référence
ISBN: 978-0-494-64555-0

Acknowledgements

First and foremost, I would like to thank my thesis supervisor, Kristine Spekkens, for her support, guidance, and instruction over these last two years. I learned an incredible amount from her during our discussions about, but not limited to, my project. I would also like to thank her for giving me the opportunity to visit the Arecibo Observatory where I had the chance to "play" with the largest single aperture telescope ever constructed. I thank everyone in the RMC Astro group for the insightful discussions during our weekly meetings and subsequent decompressions. Thank you to Peter Teuben and Josh Simon for providing me with data for NGC 6503 in advance of publication. A big thanks to Michael McDonald for reducing our CFHT data for us and his patience in helping us with our surface brightness profile. I also have to thank my parents for their never-ending support for whatever I decide I want to do next. They taught me that I "can be anything I want to be" and "can do anything I want to do" before I even knew what they were saying. Finally, an innumerable amount of thanks has to be given to my fiancée Marie-Eve and her family. Her family has welcomed me into their home, encouraged me, and saved me from doing the dishes since I had to go and work. Marie-Eve's support through all my time here at RMC has been undying and although she says that doing a Masters is bad for a couple, I have only come to love her more.

Abstract

We perform in-depth kinematic, photometric, and mass studies of the nearby, late-type spiral galaxy, NGC 6503. First, using the publicly available velocity field code Velfit, we searched for coherent non-circular motions in our Hα, H I, and CO kinematic datasets. Once we were able to rule out significant radial or bisymmetric flows we combined the four datasets into a single, multi-wavelength, master dataset and constructed a rotation curve. Using the Canada-France-Hawaii Telescope Wide-field Infrared Camera observations in the K-band, to minimize effects from dust and to trace the old stellar population to the edge of the optical disk, a 1-D surface brightness profile for NGC 6503 was constructed. This profile was used to define the mass contribution from the stellar disk. Using the multi-wavelength kinematics, the stellar contribution to the rotation curve, and gas rotation data, we performed mass models for Isothermal, Hernquist, and NFW dark matter halo profiles. Although the Isothermal profile provided the best fit to the data, the analytical Hernquist profile and the cosmologically motivated NFW halo are also allowed. The best-fitting values for the NFW halo parameters were found to be $c = 25.45 \pm 2.35$ and $V_{200} = 65.25 \pm 1.30$ $\mathrm{km\,s^{-1}}$. In contrast to the low values found by large surveys of galaxies, this value of c (for a given V_{200}) is higher than predicted by current cosmology and we consider it an upper limit for NGC 6503. Each of the dark matter profiles solved for the mass-to-light ratio (m_d) as a free parameter and gave $m_d = 0.138 \pm 0.022$, 0.127 ± 0.011, and 0.116 ± 0.014 $M_\odot/L_{\odot,K}$ for the Isothermal, Hernquist, and NFW profiles respectively. Comparing this to the maximum disk mass-to-light ratio, $m_d = 0.268$ $M_\odot/L_{\odot,K}$, we find that in all cases a submaximal disk is strongly preferred for NGC 6503.

Résumé

Nous effectuons une étude approfondie de la cinématique, de la photométrique et de la masse de la galaxie spirale proche NGC 6503. Premièrement, à l'aide du logiciel public Velfit, nous avons cherché des mouvements non circulaires cohérents dans nos données cinématiques Hα, H I, et CO. Une fois les écoulements radiaux et bisymmétriques exclus, nous avons combiné les quatre groupes de données pour former un ensemble de données multi-longueur d'onde maître et construire une courbe de rotation. Un profil 1-D de la brillance de surface de NGC 6503 a été construit, en utilisant des observations du Wide-Field Infrared Camera dans la bande K obtenues avec le télescope Canada-France-Hawaii afin de minimiser les effets de la poussière et pour tracer la vieille population stellaire jusqu'au bord du disque optique. Ce profil a permis de définir la contribution du disque stellaire á la masse. à l'aide de la cinématique multi-longueur d'onde, de la contribution stellaire à la courbe de rotation, et des données pour la rotation du gaz, nous avons effectué des modèles pour la masse, incluant des profils Isotherme, Hernquist et NFW pour la matière sombre. Bien que le profil Isotherme ait produit le meilleur ajustement, le profil analytique Hernquist et le halo NFW motivé par la cosmologie sont aussi permis par les données. La meilleure régression pour le halo NFW a des valeurs $c = 25,45 \pm 2,35$ et $V_{200} = 65,25 \pm 1,30$ km s^{-1}. En contraste avec les valeurs basses trouvées par de grands relevés de galaxies, cette valeur de c (pour une valeur donnée de V_{200}) est plus grande que prévu par la cosmologie courante, et nous la considérons comme une limite supérieure pour NGC 6503. Chacun des profils de la matière sombre possède le rapport masse-lumière (m_d) comme paramètre libre. Les solutions possèdent m_d = 0,138±0,022, 0,127±0,011, et 0,116±0,014 $M_\odot/L_{\odot,K}$ pour les profils Isotherme, Hernquist et NFW respectivement. En comparant ceci au rapport masse-lumière maximal, m_d = 0,268 $M_\odot/L_{\odot,K}$, nous trouvons que, dans tous les cas, un disque sous-maximal est fortement préféré pour NGC 6503.

Contents

List of Figures

List of Tables

1 Chapter 1 - Introduction

A galaxy is a large, gravitationally bound, astronomical object which consists of several individual components. Generally, a galaxy can be separated into a stellar (and stellar remnants), dust and gas, and a dark matter (matter that is inferred indirectly to exist from gravitational effects on visible matter and radiation, yet so far undetected by emitted or scattered electromagnetic radiation) component. Historically galaxies are classified according to their apparent shape and visible features. One common type of galaxy is the spiral galaxy, which is traditionally recognized by its disk shape and spiral arms. Fig. 1 shows an example of a spiral galaxy and how one can separate it into its different components. First, shown in blue, there is a rotating disk of stars and interstellar medium (the matter that is found between the star systems within a galaxy). Part of the disk structure, shown as the curved lines emerging from the centre of the galaxy in Fig. 1, is the spiral arms of the galaxy. Also part of the disk of a galaxy is the gas disk, consisting of the atomic and molecular gas. Neutral hydrogen, the most prominent atomic gas in the disks of galaxies, often extends well beyond the stellar disk, and therefore is shown in green in Fig. 1. A spiral galaxy also may or may not contain a significant bulge, which usually contains an older stellar population than the disk. This is shown as the yellow component in Fig. 1. Spherical collections of old stars, known as globular clusters, are often found in the halo (orbiting a galactic core). These spherical collections of stars are shown as the brown spheres scattered away from the disk in Fig. 1. Finally, the dark matter halo, which extends beyond the edge of the visible galaxy and dominates the mass of the system, is shown as the encompassing red sphere in Fig. 1.

A visible light image for the Sombrero Galaxy (M104), seen in Fig. 2, is another good example to show the separate components of a spiral galaxy. The orientation of M104 on the sky allows us to clearly see its disk and the spiral structure in that disk. It shows a bright central component in the centre of the disk: the bulge. M104 is particularly rich in globular clusters and this stellar halo can be seen in Fig. 2 as, and within, the glow encompassing the galaxy. Not seen in this visible image of M104 are the gas components of the disk, which extend beyond that of the stellar disk, and

Figure 1 Schematic of a spiral galaxy. The blue portion represents the rotating stellar disk, including spiral arms. The green represents the gas disk for this galaxy. The yellow central component gives an example of a bulge. Globular clusters are shown in brown in the galaxy halo, orbiting the central core. Finally, the dark matter halo is shown in red.

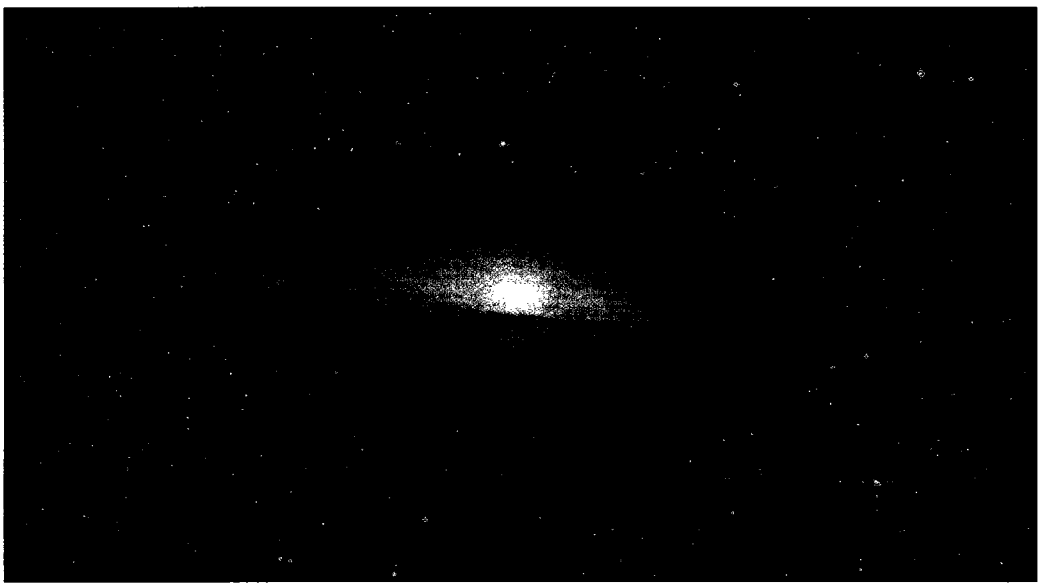

Figure 2 The Sombrero Galaxy is a good candidate to visually demonstrate the different components of a galaxy. Here we can clearly see the disk, bulge, and stellar halo present in M104. NASA/ESA and The Hubble Heritage Team (STScI/AURA)

the dark matter halo.

Understanding the different components of a galaxy is important because it allows us to break down the galaxy into its constituents and constrain the properties of those we do not understand. The dark matter halo, for example, contributes a large portion of the mass of a galactic system, but the nature of the halo itself is not well understood. This thesis aims to use the observed properties of the disk (stars and gas) of a nearby galaxy, NGC 6503, to constrain the properties of its dark matter halo.

The standard model of Big Bang cosmology attempts to explain the structure of the Cosmic Microwave Background[1] (CMB), distribution of elements in the Universe, large scale structure of galaxy clusters, and the accelerating expansion of the Universe. The simplest theory, and the one in general agreement with observations, is known as Lambda-Cold Dark Matter (ΛCDM). This model assumes a Universe which is isotropic (looks the same in all directions), homogenous (looks the same from every direction), and expanding. The model traces the origins of the Universe back to a single originating event, the Big Bang, which is the point in time when the Universe began to abruptly expand. $10^{-}36$ seconds after the Big Bang, an exponential expansion of space known as cosmic inflation. It is through this inflation that we are able to describe the relative abundances of the lighter elements in the universe, the slight irregularities in the CMB, and the continuing expansion of the Universe.

The simplest standard cosmological model is based on six parameters, three of which describe densities of the constituents of the Universe. The current Wilinson Microwave Anisotropy Probe (WMAP; Komatsu et al., 2009) analysis finds that dark energy (the hypothetical energy which permeates all of space and increases the rate of expansion of the Universe; Peebles and Ratra, 2003) make up 72.6 percent of the Universe, baryons make up 4.56 percent, and cold dark matter makes up 22.8 percent. This cold dark matter is the type of matter necessary to account for gravitational effects observed in the Universe, which cannot be explained by the amount of currently observed matter. The main properties of dark matter in the standard model is that it is non-relativistic, possibly consisting of matter other than protons and neutrons,

[1] electromagnetic radiation coming from all directions in the universe, considered to be the remnants of the big bang

not able to be cooled by radiating photons, and only interactive with with other particles through gravity (and not through collisions). Possible candidates for cold dark matter include axions (a hypothetical elementary particle), sterile neutrinos (a hypothetical neutrino), Weakly Interacting Massive Particles (WIMPs), neutralinos (hypothetical particle predicted by supersymmetry), or Massive Astrophysical Compact Halo Objects (MACHOs). Although no widely supported direct detections of dark matter have occurred, it is generally accepted that dark matter is needed in the Universe.

1.1 Kinematics and Masses of Spiral Galaxies

Spiral galaxies are disk galaxies with ongoing star formation. Together with irregular galaxies, spirals make up approximately sixty percent of galaxies in the Universe (Loveday, 1996). In general, most of the mass in an unbarred spiral galaxy is contained in its disk components (consisting of a flat rotating disk of stars, gas and dust) and a dark halo component[2]. Because the disk is rotationally supported[3] by the halo, observations of the disk kinematics place constraints on both the disk and halo structure in spiral galaxies.

By observing specific features in the spectra of spiral galaxies (a spectrum refers to the distribution of energy with wavelength or frequency from the observed source) we are able to measure radial velocities (with respect to us, the observer) across a resolved galaxy. For example, we can derive radial velocities through the observation of the spin flip spectral line of neutral hydrogen (H I), whose rest frame wavelength is 21 cm ($\sim$ 1420 MHz). Using Eq. 1 we can compare the observed wavelength of this feature to its rest wavelength, thereby resulting in a radial velocity. In Eq. 1 ν_0 is defined as the frequency of emission in the rest frame of the source (ν_0 = 1420 MHz for H I), ν is the frequency at which it is observed, c is the speed of light, and $V_{doppler}$ is therefore the Doppler shift in velocity units.

$$\frac{V_{doppler}}{c} = \frac{\nu_0 - \nu}{\nu} \tag{1}$$

[2]In spirals such as NGC 6503 studied here, the mass contributions from the bulge and halo is negligible

[3]Since dark matter halos are actually triaxial rather than spherical, the torque of the uneven distribution of mass can therefore give rise to angular momentum.

This Doppler shift is the velocity at which the source is moving away from us along the line-of-sight. For a well-resolved galaxy, these measurements can be taken at points all over the observable galaxy giving a map of radial velocities. These radial velocities are a combination of the systemic velocity of the galaxy, caused by the uniform Hubble expansion (the observation that the velocity at which various galaxies are moving away from us is proportional to the distance to us) of the Universe, and the component of velocity in the rotating disk that projects along the line-of-sight. Once the systemic velocity is subtracted from the measured radial velocities, the rotation of the galaxy can be measured: (see part C of Fig. 3). One side of the galaxy will have velocities moving away from us and the other will have velocities coming towards us, thereby implying rotation. Examples of this Doppler shift, not only for the the H I (21 cm) line, but also for the optical Hα (656.3 nm) and millimetre CO (2.6 mm) transitions can be seen for NGC 6503 in our data in Figs. 9, 10, 11, and 12.

Once we have the line-of-sight velocities across a galaxy's disk we can derive its circular velocity for a given distance from the centre. If we assume that the components of the disk are rotating around the centre in circular orbits we can define the geometry of the system as in see Fig. 3. Take a given point in the plane of the galaxy's disk to have components r and θ, and a given point in the projected (what the observer sees) plane to have components s and α; we can relate them through:

$$r = s[1 + \sin^2(\alpha)\tan^2(i)]^{1/2} \tag{2}$$

$$V_t(r) = \frac{V_{los}(s,\alpha)(\cos^2(i)\tan^2(\alpha))^{1/2}}{\sin(i)\cos(i)} \tag{3}$$

$$V_{los}(s,\alpha) = V_t(r)\cos(\theta)\sin(i) \tag{4}$$

Eq. 3 shows the mathematical conversion between a point in the projected plane (with coordinates s and α) to those in the plane of the observer (with coordinates r and θ). Eq. 4 is the inverse, in that it translates a point in the galaxy's plane to the plane projected at an inclination i on the sky [i is measured from the ellipticity of the disk by $\epsilon = 1 - \cos(i)$]. Below, $V_t(r)$ is the circular velocity in the disk and $V_{los}(s,\alpha)$ is the

measured line-of-sight velocity. The function $V_t(r)$ is called the rotation curve of the system and traces the mass distribution (see below). Fig. 3 further illustrates these points by showing that, for a galaxy which is inclined at some angle i (parts C and D) with respect to the observer, one side of the galaxy will be redshifted (velocity component moving away from us) and the other blueshifted (velocity component moving towards us). Using Eqns. 2 and 3 in an axisymmetric, inclined galaxy $V_t(r)$ can be derived from the measured radial velocities at a series of (s,α). This rotational velocity with respect to radius is therefore the rotation curve for the galaxy.

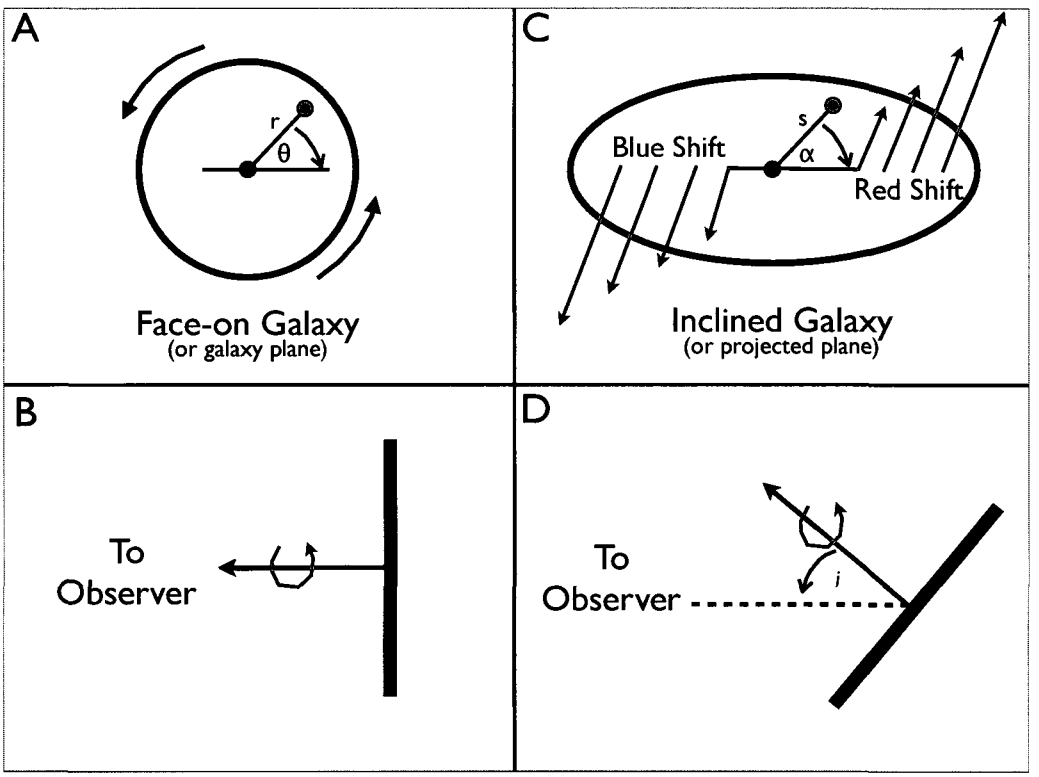

Figure 3 Cartoon showing the relationship between the galaxy and projected planes. Parts A and B demonstrate the galaxy plane or a galaxy that is face on to an observer. In this plane a given point has components r and θ and has no component of rotation towards or away from us. Parts C and D show the projected/observed plane for a galaxy. In this plane a given point has components s and α. Part C demonstrates how an inclined galaxy's circular velocity can be represented by radial velocities in the form of Doppler shifts.

In addition to velocity measurements, photometric analyses (the measurement of the flux or intensity of an astronomical object's electromagnetic radiation) of spiral galaxies are extremely useful. Generally we can determine how the brightness of a galaxy varies with radius through the fitting of concentric ellipses on 2-D photometric

observations. For an axisymmetric galaxy, a 1-D surface brightness profile is then constructed from these ellipses of equal intensity. This surface brightness profile is typically exponential, such that as the distance from the centre of the galaxy increases, the surface brightness decreases exponentially. A multitude of information about a galaxy's stellar disk can be acquired from the surface brightness profile, such as the luminosity (the amount of electromagnetic energy an object radiates per unit time), variations in age and metallicity (the amount of chemical elements other than hydrogen and helium), presence of a bulge, and the possible presence of dust. Similarly, observations of the gas in the galaxy constrain its surface brightness density distribution. Using luminosity as a tracer of the stellar and gas mass, the photometric analyses allow us to constrain the properties of the disk.

For a system in equilibrium, the centripetal acceleration of each orbit equals the gravitational acceleration at that radius. The kinematics of the disk trace the total (disk and halo) mass of the system. The relationship between velocity and mass is therefore given by:

$$\frac{mV_t(r)^2}{r} = \frac{GM_r m}{r^2} \tag{5}$$

$$M_r = \frac{V_t(r)^2 r}{G} \tag{6}$$

Here $V_t(r)$ is the circular or rotation velocity at a given radius r, M_r is the mass within that radius, m is a test mass at r, and G is the gravitational constant.

It should be noted that the equations presented above hold only for circular orbits in a spherically symmetric mass distribution, but the scaling relation between mass and velocity is conserved for the disk case as well. If all of the mass in the spiral galaxy were contained in the disk, Eq. 6 predicts a Keplerian fall-off beyond the disk edge: $V_t \propto \sqrt{r}$ (M_r constant). This "falling" rotation curve is depicted as the dashed line A in Fig. 4. Instead, rotation curves remain flat as the distance from the centre of the galaxy increases; an example of this, for illustration purposes only, is the solid line B of Fig. 4. This extended rotation curve is therefore representative of a significant amount of mass eluding observation according to Eq. 6. This turns out to be one of the strongest lines of evidence for the need of dark matter in the Universe

today (Rubin et al., 1980; Bosma, 1981). The mass of the system is comprised not just of the stellar constituents, but also a significant and invisible dark matter halo.

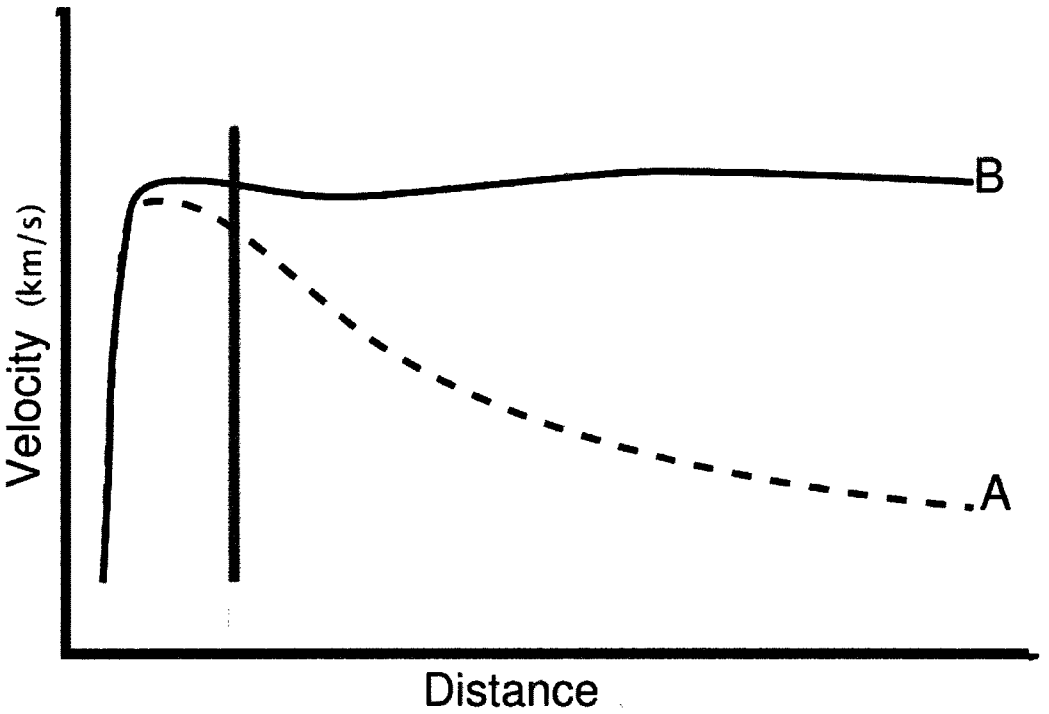

Figure 4 Cartoon of an observed rotation curve versus the expected rotation curve from Keplerian dynamics. The solid line B shows an example of an extended rotation curve that is typical of observations. The dashed line A shows a Keplarian fall off expected if all of the mass is contained within the stellar disk. The vertical line indicates the edge of the optical disk.

Knowing that the mass of the system is comprised of a significant dark matter halo as well as the previously mentioned components (bulge, disk, gas, and dark matter component), we can carry out mass modelling of its rotation curve in order to determine how each of the components present in the galaxy contributes to this total mass. For systems where the disk and halo dominate the mass distribution, we may write:

$$M_t(r) = M_g(r) + M_d(r) + M_u(r) \tag{7}$$

where $M_g(r)$ is the mass of the gas, $M_d(r)$ is the mass of the disk, $M_u(r)$ is the mass of the dark matter halo, and $M_t(r)$ is the total mass. Each of these components contributes to the total mass budget for the system, and can also be expressed in

velocity units through Eq. 6. These velocities are not the representative of the circular motion of each component of the galaxy, but rather the mass of that component's contribution to the observed rotation curve:

$$V_t(r) = \sqrt{V_g(r)^2 + \Psi\, V_d(r)^2 + V_u(r)^2} \tag{8}$$

where $V_t(r)$ is the total velocity, $V_g(r)$ is the velocity contribution by the gas, and $V_u(r)$ is the dark matter velocity component. Ψ is a dimensionless scaling factor such that $\frac{m_d}{\Psi} = 1 M_\odot / L_{\odot,X}$, where m_d is the mass-to-light ratio in the photometric band X.

Mass modelling therefore allows us to quantify the mass contributions not only of the gas and stellar disk, but also that of the dark component. Expanding upon the cartoon shown in Fig. 4, Fig. 5 shows the same rotation curve broken down into the aforementioned components. In Fig. 5 the red curve shows the contribution to mass implied by $V_t(r)$ from the stellar disk, the green from the gas, and the blue from the dark matter halo. In mass modelling, the quadratic sum of these components using Eq. 8 aims to reproduce the solid black curve B from observations. The observed kinematics of the disk allow us to measure $V_t(r)$, the rotation curve. The observed photometry of the disk allows us to compute $V_g(r)$ and $V_d(r)$ from the distribution of gas and stars, respectively. Mass modelling allows us to constrain the mass-to-light ratio, m_d, and the free parameters of the dark matter halo profile, $V_u(r)$, given the measured properties of the disk.

1.2 Non-Circular Motions

Although the process described above seems straightforward to execute, there are several fundamental challenges with some of the basic assumptions. One of these arises from the derivation of rotation curves. Although Eq. 4 assumed that the motions in the disk are purely circular, this is not necessarily the case. If there are significant (or even minor) deviations from circular orbits in the disk, the mass estimates described above may be biased. Non-circular motions must therefore be accounted for and corrected before mass modelling. We have known since Bosma (1978) that these non-circular motions could be driven by bar-like or oval distributions. This is concern-

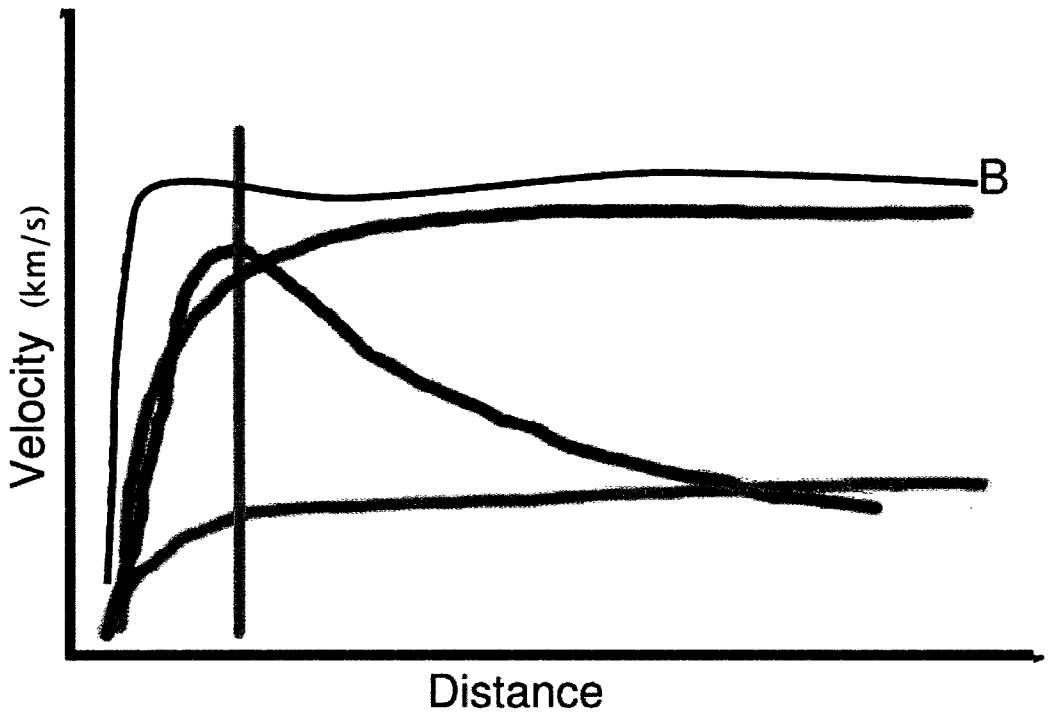

Figure 5 An extension of Fig. 4 such that the observations (solid black line) are decomposed into example components. The red curve shows the contribution to the mass represented by the rotation curve from the stellar disk. The green curve represents the contribution from the gas data. Finally, the blue curve shows an example of a contribution that could come from a dark matter halo.

ing since fifty to seventy percent of luminous spiral galaxies possess these elongated stellar structures in their central regions (Barazza et al., 2008). The non-circular motions can be especially significant at small radii since they may represent a significant fraction of the gravitational potential and since the contributions from circular and non-circular motions combine in quadrature (Valenzuela et al., 2007). From this we can conclude that a comprehensive study of the structure of disk galaxies requires a constraint on the non-circular motions in the disk.

Tools to probe galaxies for non-circular motions have been present since Schoenmakers et al. (1997) and Schoenmakers and Swaters (1999) introduced RESWRI as an extension of ROTCUR in the Gipsy software package (Van der Hulst et al., 1992). These tools have been extensively used to check kinematic data for non-circular motions, but it is difficult to interpret the code outputs and to correct for the motions that are found. Spekkens and Sellwood (2007) introduced a new and alternative tool, Velfit, for estimating the rotational velocities by fitting for non-circular streaming flows caused by distortions from bar-like flows. A detailed explanation of this tool is given in §3.2. Through the use of this tool we can hope to acquire the necessary constraints on the non-circular motions in order to perform accurate mass models.

1.3 Mass-to-Light Ratios and the Maximum Disk

The next major uncertainty in mass modelling is the accurate determination of the mass-to-light ratio, m_d (Eq. 8). In order to reliably model the luminous matter's contribution to the overall mass of the system (as represented by the observed rotation curve) we must have a good estimate of the stellar mass distribution. The fundamental difficulty with this is that most of the light is emitted by the few stars that are extremely bright, whereas the mass is dominated by the many low-luminosity stars that are too faint to detect. Fig. 6 (Sparke and Gallagher, 2007) gives an example of this in the V band. Fig. 6 presents the number, mass and luminosity densities of nearby stars as a function of absolute magnitude[4] from -5 $< M_v <$ 15.

There are a few things that we can immediately see from Fig. 6 and the solar neighbourhood in general. Most stars in the area are intrinsically faint. Absolute

[4] A logarithmic measure of intrinsic brightness of an astronomical object. Lower numbers indicate brighter objects and larger number indicate fainter ones.

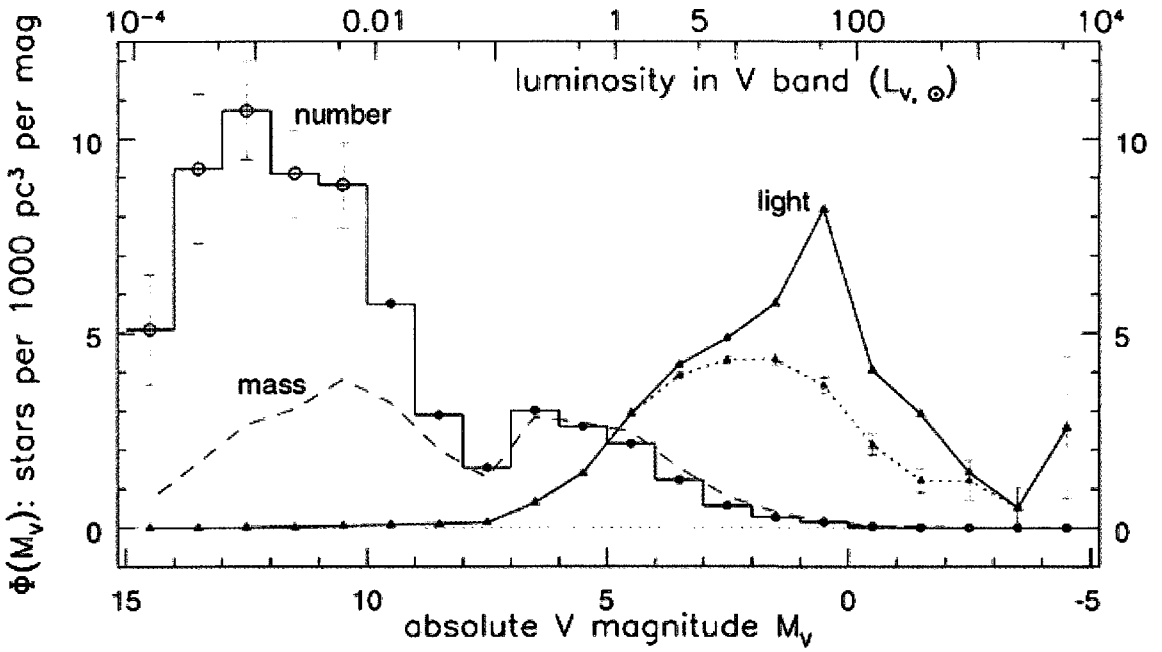

Figure 6 Fig 2.3 from Sparke and Gallagher (2007) and references therein. The histogram shows the luminosity function $\Phi(M_V)$ for nearby stars. Lines with triangles show $L_V\Phi(M_V)$, light from stars in each magnitude bin; the dotted curve is for main-sequence stars alone, the solid curve for all stars. The dashed curve gives $\mathcal{M}\Phi_{MS}(M_V)$, the mass in main sequence stars. Units are $L_\odot$ or $\mathcal{M}_\odot$ per 10 pc cubed; vertical bars show uncertainty, based on numbers of stars in each bin.

magnitudes 12 to 15 have by far the highest stellar density for a given M_V, $\Phi(M_V)$. Most of the light on the other hand is contributed by the intrinsically luminous stars, even though they are the most rare. Finally, most of the stellar mass density in the solar neighbourhood is contributed by the intrinsically low mass stars mentioned earlier. Much of the dynamics of galaxies are therefore dominated by stars which are often inconspicuous in the observed light, whereas those that are dominate the observed light actually contribute very little to the gravitating mass. For these reasons alone it should be clear that a well defined mass-to-light ratio is crucial in properly modelling the mass in galaxies. The next question to ask is how we can accurately determine this quantity. Generally this is done through either the analysis of stellar populations or through mass modelling itself.

Bell and de Jong (2001) show us through the use of simplified spiral galaxy evolution models, under a universal initial mass function (IMF), that stellar mass-to-light ratios (m_d) in all optical and near-infrared bands correlate strongly with galaxy colour. This is an expected result since stellar population models tell us that the

star formation and chemical abundance history determine both m_d and the galaxy colours. This relation is especially useful in the near-infrared since in these bands the data traces the older stellar populations (which contain most of the mass). The near-infrared wavelengths are also the least affected by dust obscuration (Bell and de Jong, 2001).

Attempts have also been made to constrain the mass-to-light ratio through mass models as defined by Eq. 8. In practice, however, the dark matter halo profile can be adjusted to compensate for any change in m_d without affecting the quality of the fit (van Albada et al., 1985). For these reasons, the disk and halo contributions to mass models are almost completely degenerate. Given the uncertainties in m_d from both stellar population methods and mass models, the standard practice is to fix m_d to a constant in mass models. One obvious lower limit is $m_d = 0$, that the disk mass is insignificant compared to that of the dark matter (for example, in Fig. 5 the red curve would not exist and the rotation curve would be completely described by the blue line). An upper limit can be defined when m_d yields a stellar contribution that matches, but does not exceed, the rotation curve data (in Fig. 5 this would mean that the blue curve would be minimized and the rotation curve would be almost entirely described by the red curve). This assumes that the inner portions of galaxies contain little dark matter. These maximum disk mass-to-light ratios were historically implemented as a solid limit in the attempt to break the degeneracy found between the stellar disk and mass model parameters. Some authors, when defining a maximum disk, leave room for a dark matter contribution such that even for a maximum disk case the disk may only contribute approximately 84% of the observed velocity (Sackett, 1997). Others leave no room for a dark matter component and consequently fit disk-only models as far out as possible (Palunas and Williams, 2000).

Whether or not galaxy disks are maximal is still debated. Using fluid dynamical models of gas flow to model a two-dimensional velocity field of barred galaxies, Weiner et al. (2001) find that their models are in need of $80-100\%$ maximum disk m_d ratios. A survey of 74 spiral galaxies by Palunas and Williams (2000) concluded that 75% of their sample have rotation curves that can be entirely accounted for by baryons (down to 23.5 magnitudes). Those that are not described entirely by baryons exhibit

non-axysymmetric structures. On the other hand, Courteau and Rix (1999) showed that the residuals in the Tully-Fisher relation (the correlation of a galaxy's maximum velocity with luminosity via $L \propto V_{max}^{\alpha}$ where $\alpha \approx 3 - 4$), at a fixed luminosity, are essentially uncorrelated with the residuals in the size-luminosity relation, also at fixed luminosity. In other words, the Tully-Fisher relation is independent of surface brightness and that implies that the size of a given disk with a fixed luminosity is not related to its rotation velocity. Courteau and Rix (1999) therefore conclude that on average high surface brightness galaxies are submaximal (the disk only contributes slightly to the observed rotation velocity).

Although different authors obtain contradicting results regarding the degree at which a disk is submaximal, it has been widely recognized that one cannot treat a high surface brightness (HSB) galaxy the same as a low surface brightness (LSB) galaxy in this context. The radius at which the dark matter begins to contribute significantly to the galaxy is smaller for LSB galaxies (De Blok and McGaugh, 1997). Authors have shown this by adopting a stellar m_d ratio at a given radius and evaluating the mass discrepancy of galaxy disks or a similar quantity. Although minor details may vary, most authors agree that the radius where dark matter dominates over stellar matter is much smaller for LSB galaxies.

Since uncertainties on m_d translate into uncertainties on the halo profile extracted from mass models (Eq. 8), constraining m_d is a key step in measuring spiral galaxy structure.

1.4 Theoretical Predictions

Detailed observations of the CMB, large-scale galaxy distances, and type 1A supernovae (the results of the violent explosion of a white dwarf star) have led to a "standard" cold dark matter (*Lambda*CDM) cosmological model that specifies the composition of the Universe and the initial conditions from which structure forms (Komatsu et al., 2009). In this model, the matter density in the Universe is dominated by a cold, collisionless dark matter component, which drives the growth of structure. High-resolution simulations of the evolution of this dark matter component under the influence of gravity yield predictions for the structure of dark matter halos that

exist today. Recently there has been significant progress in the prediction of the properties of dark matter halos in the *Lambda*CDM paradigm. Collisionless N-body simulations yield an approximately "universal" profile shape that can be described by simple fitting parameters. Simulations predict a cuspy profile, such that at inner radii (r) the density goes as:

$$\rho(r) \propto r^{-\alpha} \tag{9}$$

where $\alpha \sim 1$ (see below). One such analytic dark matter profile, which is still popularly used now, is that described by Navarro et al. (1997, hereafter NFW):

$$\rho_{NFW}(r) = \rho_{crit} \left(\frac{\delta_0(c)}{cr/r_{200}(1 + cr/r_{200})^2} \right) \tag{10}$$

where $\rho_{crit} \approx 5 \times 10^{-30} \mathrm{gcm}^{-3}$ is the critical density of the Universe given $\rho_{crit} = \frac{3H^2}{8\pi G}$ (where H is the Hubble parameter), c (not to be confused with the speed of light) is the concentration of the halo, δ_0 is the characteristic overdensity (which is a function of c) as defined by $\delta_0(c) = \frac{200}{3} \left(\frac{c^3}{\ln(1+c) - c/(1+c)} \right)$, and r_{200} is the radius inside which the mean density is $200\rho_{crit}$. A velocity parameter, V_{200} at the radius r_{200}, is related to r_{200} by $r_{200} = \frac{V_{200}}{10H}$.

Adopting the standard cosmology with H=70 $\mathrm{km\,s^{-1}Mpc^{-1}}$, the NFW profile therefore has 2 free parameters; here we use V_{200} and c. Since α=1 in Eq. 9, the NFW profile predicts a density profile with a "cusp" at the centre of galactic dark matter halos.

Whether or not galaxy observations are consistent with a cusp is still under debate. Many studies show evidence that dark matter halos do not show a cuspy centre but rather "cores" where the inner profile has little to no dependance on r. Other observations find values of $\alpha \leq 0.5$. For example, Salucci (2001) analysed a set of 137 dark matter dominated galaxies, concluding that halos have cores larger than the corresponding disk scale-lengths. Despite this apparent conflict between theory and observations it is still uncertain whether halo shapes are in fact cored, or if a cusp can be reconciled by taking observational errors and model parameter degeneracies into consideration (Swaters et al., 2003; Rhee et al., 2004; Spekkens et al., 2005).

Examples of observational errors include beam smearing (underestimation of the inner part of the rotation curve due to H I emission being smeared out from the finite beam size of the telescope) or misposition of the slit in the case of long-slit observations. The possible resolution of these problems can arise from the combination of high resolution datasets and the use of two-dimensional velocity fields. Non-circular motions, such as those described in §1.2, can represent a substantial fraction of the inner portions of the rotation curve. These are especially important when on the same order of magnitude as the rotational velocity itself (Simon et al., 2005). As discussed in §1.3 the acquisition of an accurate stellar mass is crucial. For HSB galaxies, where submaximal disks are found (Courteau and Rix, 1999), dynamically significant fractions of dark matter could result in steep cusps.

N-body simulations also make predictions for the value of c in halos of different masses. The NFW parameters c and V_{200} are correlated (Navarro et al., 1997), which is expected cosmologically: halos with larger values of c have lower values of V_{200} since halos with higher masses virialize at earlier times, when the average density of the Universe was higher.

McGaugh et al. (2007) studied 60 galaxies spanning a range of mass and Hubble type and carried out mass models assuming a maximum disk. Their sample of galaxies had only minor non-circular motions and they used only the intermediate to large radii where the non-circular motions that are present would be less significant. Observational errors due to slit alignment were not an issue due to two-dimensional velocity fields being used for all cases. They find that the c and V_{200} values obtained do not coincide well with those predicted by *Lambda*CDM simulations as illustrated in Fig. 7. The theoretical values to which McGaugh et al. (2007) compare their work to are the *Lambda*CDM models of Tegmark et al. (2004) and the WMAP 3 year results (Spergel et al., 2006). Slight changes in all of the relevant parameters in the WMAP 3 cosmology tend to lower the values of the concentration parameter (in relation to those of Tegmark et al., 2004) but essentially they follow the same trend. Also included in Fig. 7, in grey and blue, are the ranges of parameter values from mass modelling for the different m_d estimators [blue is where the m_d was estimated from stellar populations and grey is where the m_d was taken from the mass discrepancy-acceleration relation

(McGaugh, 2005)]. The problem with the predictions versus observations here is not so much with the mean concentration, but rather the run of concentration with halo mass. For low mass halos (low V_{200}), the values of the concentration parameter are acceptable (more or less in agreement with predictions) but becomes more discrepant as V_{200} increases. Taking into consideration the effect of adiabatic contraction (a simple prescription that describes the impact of galaxy formation on dark matter halos; Blumenthal et al., 1986) only lowers the value of c, pulling it further away from the theoretical values. McGaugh et al. (2007) go through possibilities for resolving this discrepancy, but come to no concrete conclusion. If disks are maximal as suggested by several lines of evidence (§1.3), then spiral galaxy dark matter halo densities are significantly lower than predicted by *Lambda*CDM.

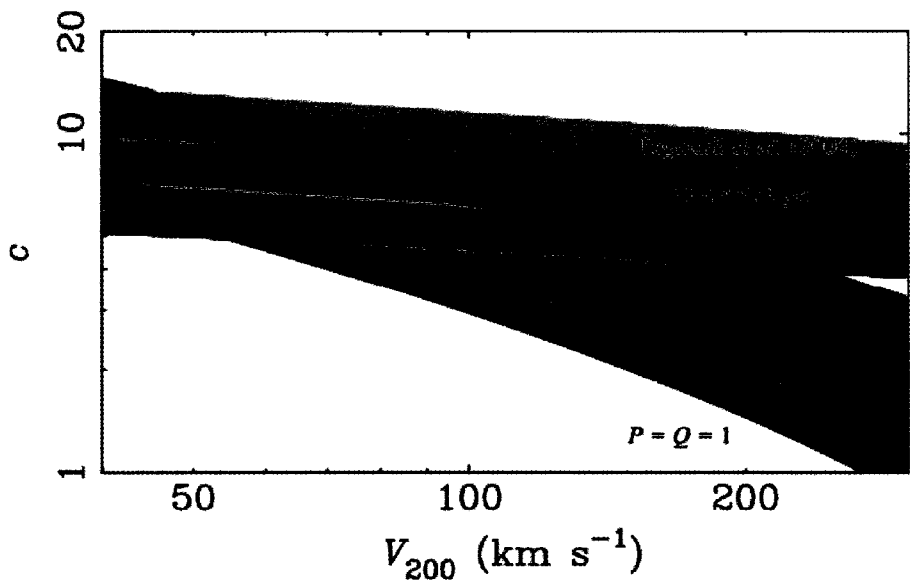

Figure 7 Figure 10 from McGaugh et al. (2007) showing the modelled values for two m_d estimators (blue for the stellar population estimator and grey for the mass discrepancy-acceleration relation estimator) compared to the predicted values of the NFW parameters c and V_{200} (in orange and red for the Tegmark et al. (2004) and WMAP 3 year (Spergel et al., 2006) cosmologies respectively). In all cases the width of the bands is representative of $\pm 1\sigma$. The predicted bands assume an intrinsic scatter of $\sigma_c = 0.14$ (Bullock et al., 2001).

1.5 Making Progress with NGC 6503

With the understanding of the current situation in spiral galaxies presented in Sections 1.1 1.2, 1.3, and 1.4 we perform mass modelling on NGC 6503. NGC 6503

is an ideal target since it is a (relatively) isolated galaxy with apparently minimal non-circular motions. The key science goals of this thesis are to measure a reliable rotation curve, explore the extent to which m_d can be constrained through mass models, and given this constraint on m_d, determine whether the halo profile in NGC 6503 is consistent with *Lambda*CDM predictions.

In this thesis we perform an in-depth search for non-circular motions in our H I, Hα, and CO datasets for NGC 6503, using Velfit (see §1.2). Once we are sure that significant non-circular motions are not present in any of them, we combine them to make a master, multi-wavelength dataset which defines the rotation curve for NGC 6503. Using recently acquired near-infrared K-band data, which traces the old stellar populations, we construct a surface brightness profile for the galaxy and use it to define the rotation contribution from the stellar disk. Using the multi-wavelength rotation curve, the rotational component from the stellar disk, and gas rotation we perform mass models on NGC 6503. Mass modelling the dark matter halo with the Isothermal, Hernquist, and NFW profiles, we attempt to constrain values for the mass-to-light ratio m_d and the halo parameters.

Information about NGC 6503 and the datasets used during the course of this thesis are presented in §2. A detailed search for non-circular motions in each of the datasets is presented in §3. The processing and derivation of the surface brightness profile from our K-band data is shown in §4. The details on the mass modelling performed is presented in §5. Finally, the results of the mass models and a discussion of these results is presented in §6.

2 Chapter 2 - NGC 6503: Literature Review and Data Presentation

2.1 NGC 6503

NGC 6503 is a low-luminosity, late-type spiral galaxy that is relatively isolated from systems of similar mass. The de Vaucouleurs type of this galaxy is SA(s)cd (de Vaucouleurs et al., 1991a), which means that this is a late-type (cd), unbarred spiral galaxy (SA), without a ring [(s)]. Although this is a modest low-luminosity galaxy, Lira et al. (2007) find a bright central nucleus. This and radio emission in the central region of NGC 6503 suggest that it has a low-luminosity active galactic nucleus (AGN). This galaxy's isolation, simple apparent structure, and low-luminosity make it an ideal candidate for an in-depth kinematic and photometric study. The known properties of NGC 6503 are given in Table 1. A Hubble Legacy Archive image for NGC 6503 is shown in Fig. 8[5].

Because of its suitability for detailed structural studies, NGC 6503 has been the focus of several recent studies. Greisen et al. (2009) present new aperture synthesis observations of NGC 6503. Even with considerably higher H I resolution and sensitivity than previous studies they find that the H I disk is remarkably regular. They also find that the disk is best modelled with 2 components: a thin and a thick disk. The modelled thick disk has a low column density and is rotationally lagging (in comparison to the thin disk) and is truncated at the optical radius (Thilker et al., 2007). They therefore present evidence for a clear correlation between the presence of extra-planar gas and the stellar disk. Freeland et al. (2010) present H-band ($1.6\mu m$) imaging for NGC 6503, using the WIYN Observatory High Resolution Infrared Camera. They present evidence for a strong end-on bar, arguing that it is the only configuration capable of reproducing the central σ-drop (the depression of the velocity dispersion in the centre of spiral galaxies) observed. Puglielli et al. (2010) constructed dynamical models of NGC 6503 using Bayesian statistics and Markov chain Monte Carlo techniques. They tested four different disk models and found that the model treating

[5]Based on observations made with the NASA/ESA Hubble Space Telescope, and obtained from the Hubble Legacy Archive, which is a collaboration between the Space Telescope Science Institute (STScI/NASA), the Space Telescope European Coordinating Facility (ST-ECF/ESA) and the Canadian Astronomy Data Centre (CADC/NRC/CSA).

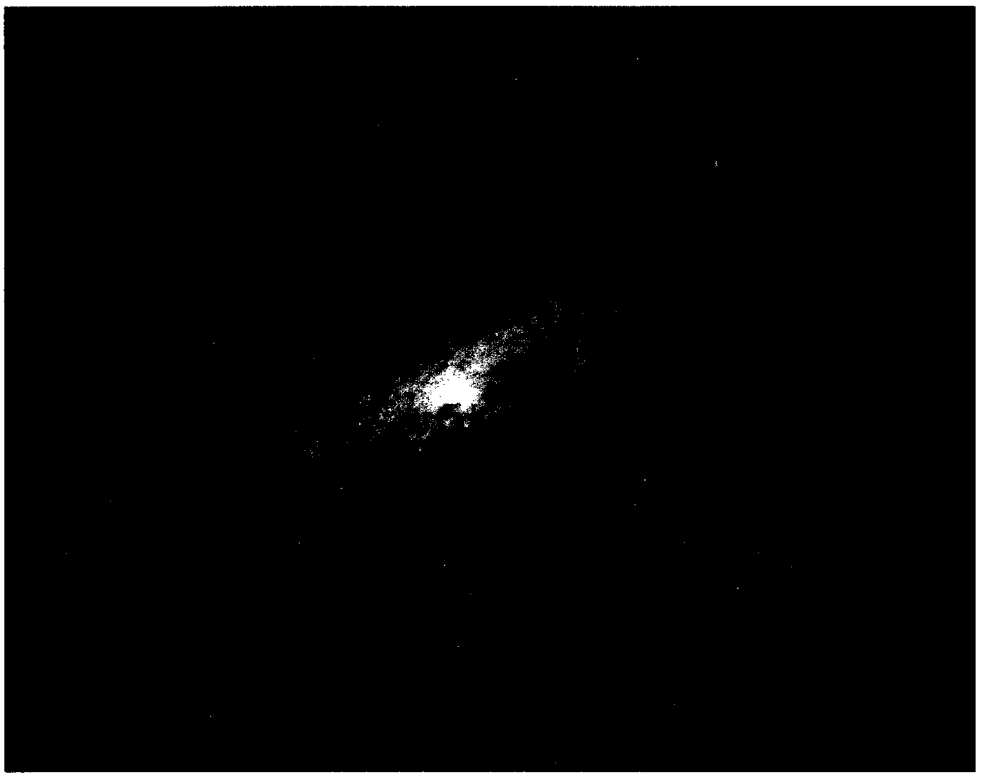

Figure 8 Hubble Legacy Archive image of NGC 6503.

the galaxy as having an inner truncated disk best fits the data. They also present evidence for a cuspy ($\alpha \gtrsim 1$ in Eq. 9) dark matter halo.

We have acquired and compiled new, high-quality, multi-wavelength kinematics and photometry for NGC 6503. This enables a detailed search for non-circular motions for the first time, as well as a detailed mass modelling study.

2.2 The Data

There are a variety of observable tracers of the kinematics of a galaxy disk (see §1), and each has advantages and disadvantages. H I data are especially useful in constructing extended rotation curves of galaxies due to the quantity of H I gas in the outer regions of galactic disks. Unfortunately the low angular resolution of H I observations due to the low frequency of the transition ($\nu_0 = 1420$ MHz in Eq. 1) gives rise to biases of the inner rotation curve (such as beam smearing discussed in §1.4). The increased resolution of Hα ($\nu_0 = 457$ THz) observations often complements the H I data for this reason. Despite this advantage, Hα observations could potentially

Table 1. Properties of NGC 6503

Parameter	Value	Source
Right ascension (J2000)	$17^h49^m26^s.50$	Jarrett et al. (2003)
Declination (J2000)	$70°08'40''$	Jarrett et al. (2003)
Systemic Velocity (Heliocentric)	34.20 ± 0.38 km s^{-1}	This Work
Position Angle	$117.5° \pm 0.06$	This Work
Inclination	$68.45° \pm 0.11$	This Work
Distance	5.2 Mpc	Karachentsev and Sharina (1997)
Optical Radius	5.35 kpc	de Vaucouleurs et al. (1991b)
Scale	1 kpc = $40''$	Greisen et al. (2009)

Note. — The known physical parameters of NGC 6503 from a variety of sources. Those quoted to be from this work are the quantities derived from the final Velfit run of the multi-wavelength master dataset described in §3.3.

be affected by dust in the centre of galaxies. CO data (ν_0 = 115 GHz), which are much less affected by dust, are therefore used to further complement Hα observations. However, CO data are not usually used as the sole measure of the inner regions of galaxies due to a slightly poorer resolution and patchy distribution of CO gas (at least compared to Hα data).

Ideally, a combination of all these tracers can be used to derive a rotation curve. By using CO data to check for dust extinction (and as added information in the inner regions), using Hα data to construct the inner rotation curve with high resolution, and using H I data to trace rotation to the extended regions of the galactic disk, we can attempt to get the best of all worlds. As well as the data used to derive kinematics, photometric data are necessary in order to get an accurate representation of the mass profile of the stellar disk.

The basic properties of the datasets used to study NGC 6503 are listed in Table 2, and we discuss each one in turn below.

2.2.1 Hα - 1

An Hα dataset was kindly provided by Simon, in advance of publication, who acquired it as part of an initiative to obtain high quality 2D velocity field data in order to avoid problems associated with long slit spectroscopy. Using the WIYN telescope

with the Denspak fibre array, Josh Simon obtained Hα spectroscopy in order to determine the best estimation of the stellar mass-to-light ratios for a sample of low-mass galaxies. Through 5-11 positions, 350-650 independent velocity measurements, and exposure times between 10 to 60 minutes per position, angular and velocity resolutions of 4 arcseconds[6] and 13 $\mathrm{km\,s^{-1}}$ respectively were obtained. The data for NGC 6503 were processed in the same fashion as those presented by Simon et al. (2005).

A contour plot is shown in Fig. 9. This contour plot (as well as those that follow) describes the motion of the gas in the galaxy away (red) or towards (blue) us relative to the galaxy centre. As is seen from the legend, the more red a contour is the faster the parts of this galaxy are moving away from us. Similarly, the more blue a contour is, the faster it is approaching us. The analysis of this dataset and the results from the Velfit modelling of these Hα data are discussed in §3.2.1.

2.2.2 Hα - 2

A second, independently measured Hα dataset is available for NGC 6503, so we also included it in our analysis. The Hα - 2 dataset was kindly provided to us by Laurent Chemin and was published in Épinat et al. (2008). High spectral resolution 3D data cubes were obtained using a focal reducer containing the scanning Fabry-Pérot interferometer attached at the Cassegrain focus of the 1.93m OHP (Observatoire de Haute-Provence) telescope. The data were given to in a Flexible Image Transport System (FITS) format 512 $\times$ 512 pixel grid. Each pixel denoted 0.68 arcseconds but had an actual angular resolution of approximately 3 arcseconds. The information about this dataset and the instruments used in acquiring the data are explained by Épinat et al. (2008). A contour plot of this data is shown in Fig. 10. The results of modelling this dataset with Velfit and the analysis of the dataset itself will be discussed in §3.2.2.

[6] A unit of angular distance used in astronomy such that one arcsecond is $1/60^{th}$ of an arcminute (which is $1/60^{th}$ of a degree on the sky.)

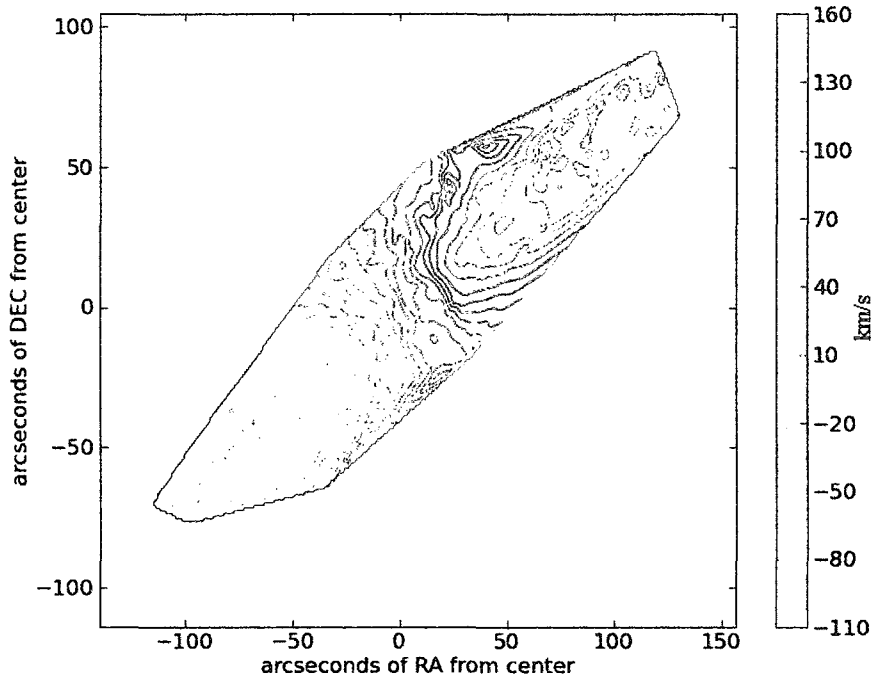

Figure 9 Contour plot of measured velocities in the Hα - 1 dataset, provided by Simon. Contours show constant recessional velocities and their amplitude, in km s^{-1}, is given by the colour bar on the right. The solid contours (red) show the receding side of the disk, and the dotted contours (blue) show the approaching side of the disk. The irregularity of the outer colour scale edge reflects the patchiness of the Hα emission and the velocity sampling pattern.

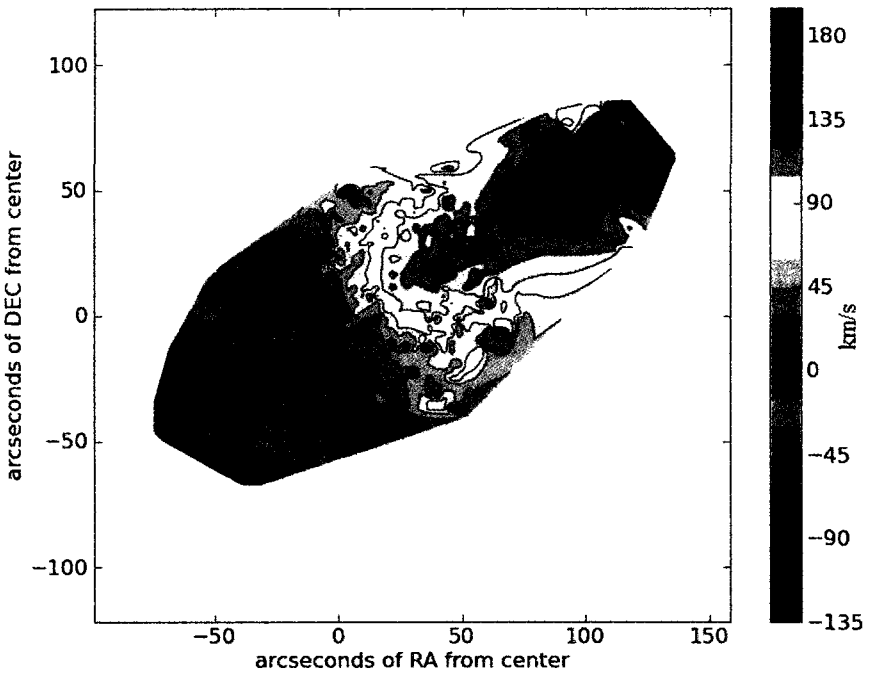

Figure 10 Same as Fig. 9 but for the Hα - 2 dataset.

2.2.3 H I

The H I dataset, presented in Greisen et al. (2009), was kindly provided to us by Eric Greisen. These data were obtained using the Very Large Array in the C configuration. They used 127 spectral channels each separated by 24.4 kHz (5.15 $\mathrm{km\,s^{-1}}$) centred on 26 $\mathrm{km\,s^{-1}}$ heliocentric radial velocity, and a total exposure time of just over 500 minutes. The H I data were given to us in the FITS format of a 1024 $\times$ 1024 pixel grid and were processed in manner described by Greisen et al. (2009). These data have a resolution of approximately 14 arcseconds and spans out to approximately 800 arcseconds on either side of the galaxy centre. The contour plot of these data is shown in Fig. 11. In §3.2.3 we will discuss this dataset and the result of modelling for its non-circular flows.

2.2.4 CO

The CO data were kindly provided to us by Peter Teuben, in advance of publication, through observations with the 23 antenna Combined Array for Research in

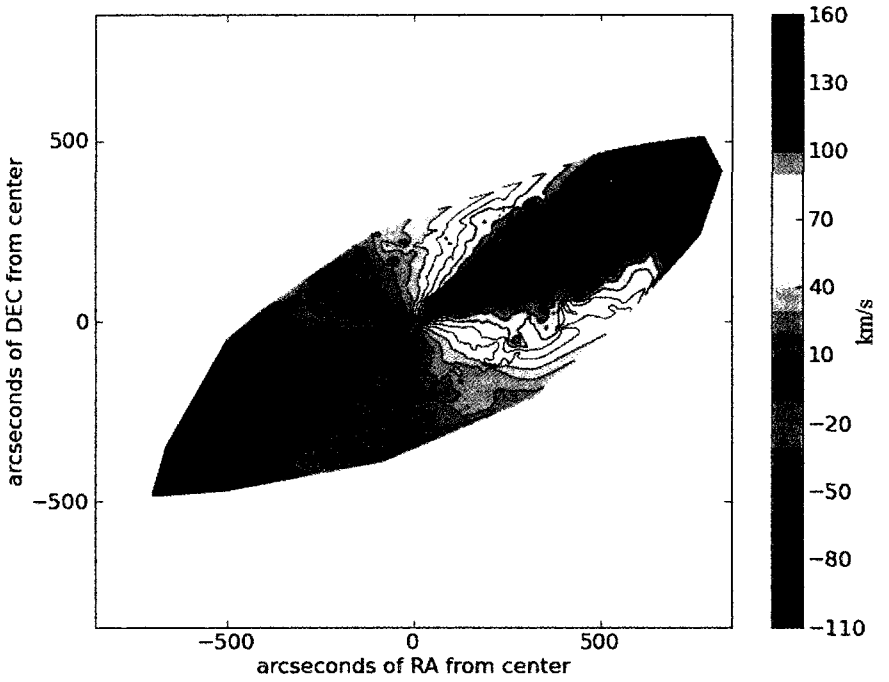

Figure 11 Same as Fig. 9 but for the H I dataset. The irregularity of the outer colour scale edge reflects the patchiness of the H I emission at the disk edge.

Millimeter-wave Astronomy interferometer. The data came to us as a FITS data-cube with a 339 × 309 pixel grid and a masked total intensity map for the kinematic analyses. These data have a resolution of approximately 5 arcseconds and cover the inner 100 arcseconds of the galaxy. The contour plot of these data is shown in Fig. 12. In §3.2.4 we will discuss this dataset and the result of modelling it for its non-circular flows.

2.2.5 K-band

To complement literature photometry we acquired our own K-band images. The K-band was chosen to minimize the effect of dust extinction in our highly inclined galaxy (Table 2). We acquired this K-band photometry using CFHT's (Canada-France-Hawaii Telescope) WIRCAM through a total of one hour of exposure time in a dithering pattern of fifteen second individual exposures. These data were reduced by Michael McDonald, according to the procedure of McDonald et al. (2009), in order to provide a single two-dimensional FITS image of NGC 6503 with a resolution of 1

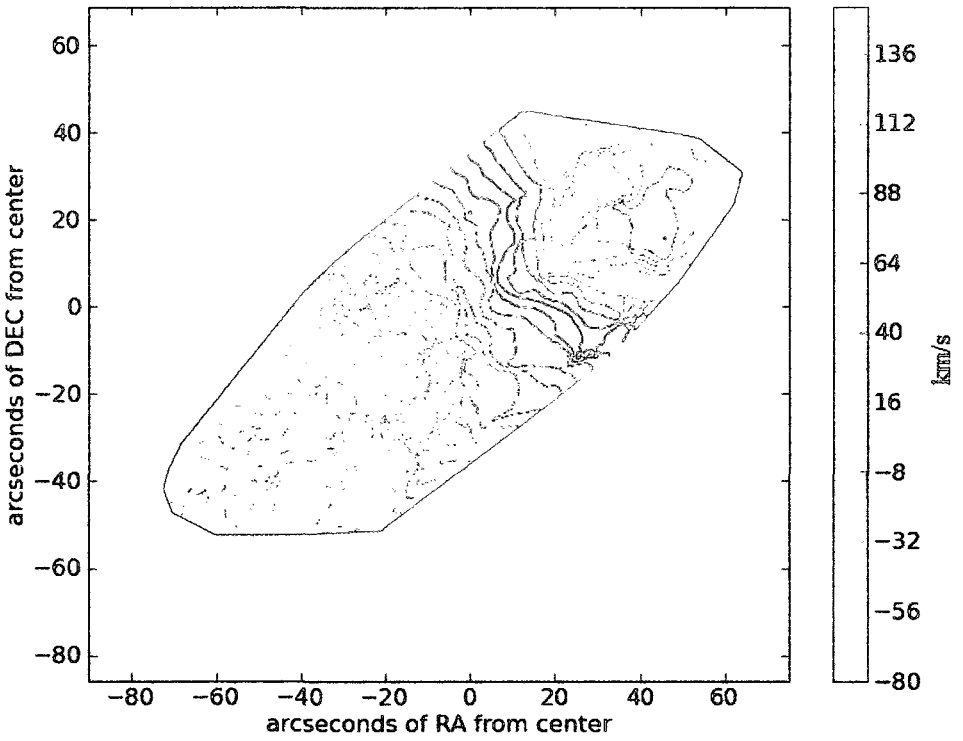

Figure 12 Same as Fig. 9 but for the CO dataset. The irregularity of the outer colour scale edge reflects the patchiness of the CO emission.

arcsecond. The histo-equalized K-band image with FITS viewer is shown in Fig. 13.

2.3 Comparing the Kinematic Datasets

Considering that all of the kinematic datasets for NGC 6503 trace the dynamics of the disk, one would expect the measured velocities to be consistent to within their uncertainties. A direct comparison between the two Hα datasets will be shown in §2.3.3. A comparison between Hα - 1 data and the H I data will be discussed in §2.3.1. Finally a similar comparison between the Hα - 2 data and the H I data will be discussed in §2.3.2. Because the emission in the CO dataset is patchy and more poorly sampled than in the other datasets, we do not include it in this analysis.

2.3.1 Comparison of the Hα - 1 and H I Datasets

The Hα - 1 dataset was compared to the H I dataset by carrying out two major steps; first, the H I data was extracted from the FITS format to a format similar to that of the Hα data, and the measured positions and velocities were made into arrays

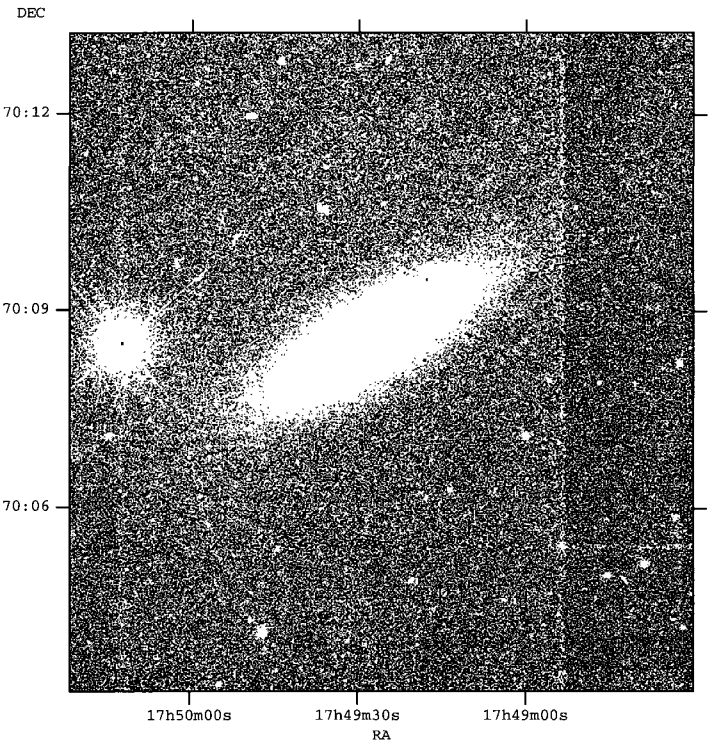

Figure 13 histo-equalized image of NGC 6503 in the K-band.

Table 2. Dataset Properties

Dataset	Rest Frequency	Angular Resolution $''$	Coverage Used $''$	Reference
(1)	(2)	(3)	(4)	(5)
Hα - 1	456.8 THz	4	140	Josh Simon[1]
Hα - 2	456.8 THz	3	140	Épinat et al. (2008)
H I	1420 MHz	14	500	Greisen et al. (2009)
CO	115.3 GHz	5	90	Peter Teuben[1]
K-band	139.7 THz	1	279	This work

Note. — Col. (1): Dataset. Col. (2): Rest wavelength of spectral line, or photometric band. Col. (3): Approximate angular resolution of the dataset. Col.(4): Approximate coverage the dataset has of NGC 6503 with respect to the centre of the galaxy. Col.(5): Data source. Note:[1] indicates that the data were provided to us in advance of publication.

in IDL. Second, for each point in the Hα data we found the closest coordinate point to it in the H I data through a series of loops in IDL. A new array was made of all of the velocity values that corresponded to these nearest points. The Hα - 1 and H I velocity arrays were then subtracted from one another, and the resulting array was contoured in the same fashion as in Figs. 9-12. The corresponding contour plot (and histogram) for the residuals, ΔV, is found in Fig. 14. The discrepancies between the Hα - 1 and H I data follow a relatively Gaussian distribution, though shifted to $\Delta V > 0$ km s^{-1} instead of peaking around zero. This too can be seen from the red sections of the contour plot on the right hand side of the galaxy. Although the noticeably large velocity differences (sometimes $\Delta V \simeq 30$ km s^{-1}) are not completely unexpected for a disk with a gas velocity dispersion of $\simeq 5$ km s^{-1} (see §3.2), the fact that they occur mostly on the right hand side of the galaxy is interesting. Despite the aforementioned large discrepancies, the majority of the velocity differences do lie within 20 km s^{-1}.

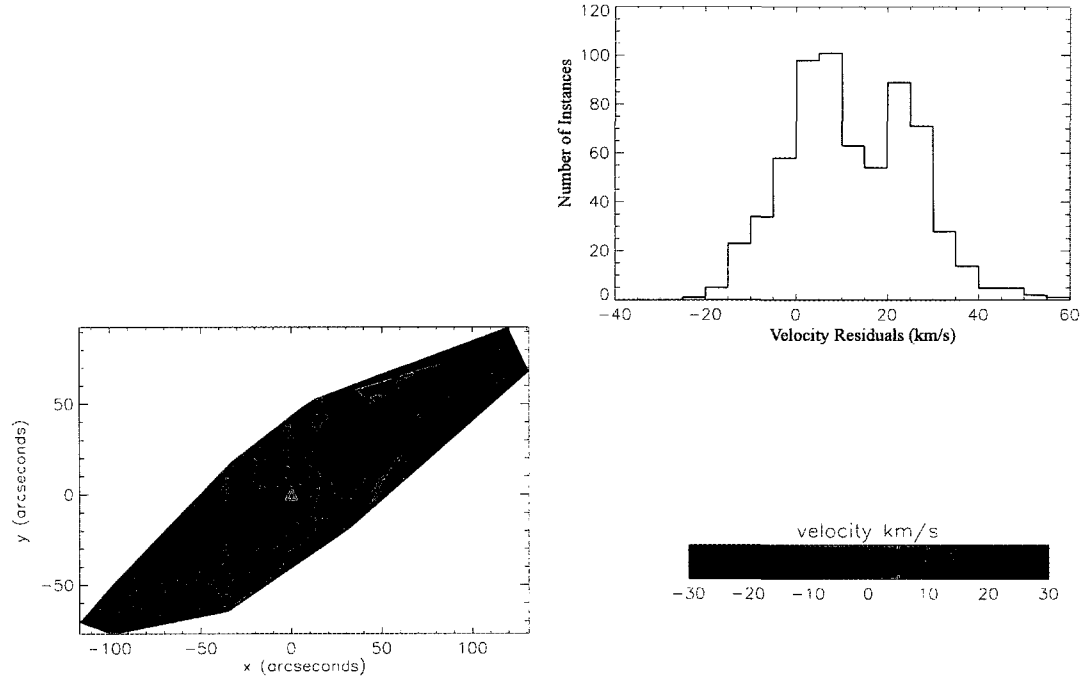

Figure 14 Bottom left shows the contour plot of the residuals obtained by subtracting the Hα - 1 and the H I datasets. Light blue or green is representative of very little difference between the datasets, whereas dark blue or red indicates greater discrepancies. The histogram in the upper left shows the essentially normal distribution of the residuals using a bin size of 10 km s^{-1}.

2.3.2 Comparison of the Hα - 2 and H I Datasets

Both the Hα - 2 and the H I datasets came in the FITS format, making comparison slightly simpler than explained in §2.3.1. Since there were minor differences in format between the two datasets, the AIPS task OHGEO was used to change the astrometry of the Hα - 2 dataset to match that of the H I data. This transformation mainly placed the Hα data in a 1024 X 1024 grid and corrected for the difference in orientation (FITS keyword CROTA2) between the datasets. The H I data was then subtracted from the Hα - 2 data using the AIPS program COMB. The results of this subtraction as well as the histogram distribution of the velocity residuals are shown in Fig. 15. The histogram shows that the differences in velocity between the two datasets follow a relatively Gaussian distribution centred at $\Delta V = 0$ km s^{-1}. From the contour plot, it can be seen that the major areas of discrepancy between the Hα - 2 and H I datasets are located on the approaching side of the galaxy and along the edges of the receding side. Although there are some large values of ΔV, it can easily be seen that the majority of the velocity differences between the two datasets have $\Delta V \leq 20$ km s^{-1}.

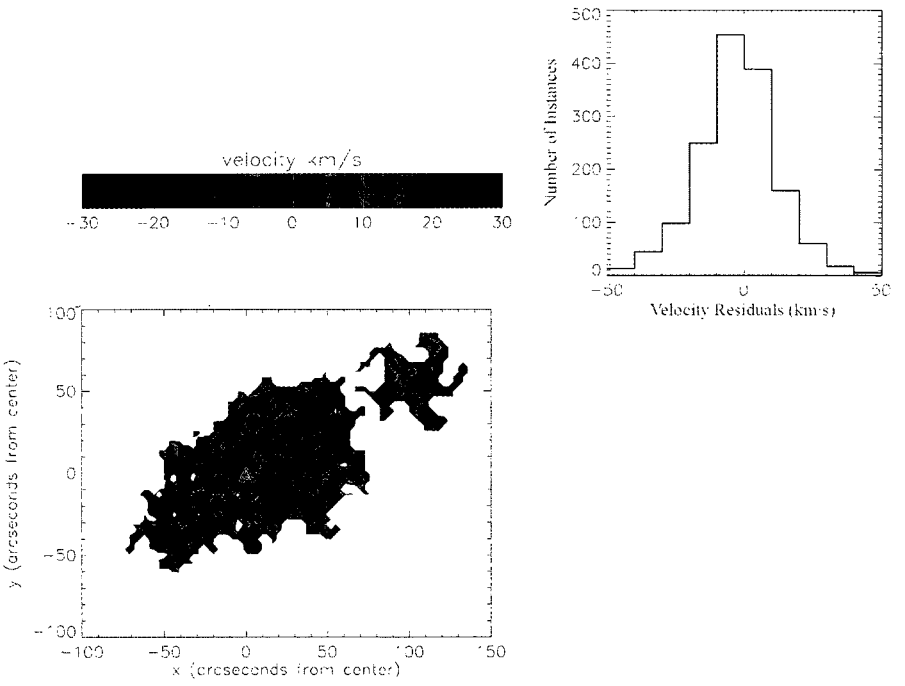

Figure 15 Same as Fig. 14 except the comparison between the Hα - 2 and H I datasets.

2.3.3 Comparison of Hα - 1 and Hα -2 datasets

When comparing between the two Hα datasets we used the same method as applied in §2.3.1: the Hα - 2 FITS data was read into IDL arrays and the point closest in position to each data point in the Hα - 1 dataset was determined. Finally the Hα - 2 velocity array was subtracted from the Hα - 1 array. It is important to note here that the Hα - 2 FITS file imported into IDL had been transformed to the same coordinate geometry as the H I data using OHGEO (see §2.3.2). What is significant to notice when comparing these two Hα datasets (seen in Fig. 16) is that the distribution of residuals is relatively Gaussian although centred on $\Delta V \sim 20$ $\mathrm{km\,s^{-1}}$. This is interesting because there was also a velocity offset between the Hα - 1 and H I datasets of the the same amplitude (see §2.3.1). Although it is not yet certain whether or not these discrepancies are related (due to geometry or otherwise), it is necessary to note when considering the accuracy of the data used.

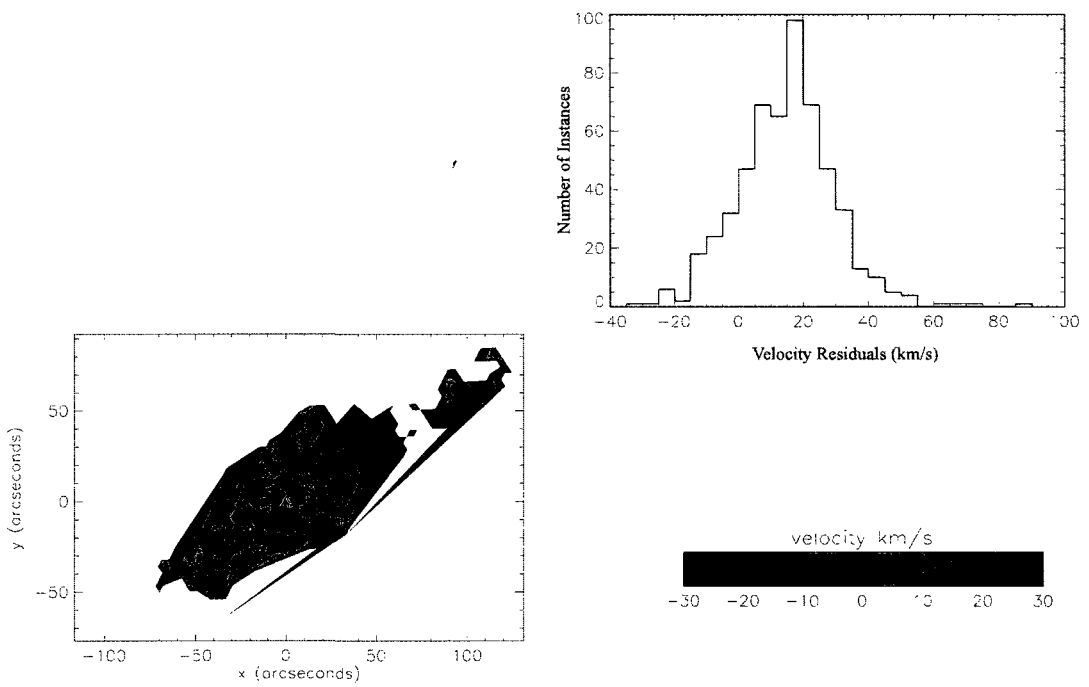

Figure 16 Same as Fig. 14 except the comparison between the Hα - 1 and Hα - 2 datasets.

2.3.4 Conclusions

The direct comparisons between the Hα - 1, Hα - 2, and H I datasets demonstrate that the measured recessional velocities in different tracers appear similar.

However, there are some large ($\Delta V \gtrsim 20$ km s^{-1}) discrepancies whose origin is unclear: they could stem from real differences in the gas velocities, or from differences in the dataset geometries. To quantitatively compare the datasets, a more sophisticated technique is required. In the next chapter, we use the code Velfit to carry out this comparison as well as to search for non-circular motions.

3 Chapter 3 - Kinematic Analysis

The goal of this project is to combine high quality data from different tracers and sources in order to understand the structure of NGC 6503 to a previously unparalleled level. By exploiting the high resolution of Hα data, the breadth of coverage available with H I, and the extinction-free CO data, we will be able to produce a velocity field for this galaxy of much higher quality than that of a single tracer. In this chapter, we use the Velfit code (Spekkens and Sellwood, 2007) to analyse each dataset in detail, search for non-circular motions, and derive a multi-wavelength rotation curve for NGC 6503. This rotation curve will then be used in the mass modelling of §5 to constrain the mass-to-light ratio and the dark matter halo structure of NGC 6503. In §3.1 we will discuss the pre-processing steps before analysis. In §3.2 we will discuss the search for non-circular flows using Velfit for each of the datasets. Finally, in §3.3 we discuss the combination of the data into one multi-wavelength, master dataset.

3.1 Pre-Processing

The Hα - 1 dataset was given to us in text file format. Relevant columns for this analysis are the RA and dec of each velocity measurement (expressed in arcseconds with respect to the galaxy centre), the measured velocity, and the uncertainty on the measurement.

The Hα - 2 dataset was originally given to us in FITS format. As explained in §2.3, in order to render the astrometry of the image identical to that of the H I data (which was also in the format), we ran the data through the OHGEO task in AIPS. The corrected Hα - 2 data was then re-read into IDL, and the positions (in arcseconds from the galaxy centre) and velocities written out into a text file that matched the input format required by Velfit.

The H I dataset was also given to us in the FITS file format and it too was imported into IDL and converted into a text file format. The high inclination of NGC 6503 (Table 2) means that it is possible to underestimate the amplitude the line-of-sight velocities from the measured spectra using standard techniques. In order to compensate for the effects this has on the rotation curve, the dataset was envelope

traced, by Kristine Spekkens, through a series of Gipsy and AIPS tasks to implement the MET method of Gentile et al. (2004).

The CO dataset was also provided to us in the FITS file format and was therefore pre-processed in a similar fashion as the Hα - 2 dataset.

3.2 Searching for Non-Circular Flows with Velfit

Velfit, as introduced by Spekkens and Sellwood (2007), is a new procedure which aims to fit non-axisymmetric flow patterns to 2-D velocity maps of spiral galaxies. Although the program focusses on flows caused by bar-like or oval distortions to the total potential, it also provides means for modelling purely radial flow components as well. The main inputs into Velfit are the velocity fields presented in §2.2. In addition to the velocity fields, Velfit takes initial guesses for the centre of the galaxy (x_c and y_c with respect to the centre of the galaxy as given in Table 1), the systemic velocity, the ellipticity [$\cos(i) = 1 - \epsilon$ for an inclination i], and the position angle (the angle subtended by the major axis of the galaxy referenced to North, moving counter clockwise towards East). Finally, a value for the ISM turbulence parameter (Δ_{ISM}) needs to be given. For our calculations, we use a $\Delta_{ISM} = 6\ \mathrm{km\,s^{-1}}$ in order to be consistent with turbulence in galaxy disks and in order to produce reasonable χ^2 statistics. Although further increasing (or decreasing) the value for Δ_{ISM} obviously affects the goodness of fit given by the χ^2, we can still use the statistics to compare best fitting models. As long as we use the same Δ_{ISM} for all models used, we can still determine the models' goodness of fit with respect to each other (assuming $\chi^2_{\mathrm{r,min}}$ close to one). This project uses V1.0 of the code publicly available at `http://www.physics.rutgers.edu/~spekkens/velfit/`.

One of the key reasons why NGC 6503 was used for this project is that it appears to be a simple, regularly rotating system whose kinematics do not exhibit non-circular flows (see §2). Before we can safely make this assumption we must model our galaxy for non-circular flows to verify that this indeed is the case. Using Velfit, we model each of the velocity fields, described in §3.1, as a system containing rotation-only, radial, or bisymmetric flows. The rotation-only model is identical to Eq. 4:

$$V_{model} = V_{sys} + V_t(r)\cos(\theta)\sin(i) \tag{11}$$

where V_{sys} is the systemic velocity, $V_t(r)$ is the rotational component of the velocity and θ and i are defined as in Fig. 3. Velfit models for purely radial flows with Eq. 7 by Spekkens and Sellwood (2007):

$$V_{model} = V_{sys} + \sin(i)[V_t(r)\cos(\theta) + V_r(r)\sin(\theta)] \tag{12}$$

where $V_r(r)$ is the inflow/outflow velocity (radial) component. In order to model for bisymmetric flows to the potential, Velfit models velocities as given by Eq. 5 of Spekkens and Sellwood (2007):

$$V_{model} = V_{sys}+\sin(i)[V_t(r)\cos(\theta)-V_{2,t}(r)\cos(2\theta_b)\cos(\theta)-V_{2,r}(r)\sin(2\theta_b)\sin(\theta)] \tag{13}$$

where $V_{2,t}(r)$ and $V_{2,r}(r)$ are the tangential and radial components of the non-circular (in this case bisymmetric) flows respectively. In the bisymmetric model, the angle $\phi_b = \theta - \theta_b$ of the bisymmetric distortion from the major axis is also a free parameter in the fit. A visual representation of the geometry involved in the bisymmetric flows (Spekkens and Sellwood, 2007, Fig.1) is shown of Fig. 17. We also tried fitting lopsided models to all of our data but this did not give plausible results.

All kinematic models are fit by minimizing the χ^2 statistic:

$$\chi^2 = \sum_{n=1}^{N}\left(\frac{V_{los}(x,y) - \sum_{k=1}^{K} w_{k,n}V_k}{\sigma_n}\right)^2 \tag{14}$$

where $V_{los}(x,y)$ are the velocities in the data, V_k are the model velocities, $w_{k,n}$ interpolate the model velocities to the data locations, σ_n are the data uncertainties, and N is the number of datapoints.

In all cases Velfit returns the best-fitting kinematic centre, position angle, disk inclination, and rotation curve (V_{model} in Eq. 11); non-circular flow profiles are also returned for the radial and bisymmetric flow models, and the bar angle is an additional output in the latter model.

For this model and for the bisymmetric model later we sometimes refer to a

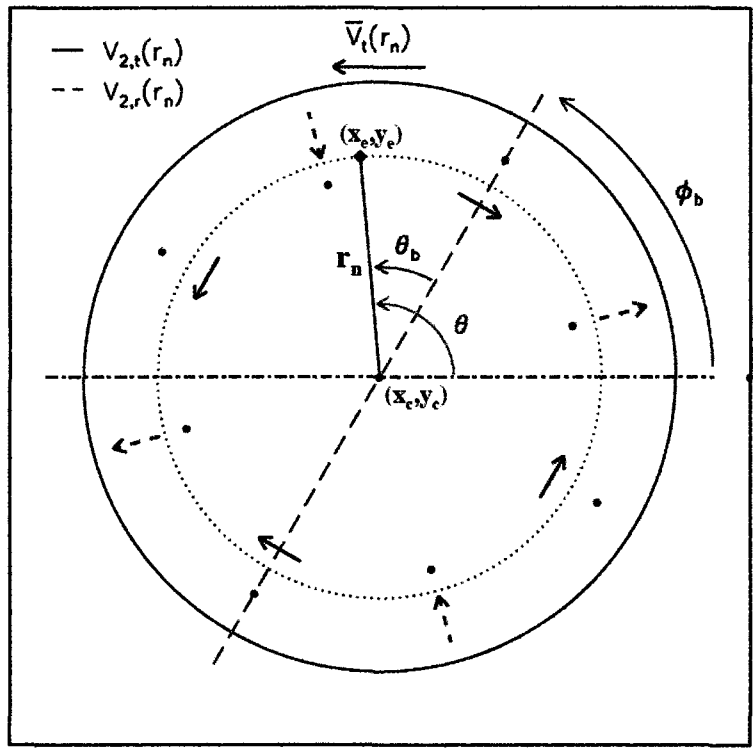

Figure 17 Fig. 1 from Spekkens and Sellwood (2007), caption taken and adjusted from that paper. Parameter definitions and flow pattern in the disk plane for the bisymmetric model (Eq. 13). The solid circle represents the largest r included in the model, and the horizontal dash-dotted line is the major axis of the disk defined by the sky plane. The long dashed line is the major axis of the bisymmetric distortion, at angle ϕ_b from the major axis. The diamond denotes the location (x_e, y_e) of a datapoint, a distance r_n from the centre (x_c, y_c) and at PAs θ_b from the bisymmetric distortion axis and θ from the major axis. The dotted circle shows the circular orbit of radius r_n in the disk, and the axisymmetric model component $V_t(r_n)$ is in the counter-clockwise direction. The extrema of components $V_{2,t}(r_n)$ and $V_{2,r}(r_n)$ are indicated by solid and dashed arrows, respectively, and large dots at the same distance from (x_c, y_c) as each set of arrows denote PAs where the corresponding component passes through zero.

fit as unrealistic or inconsistent. Essentially this means that even though Velfit is able to produce a fit for that model, the number of degrees of freedom only allows a fit where the uncertainties are as large as the features themselves. In describing the goodness of fits in the following sections, we refer to whether or not a change in $\chi^2_{\rm r,min}$ ($\chi^2_{\rm r,min} = \chi^2/\nu$, where ν is the number of degrees of freedom in the fit) is significant or not. We can assume that the χ^2 distribution is an approximately normal for fits to our data and therefore for a good fit ($\chi^2_{\rm r,min} = 1$) $\chi^2 = \nu$. With the standard deviation for a χ^2 distribution defined as $\sqrt{2\nu}$, a one sigma result has a χ^2 value that falls in the range $\chi^2 \pm \sqrt{2\nu}$ (Press et al., 1992). Throughout of our analysis, we define a fit as significantly better or worse if it is different by more than 1σ from the fit to which it is being compared.

3.2.1 Hα - 1

rotation-only (Eq. 11), radial flow (Eq. 12), and bisymmetric flow (Eq. 13) models were fit to the pre-processed Hα - 1 data. The bisymmetric model outputs were unrealistic, in that the uncertainties are as large as the detected features (see §3.2). As such, this model does not provide a reliable fit to the Hα - 1 data and we do not consider it further. The best-fitting values for the rotation-only and radial models are in Table 3.

When comparing the two plausible models for the Hα - 1 data, we look at both the velocity field components in Fig. 18 and Fig. 19 as well as the two $\chi^2_{\rm r,min}$ found in Table 3. The rotation curves ($V_t(r)$) are almost exactly the same despite the addition of the $V_r(r)$ component in Fig. 19. Also noticeable is that the $V_r(r)$ component in Fig. 19 is almost consistently zero thereby suggesting that it is insignificant compared to $V_t(r)$. As well from observing the $\chi^2_{\rm r,min}$ values in Table 3 we can see that there is not a significant drop in $\chi^2_{\rm r,min}$ to suggest a preference for either model.

3.2.2 Hα - 2

Velfit was used to find the best-fitting model of the rotation-only, radial, and bisymmetric models for the pre-processed Hα - 2 dataset. The rotation curve for the rotation-only model is shown in Fig. 20, and the best-fitting components of the radial

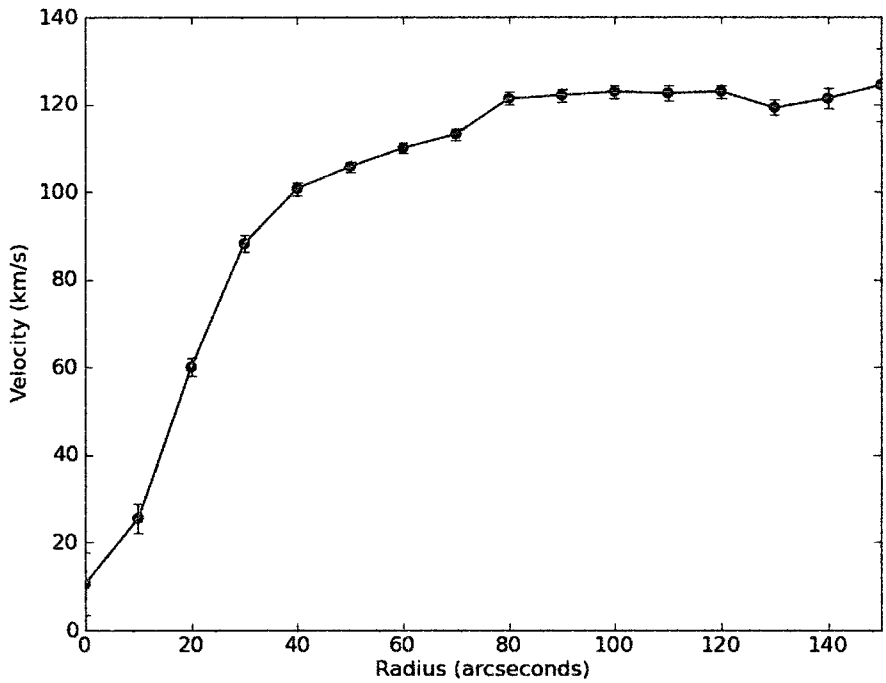

Figure 18 Rotation-only model outputs obtained for the Hα - 1 dataset. The solid line shows the rotational velocity ($V_t(r)$), in $\mathrm{km\,s^{-1}}$, with respect to the distance from the centre of the galaxy (in arcseconds). Error bars are shown in black for each of the points.

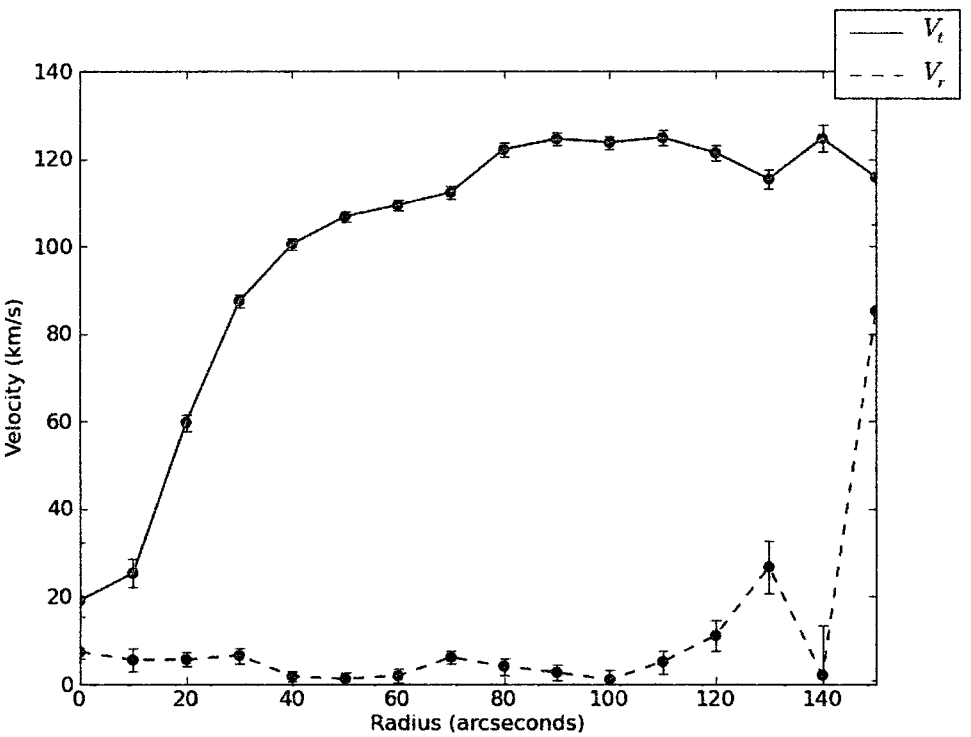

Figure 19 Radial flow model outputs obtained for the Hα - 1 dataset. The solid red curve shows circular velocity ($V_t(r)$), in $\mathrm{km\,s^{-1}}$, as a function of distance from the centre of the galaxy (in arcseconds). The dashed blue curve is the radial velocity ($V_r(r)$) component. Error bars are shown in black for each of the data points.

model is shown in Fig. 21. Finally, similar to the Hα - 1 dataset, the best-fitting bisymmetric model was not plausible. The best-fitting properties of the rotation-only and radial models can be seen in Table 3. The higher values of χ^2 for the Hα - 2 data (see Table 3), compared to the Hα - 1 data, is due to the way that pixels are defined in the data (see Épinat et al., 2008).

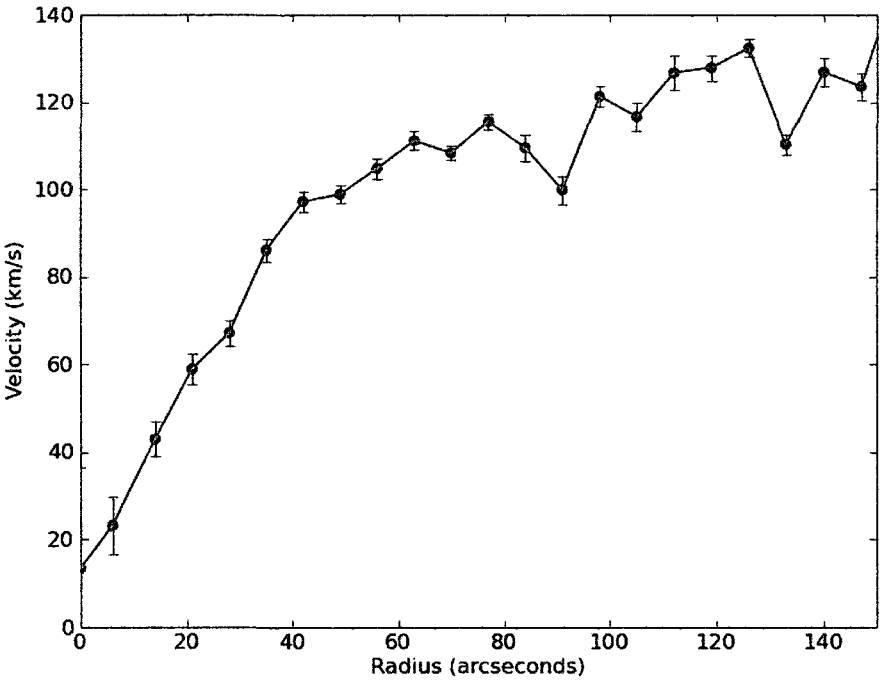

Figure 20 Same as Fig. 18 but for the Hα - 2 dataset.

Similar to the arguments made for the Hα - 1 dataset, through the observation of Figs. 20 and 21 show that there is little evidence for a radial component. The lack of a significant difference between $\chi^2_{r,min}$ for the two models applies to the the Hα - 2 dataset as well. For these reasons we do not see significant evidence for radial flows in the Hα tracer for NGC 6503.

3.2.3 H I

As with the other datasets, the rotation-only, radial, and bisymmetric models were fit to the pre-processed H I data. The resultant rotation curve in the rotation-only model can be seen in Fig. 22 and the radial model components can be found in

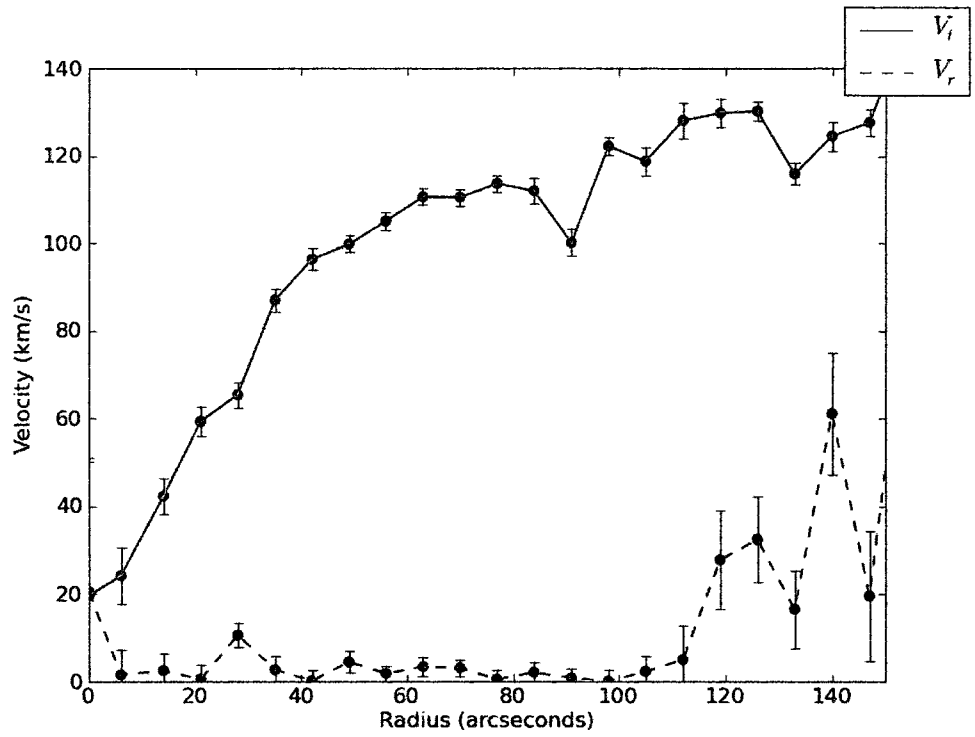

Figure 21 Same as Fig. 19 but for the Hα - 2 dataset.

Fig. 23. The rotation curve of the bisymmetric model can be seen in Fig. 24. Unlike the Hα datasets, repeatable results were also obtained for the bisymmetric model fit to the data. The best-fitting parameters for all 3 models are given in Table 3.

The results for the rotation-only and radial models are similar to those of the 2 Hα datasets, but the bisymmetric model (Fig. 24) gives us something completely different. The $V_{2,t}(r)$ component of the bisymmetric flow is essentially zero (as was the case with the radial flows in both of the Hα datasets) but the $V_{2,t}(r)$ component on the other hand fluctuates noticeably away from zero. It is also clear that the $V_t(r)$ are in fact not the same between the rotation-only, radial,and bisymmetric models. There is no significant drop in the $\chi^2_{\mathrm{r,min}}$ value between the rotation-only and radial models (Table 3), but there is a significant drop between the former two and the bisymmetric model (although the extremely low $\chi^2_{\mathrm{r,min}}$ in this case suggests a possible over-fitting of the data). Even considering the numerous degrees of freedom with this dataset and the model, the drop in $\chi^2_{\mathrm{r,min}}$ is still significant.

The bisymmetric model therefore provides the best statistical fit to the H I data

for NGC 6503. However, whether this fit actually signals bisymmetric flows in the disk remains unclear. One reason to doubt the physical implications of the bisymmetric model is the expected ratio between the non-circular velocity components. Sellwood and Sanchez (2009) explain that for the case where non-circular motions are caused by a non-rotating, axisymmetric, oval distortion (those being solved for in the bisymmetric case) we should expect $V_{2,t}(r) \approx 1.5V_{2,r}(r)$. As can be seen in Fig. 24, this is not the case for our non-circular flows at most values of r (ie. $50'' < r < 300''$).

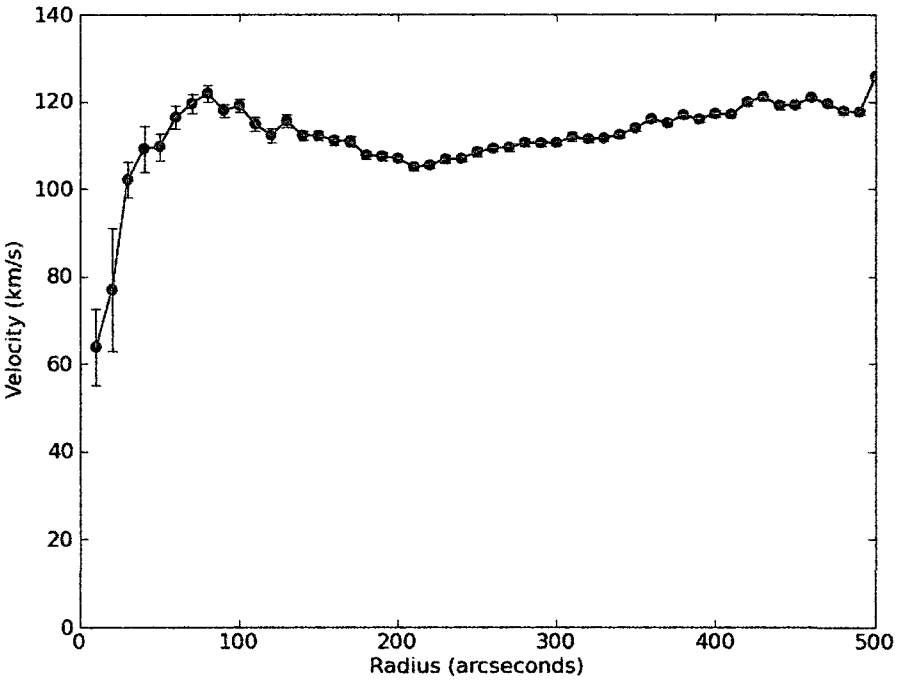

Figure 22 Same as Fig. 18 but for the H I dataset.

Since we were not convinced that the best-fit model mentioned previously for the H I data is actually representative of a galactic bar, we took a closer look at this dataset using Velfit. The parameters for which the H I data solved previously ($V_{\rm sys}$, i, ϕ'_d, x_c, and y_c) were fixed to be 27.76 $\rm km\,s^{-1}$, 68.26°, 117.34°, -0.61″, and -3.06″ respectively. The H I data were then separated into four quadrants which corresponded to the northern (N) and southern (S) portions of the galaxy (separated along the major axis) and the eastern (E) and western (W) sides of the galaxy (separated along the minor axis). In the case of a bonafide bar the best-fitting parameters obtained

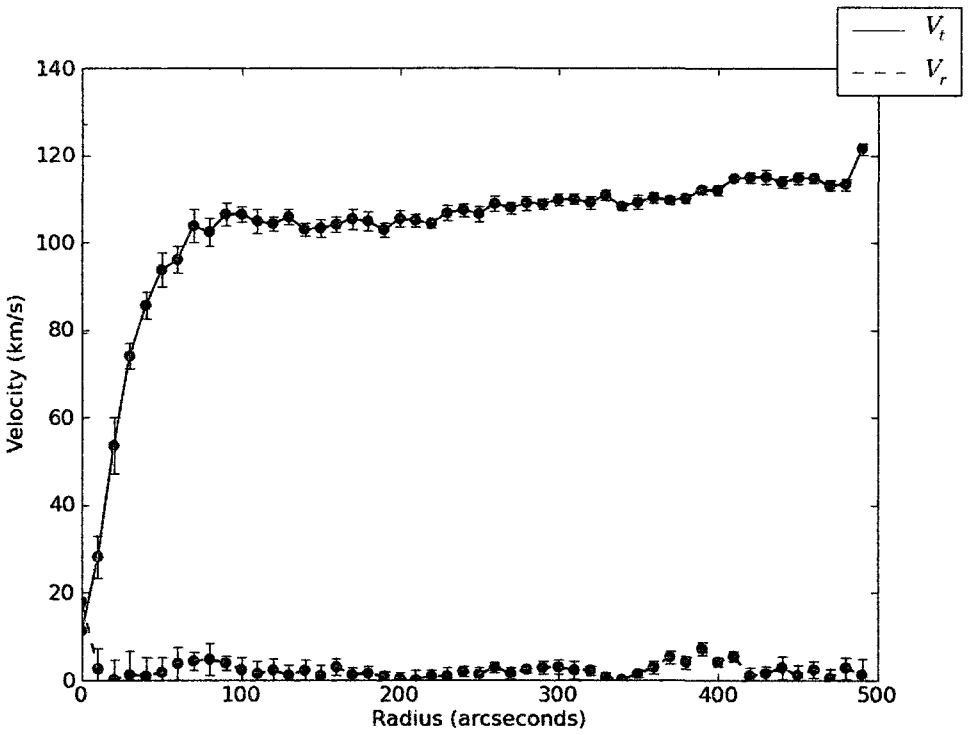

Figure 23 Same as Fig. 19 except for the H I dataset.

from each subset should be consistent with each other. Each of these four subsets of the H I data was therefore run through Velfit in order to solve for the best-fitting bisymmetric model parameters. The resulting model fits can be seen in Figs. 25, 26, 27, 28.

Velfit's bisymmetric model fits the data for non-circular flows about a bar axis at position angle ϕ_b relative to the major axis (Fig. 17). The fits to the E and W halves of the galaxy returned $\phi_b = 7.48 \pm 0.10$ and $\phi_b = 6.14 \pm 0.10$, respectively. Fig. 17 shows that ϕ_b is therefore close to the major axis, where the velocity field is best sampled. The points along the minor axis of the galaxy do not have as much pull [since $\cos(\theta) \approx 0$; see Eq. 13] and they essentially cancel out with those on the other side of the major axis. Therefore any discrepancies from pure rotation will be fit by the model as a bar.

Each ϕ_b solved by Velfit lies extremely close to the major axis, and both models produce different non-circular components (Figs. 25 and 26). An explanation for this can be inferred by examining Eq. 13. When angle ϕ_b is close to either the major or

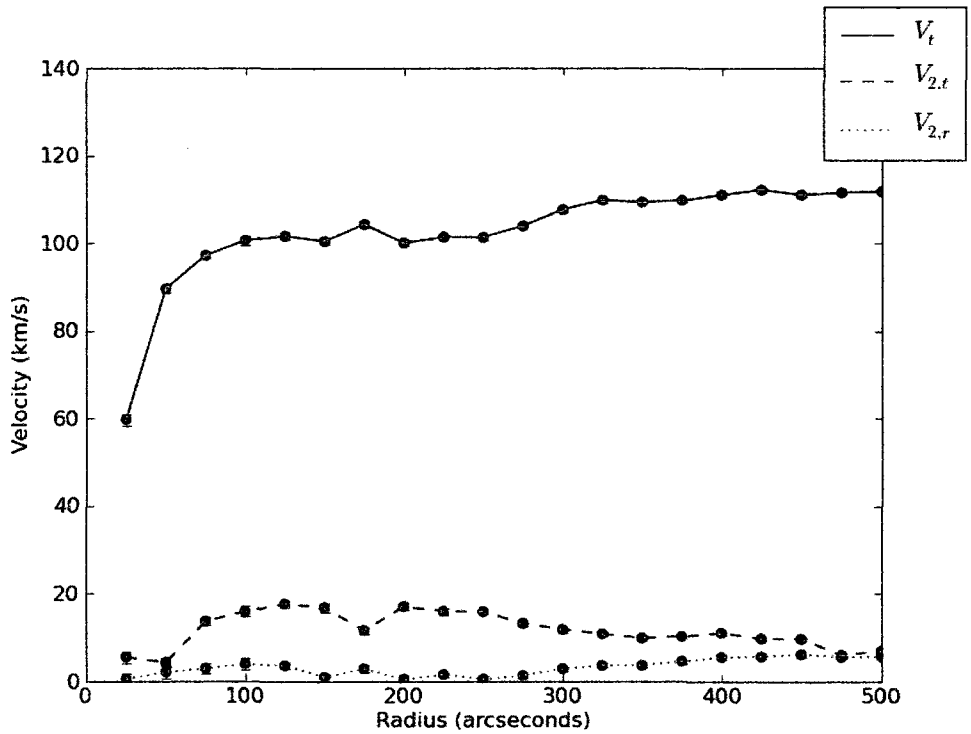

Figure 24 Bisymmetric model output obtained for the H I dataset. The solid red curve shows circular velocity ($V_t(r)$), in $\mathrm{km\,s^{-1}}$, as a function of distance from the centre of the galaxy (in arcseconds). The dashed blue line gives the tangential component of the non-circular flows ($V_{2,t}(r)$) and the dotted green line give the radial component of the non-circular flows ($V_{2,r}(r)$). Error bars are shown as black bars for each of the data points.

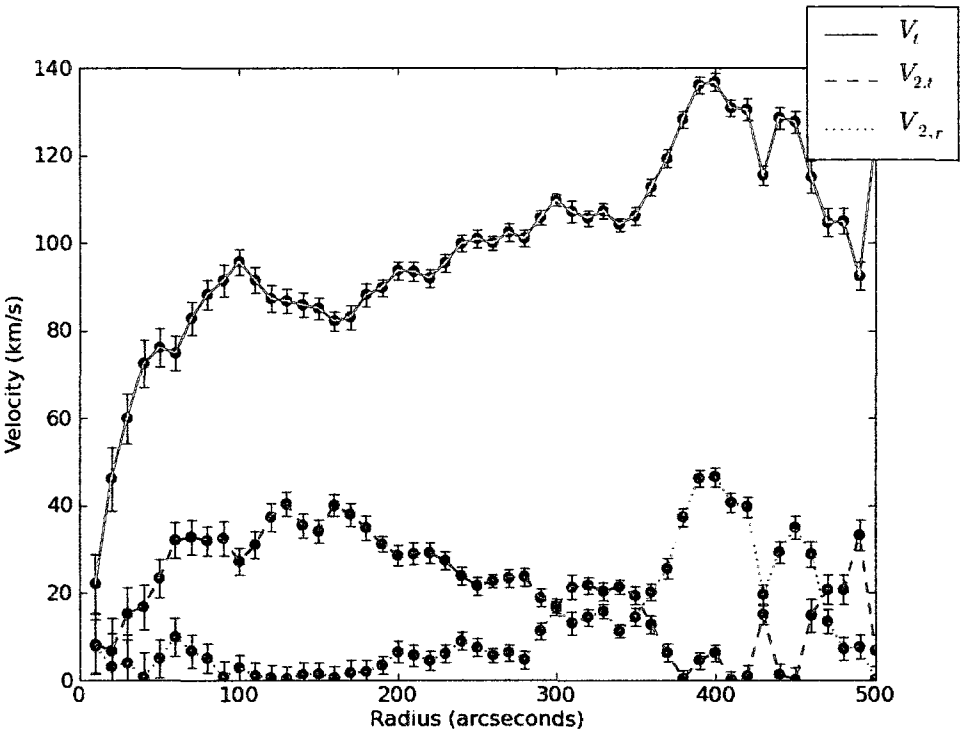

Figure 25 Same as Fig. 24, but for the eastern half of the H I dataset

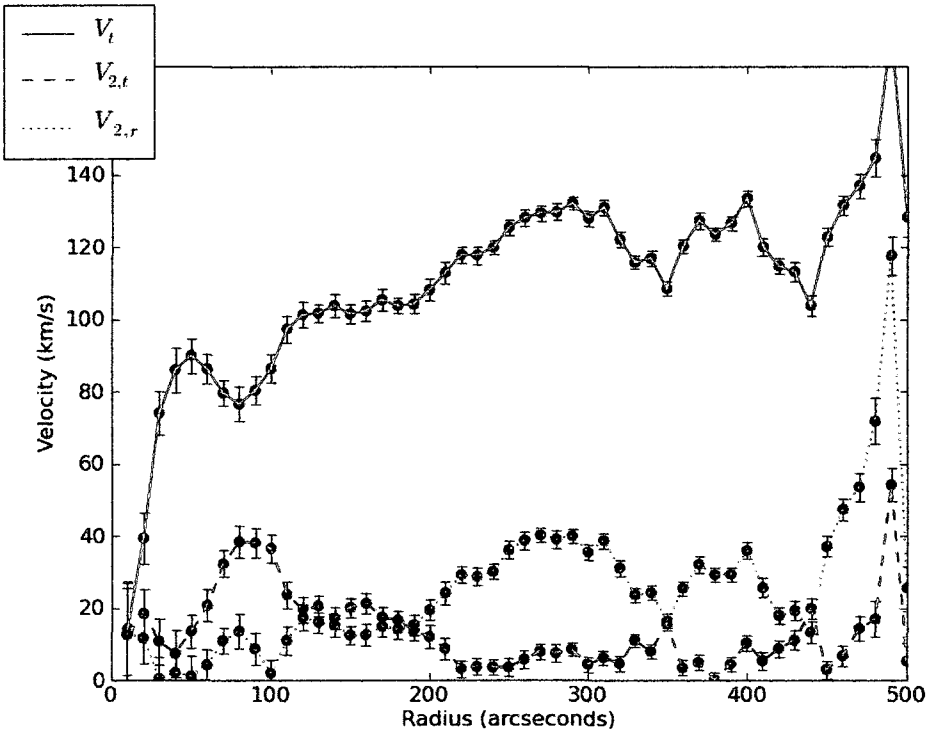

Figure 26 Same as Fig. 24 but for the western side of the H I dataset.

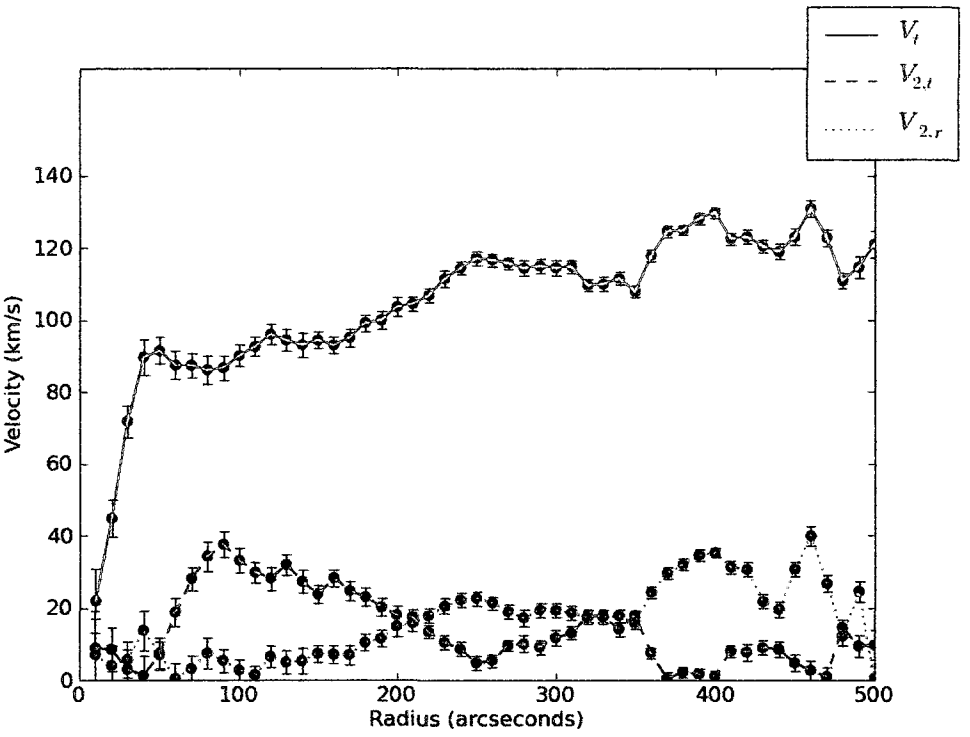

Figure 27 Same as Fig. 24 but for the southern half of the H I dataset.

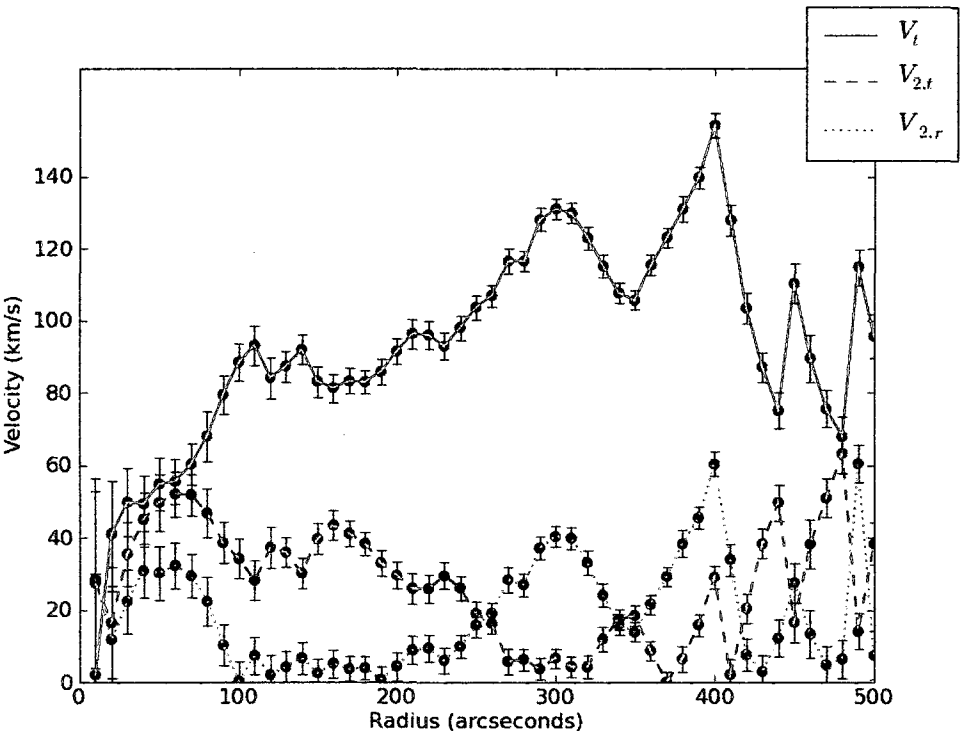

Figure 28 Same as Fig. 24 except for the northern half of the H I dataset.

the minor axis, the components of the non-circular motions that project along the line-of-sight are very small [$\cos(2\theta_b) \approx \sin(\theta) \approx 0$]. Because the net contribution to the model is small, Velfit can fit for large non-circular components that project in such a way as to account for deviations from circular orbits due to measurement error or turbulence in the disk. As well, if this model were to truly give us evidence for a bisymmetric distortion in the disk, we would expect to see similar rotation curves on both the E and W models, but this is not the case. The E dataset gives us a consistently lower rotation curve along the inner 300 arcseconds of the galaxy, and the features between the two sides are not consistent. This leads us to believe that the bisymmetric model's extra degrees of freedom, relative to the rotation-only and radial models, are allowing it to fit incoherent deviations from circular motion by applying a non-existent bar at a slight angle to the major axis. Results of the S and N fits support this hypothesis as they too solve for very small ϕ_b angles at $\phi_b = 8.01 \pm 0.11$ and $\phi_b = 3.81 \pm 0.07$ respectively. Although the rotation curves for these two cases are similar in their general shape, they too show large differences inside 300 arcseconds. By dividing the galaxy into E, W, S, and N halves we are able to convincingly rule out the bisymmetric model as a physically reasonable model for the H I data. The model provides a good statistical fit to the data by fitting deviations from circular motions along the major axis. However, while some deviations from circularity do exist in the H I dataset, they are not coherent bar-like flows that will bias the measured rotation curve.

3.2.4 CO

The pre-processed CO dataset was modelled using Velfit's rotation-only, radial, and bisymmetric models. The rotation curve acquired from the rotation-only model can be seen in Fig. 29 and the radial model components can be seen in Fig. 30. As with the Hα datasets, the bisymmetric model gave inconsistent results. The best-fitting parameters for the rotation-only and radial models are shown together in Table 3.

As with the two Hα datasets, the rotation curves for both models are almost identical and the radial flows are almost consistent with $V_r(r) = 0$.

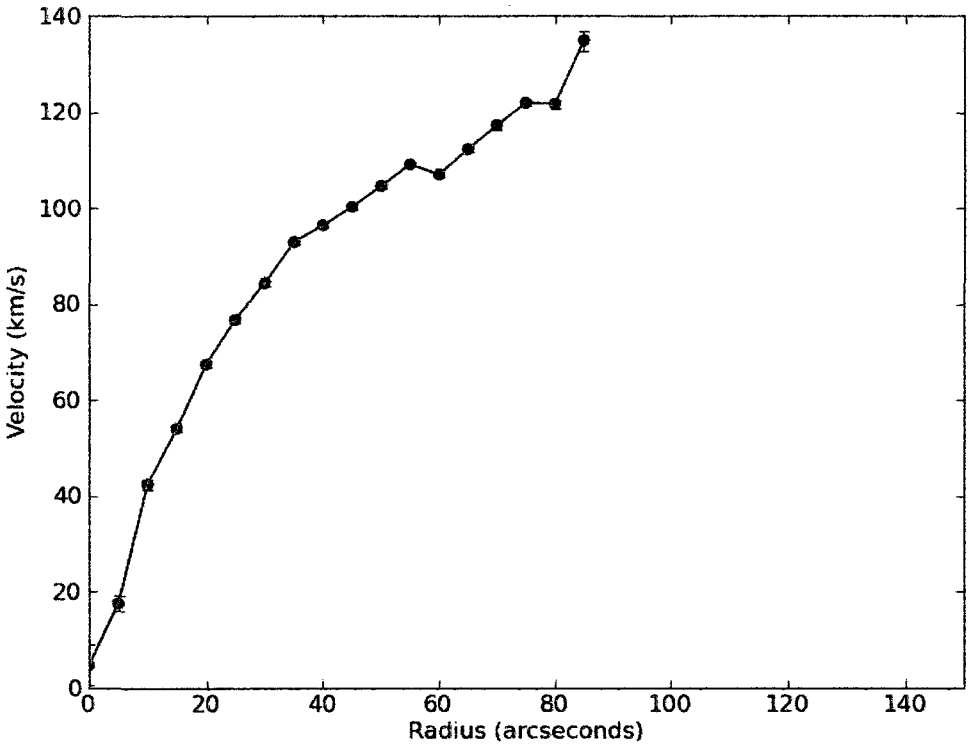

Figure 29 Same as Fig. 18 but for the CO dataset.

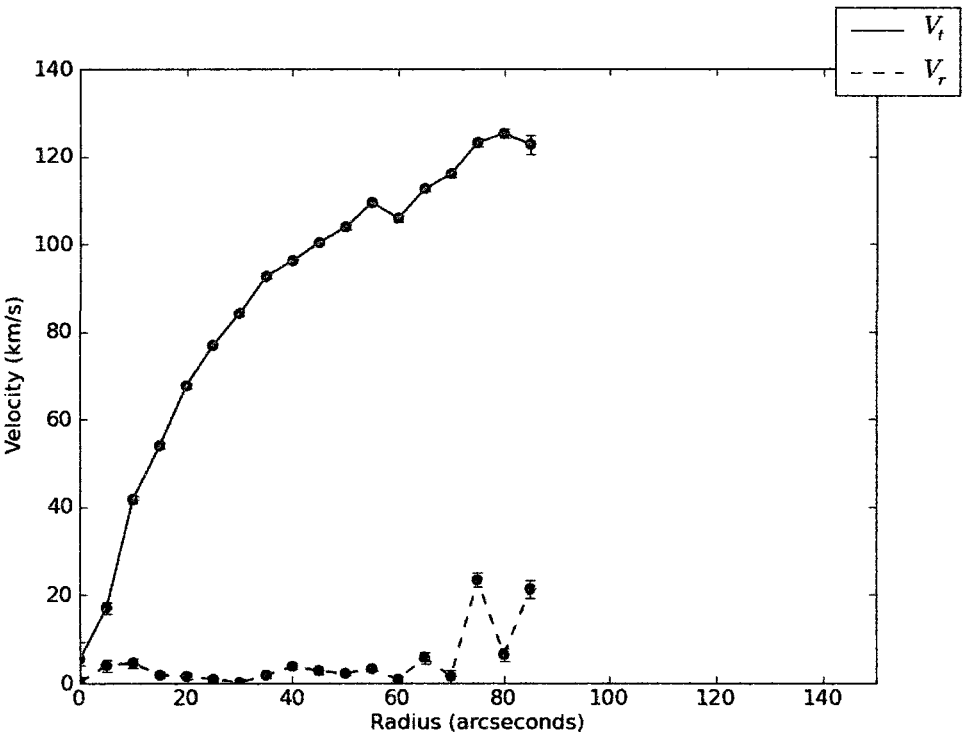

Figure 30 Same as Fig. 18 but for the CO dataset.

3.2.5 Discussion

A summary of all of the fit parameters for each of the datasets and models is shown in Table 3. Included in the table are the rotation-only and radial models for all four datasets, and the bisymmetric model for the H I dataset. In columns 3 and 4 we can see the solved values for the kinematic centre of NGC 6503 with respect to the photometric centre (values from Table 1). The Velfit procedure generates uncertainties for these values with no a priori knowledge of the angular resolutions of any of the datasets. With this taken in consideration, the solved values for x_c and y_c are similar between the H I, CO, and Hα - 1 datasets, though the centre of the Hα - 2 dataset seems anomalous. The systemic velocities in column 5 are similar, but do not exactly coincide with one another. The major discrepancy is seen in the CO dataset, but we did not correct for the fact that the CO radial velocities are relative to the local standard of rest, whereas velocities in the other datasets are heliocentric. The position angle, as seen in column 6, is constrained to less than 4° between all models and datasets. The inclinations shown in column 7, although not exactly coincident, are relatively well constrained. We therefore find reasonable agreement among the best-fitting parameters of the datasets, though some differences are larger than the tabulated uncertainties. This suggests that the error bars may be under-estimated by the Monte Carlo procedure adopted by Velfit.

For each of the dataset's radial model fit by Velfit, we concluded that the non-circular motions were essentially consistent with zero. At first glance, this assumption does not appear to be valid. At some radii the noncircular motions were obviously larger than zero, especially the last few data points (those for large values of r) even within the uncertainties. As was mentioned above, we believe that the uncertainties in the measured rotation curve may be under-estimated by Velfit. If this is the case, many of these non-circular components could still be consistent with zero. As well, if the radial velocities modelled by Velfit were representative of coherent radial flows, we would expect similar results across the four datasets. We do not see similar non-circular for all of the kinematic data thereby further suggesting that the modelled values for the non-circular motions are not representative of coherent radial flows. Finally, the increased velocity values (for both the circular and non-circular models)

for large values of r in each dataset may be attributed to mathematical artifacts from the code. These artifacts arise from fewer data points between the outer ring radii at which the velocity field components were extracted. For these reasons and those discussed previously, we adopt the rotation-only model to be the best fitting model to each of the kinematic datasets.

Fig. 31 shows all four datasets' rotation-only models. This plot shows to what extent the data coincide with one another. The advantage of H I is immediately evidently as the data extends well beyond not only the optical radius (dashed blue vertical line) but also the range of the other three datasets. The other datasets were needed in order to model the interior of the galaxy, and the importance of this can be seen from the slight differences with respect to the rising portion of the H I rotation curve. Despite the slight discrepancies between the Hα - 1 and Hα - 2 data seen in §2.3, Fig. 31 shows that they overlap almost perfectly for the rising portion of the rotation curve. We can also see from the CO data that dust extinction does not seem to be an issue, as it overlaps almost perfectly with the rising portion of the Hα rotation curves. We therefore confirm the tentative conclusion from §2.3 that the kinematics of the different tracers are consistent with one another.

3.3 Combination of the Data

The search for non-circular motions as described by §3.2 suggests that there are no significant radial or bisymmetric flows in NGC 6503. Any non-circular flows that are present are likely incoherent and at such a small scale that they should not bias the derived rotation curve. In addition the agreement between the best-fitting parameters for each dataset suggests that all are tracing the same disk kinematics. It is therefore with confidence that we combined our two Hα, H I, and CO together to form one master, multi-wavelength dataset to map the kinematics of NGC 6503.

All the data from the Hα - 1, Hα - 2, and CO datasets were combined together to make up the inner 120 arcseconds of the master dataset. Due to its lower resolution (in comparison with the other two tracers) in the inner galaxy, the H I data was only used at radii greater than 120 arcseconds. This master dataset was then run through Velfit in the same manner as all of the individual datasets. This is just to verify that

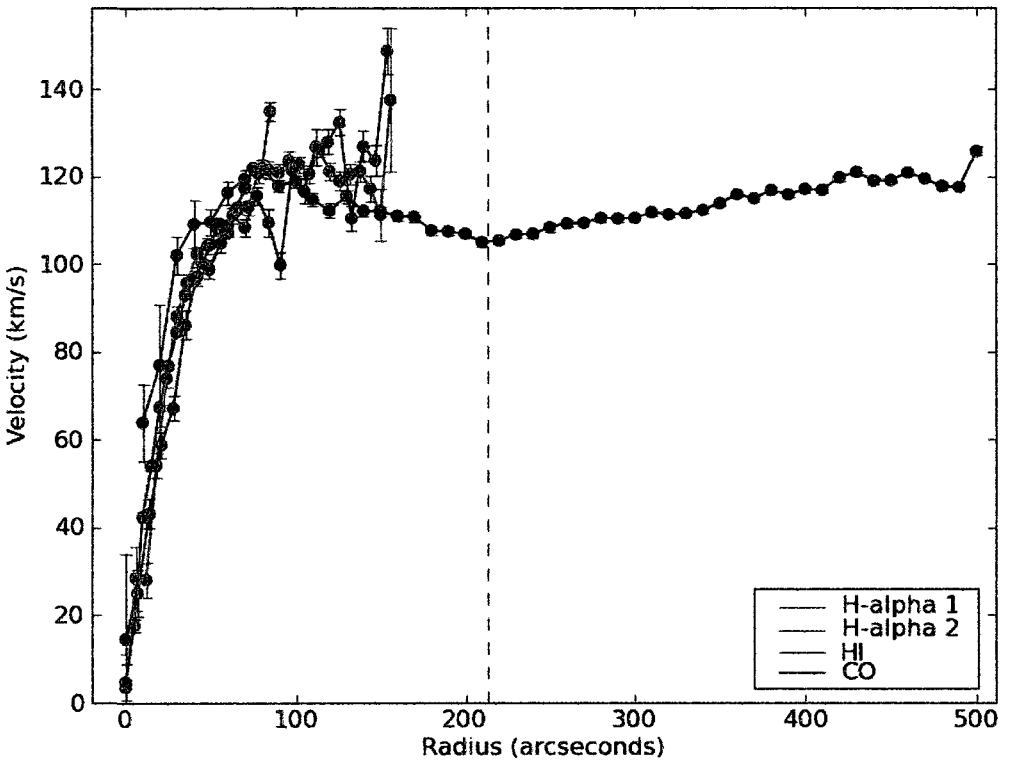

Figure 31 Rotation curves for the best-fit models (rotation-only in all cases) for all four datasets. The Hα - 1 dataset is shown in green, the Hα - 2 dataset is shown in red, the H I dataset is shown in purple and the CO dataset is shown in black. The vertical dashed blue line shows the edge of the optical disk for NGC 6503.

Table 3. Minimization Results for all 4 Datasets and the Master Dataset

Dataset	Model	x_c $''$	y_c $''$	$V_{\rm sys}$ $\rm km\,s^{-1}$	ϕ'_d $^\circ$	Inclination $^\circ$	ν	$\chi^2_{\rm r,min}$	ϕ_b $^\circ$
(1)	(2)	(3)	(4)	(5)	(6)	(7)	(8)	(9)	(10)
Hα - 1	Rotation	1.12 ± 0.29	0.56 ± 0.24	23.28 ± 0.50	121.01 ± 0.20	71.47 ± 0.36	604	1.19	...
Hα - 1	Radial	0.66 ± 0.24	1.24 ± 0.22	23.02 ± 0.41	119.67 ± 0.35	70.82 ± 0.33	588	1.12	...
Hα - 2	Rotation	-5.36 ± 0.30	-2.17 ± 0.33	19.20 ± 0.47	118.55 ± 0.24	67.62 ± 0.38	1293	4.75	...
Hα - 2	Radial	-5.84 ± 0.27	-2.19 ± 0.26	18.55 ± 0.43	117.50 ± 0.23	67.76 ± 0.35	1270	4.66	...
H I	Rotation	-2.53 ± 0.12	-5.56 ± 0.15	26.58 ± 0.06	117.41 ± 0.06	68.44 ± 0.02	8782	1.24	...
H I	Radial	-1.54 ± 0.22	-4.75 ± 0.11	27.04 ± 0.09	118.42 ± 0.07	56.17 ± 0.05	7915	3.65	...
H I	Bisymmetric	-0.61 ± 0.04	-3.06 ± 0.03	27.76 ± 0.05	117.34 ± 0.04	68.26 ± 0.03	2834	0.21	22.86 ± 0.25
CO	Rotation	0.81 ± 0.09	-1.17 ± 0.05	45.93 ± 0.19	120.56 ± 0.09	64.98 ± 0.06	4635	1.22	...
CO	Radial	0.9 ± 0.08	-1.34 ± 0.04	45.87 ± 0.17	121.67 ± 0.19	65.75 ± 0.10	4617	1.14	...
Master	Rotation	-2.82 ± 0.18	-1.98 ± 0.09	34.20 ± 0.38	117.5 ± 0.06	68.45 ± 0.11	7850	4.49	...

Note. — Col. (1): Dataset. Col. (2): Model. Col. (3): Right Ascension of disk centre modelled by Velfit, relative to the centre as quoted in Table 1. Col. (4): Declination of disk centre modelled by Velfit, relative to the centre as quoted in Table 1. Col.(5): Disk Systemic Velocity. Col.(6): Disk Position Angle. Col.(7): Inclination. Col.(8): Number of degrees of freedom in the minimization. Col.(9): Minimum value of reduced $\chi^2_{\rm r}$ of the best-fit model. Col.(10): Angle of the bar axis found in the bisymmetric model.

the conclusions made for each of the of the individual datasets hold for the master dataset as well.

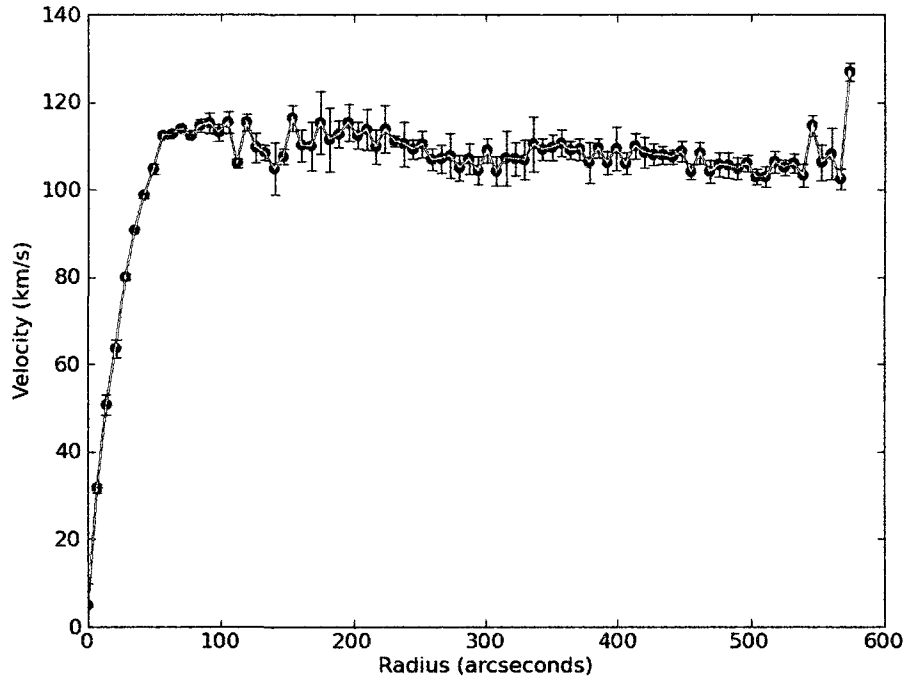

Figure 32 Same as Fig. 18 but for the master dataset.

The results for the rotation-only model can be seen in Fig. 32 and the radial model in Fig. 33. When comparing the two we see that $V_t(r)$ for each model are nearly identical. As well, $V_r(r)$ for the radial model shows that the possible radial flow amplitude is consistent with zero. Since beyond 120″ (and therefore across the majority of the master dataset) the data stem from H I, and in §3.2 we ruled bisymmetric flows in that tracer, we can rule it out for the master dataset as well. We therefore adopt the rotation curve from the rotation-only model, as derived through Velfit, as the master dataset in the mass modelling of § 5.

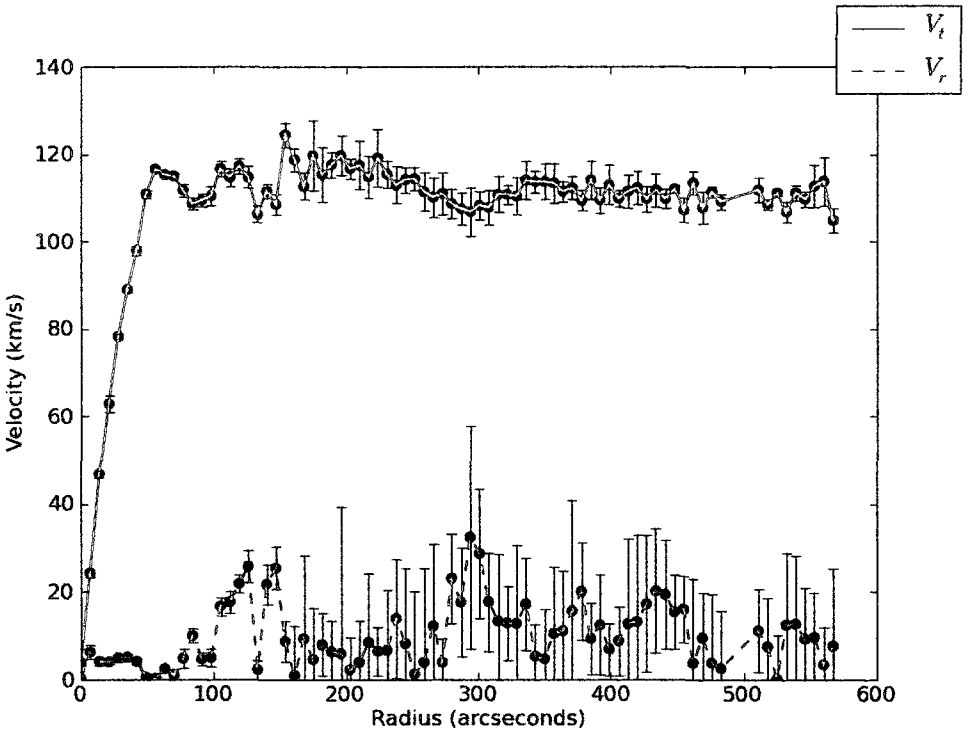

Figure 33 Same as Fig. 19 but for the master dataset.

4 Chapter 4 - Photometry

In order to model the distribution of stellar mass in NGC 6503 it is necessary to consider the photometry in the optical and infrared bands. Some photometric data exist in the literature in V- and I-bands (Héraudeau and Simien, 1996), B- and R-bands (Bottema, 1989), and J-, H-, and K-bands (2 Micron All Sky Survey; Jarrett et al., 2003). To complement these data and to probe the older stellar population that contains most of the mass (§1.3), deeper K-band photometry was needed to probe the surface brightness profile to fainter levels in the outer disk, where it can exhibit changes in slope. For that reason, the near-infrared observations, introduced in §2.2.5 and shown in Fig. 13, were taken using the CFHT's WIRCAM. The extraction of a surface brightness profile from these data is described in §4.1 and the unit calibration of the profile is described in §4.2. The K-band data extend those from 2MASS by more than 50″ in radius; we discuss the properties of this profile in §4.3.

4.1 Surface Brightness Profile Extraction

In order to generate a surface brightness profile from the CFHT K-band data, the IRAF task ELLIPSE of the STSDAS package was used. ELLIPSE is a task which fits elliptical isophotes to galaxy images. It reads in two-dimensional images and provides an output, in table format, containing the detailed characteristics of each fitted ellipse, with each row representing an individual ellipse. ELLIPSE therefore assumes that the galaxy is axisymmetric, which is justified for NGC 6503 since there are no coherent non-circular flows. The other assumption that is made is that photometric features, at the inner region of NGC 6503, such as a bulge or a minor bar will not affect the fit. The task begins with an initial guess for the position angle (PA), ellipticity, and centre value of the galaxy (input by the user) and iteratively samples the image in concentric ellipses. This produces a one-dimensional intensity distribution. The task can also be run while keeping the input values of PA, ellipticity, and centre constant. This is of particular interest for us since we have gone to great lengths with our H I, Hα, and CO data to derive these characteristics using Velfit (§3).

4.1.1 Foreground/Background Stars

Before carrying out isophotal calculations on the K-band image, we needed to remove foreground stars (i.e. stars in our own Galaxy along the line of sight to NGC 6503). A bad pixel mask was created interactively through the ELLIPSE task to eliminate pixels contaminated by foreground stars in the fitting process. This bad pixel mask acts in the same way as the Hubble Space Telescope Data Quality Files. In this bad pixel mask, pixels are assigned a value of 1 or 0; zeroed pixels are included in the fits, while non-zero pixels are blanked during the fitting process. In addition to the small foreground and background contributions, a major source that needed to be masked out was the star HIP 87295 (shown in Fig. 13 and 34 to the left of NGC 6503). This star has an apparent magnitude of +8.61 and therefore means that it is 4.33 times brighter than the total integrated light of NGC 6503 itself (assuming an apparent magnitude of +10.2 for NGC 6503) and even more so than the outer disk that we are trying to probe. Due to the proximity of HIP 87295 to NGC 6503 on the sky and its brightness, we need to mask it out so that it does not affect the outer disk

surface brightness calculations. The star itself and the major portions of its diffraction spikes were flagged in the bad pixel mask. The seam between adjacent WIRCAM chips were also flagged in the bad pixel mask since it was noticeably brighter than the background in the image. The final bad pixel mask that was used in the fitting procedure is shown in Fig. 34.

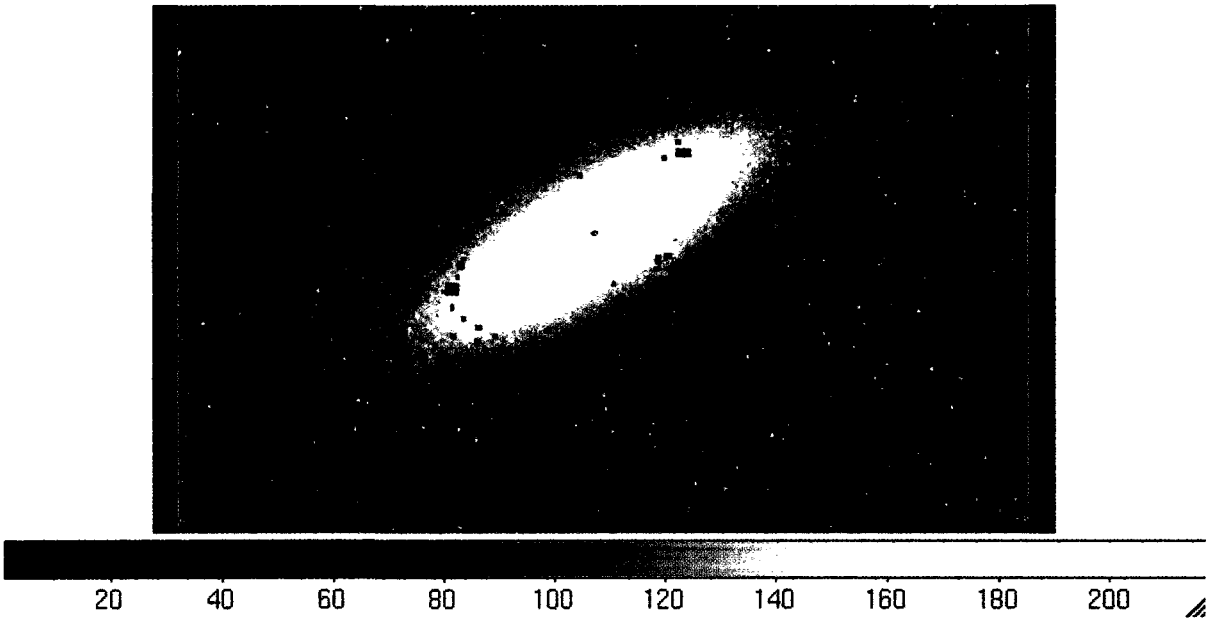

Figure 34 The bad pixel mask (red squares) used in the Iraf task ELLIPSE's fitting procedure over top of the histo-equalized image of NGC 6503. The large red square on the left edge of the image is the masked star HIP 87295. The masked seam between the CCD chips is shown as the horizontal line on the bottom of the image and the vertical line to the right of the galaxy.

4.1.2 Running Ellipse

The initial values for the position angle, ellipticity and centre for ELLIPSE were taken directly from the Velfit output of the rotation-only case for the combined multi-wavelength dataset (as seen in Table 3) in order to maximize consistency between the photometric and the kinematic analyses. The program computed an ellipse at every pixel in the radius direction from 0 to 1300 pixels. This corresponded physically to a surface brightness profile that extends up to 397 arcseconds, although beyond 279 arcseconds (which corresponds to approximately 7 kpc) the profile is dominated by sky noise.

An example of an isophotal fit where all the parameters are kept constant is

shown in Fig. 35. In this example the contours are fit every 30 pixels (instead of every pixel) solely for visual representation of the ellipses.

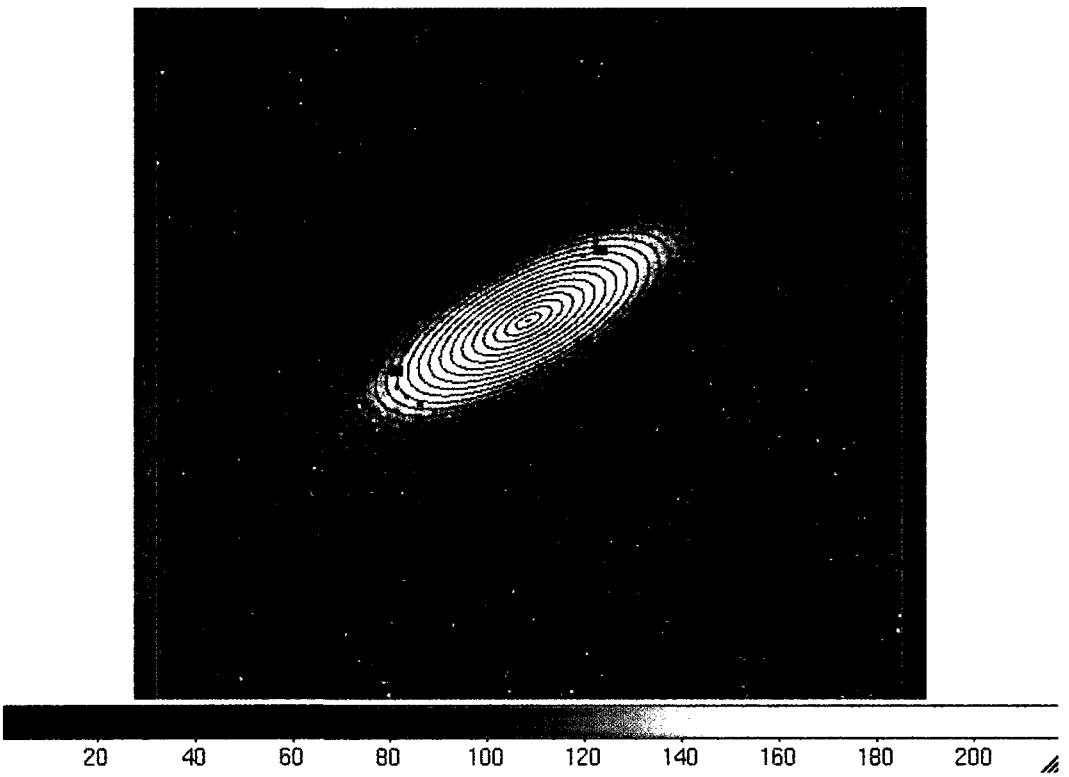

Figure 35 Example of output from the IRAF task, ELLIPSE, where the disk parameters are held constant across the disk and the contours are calculated every 30 arcseconds solely for visual purposes. The surface brightness profile is taken as the mean surface brightness in each ellipse, corrected for inclination (see §4.2).

The task was run to represent three different scenarios. First ELLIPSE was run allowing all four parameters of the ellipse to vary as a function of radius. This gives us a point of reference to how these photometric parameters vary across the disk. Second, the task was run while keeping the PA and ellipticity fixed but allowing the centre to vary. This provided a check of the consistency of the photometric and kinematic centres, particularly since the resolution of the photometric data is higher. Finally, the task was also run keeping all of the parameters fixed to the values obtained by Velfit. This allows us to obtain a surface brightness profile that is consistent with the rotation curve obtained from the kinematic analysis.

4.2 Surface Brightness Profile Calibration

4.2.1 Background Sky Value

In order to properly derive the surface brightness in $\frac{mag}{arcseconds^2}$ we needed to have an accurate representation of the background surface brightness value for our image. Systematic gradients in background level across the image were subtracted during the data reduction and we therefore subtracted a fixed value from the image. It was evident from random sampling of the image that the background value was approximately 462-463 counts/second. In order to determine the background level more precisely, the average pixel values of 15 different regions of the image were computed. Areas containing emission from NGC 6503 were avoided. Nine unique areas were chosen (three in the upper left corner, three in the lower right corner, two in the upper right corner, and one in the lower left corner) regardless of foreground star contamination. The remaining six areas were taken (three in the upper left and two in the lower right) with the intention of avoiding foreground stars. The median of these values resulted in a background value of 462.556 counts/second and this value was used as the background level in future calculations.

4.2.2 Derivation

The output of the ELLIPSE task gives us the intensity of each isophote in the fit. We needed to convert it from counts/second into the desired standard ($\frac{mag}{arcseconds^2}$). To do this we had to use the exposure time of each individual image, the pixel scale of the image, the zero point of the magnitude scales, the first order extinction coefficient (a parameter which depends on the properties of the local atmosphere and wavelength of light), and the airmass (the amount of atmosphere one looks through when observing a target, an airmass of one represents a target at zenith). The final surface brightness profile is defined by Courteau (1996):

$$SB = -2.5\log(s^2[F_T - F_S]/t_{exp}) + ZP - (K_k X) \quad \frac{mag}{arcsecond^2} \tag{15}$$

where the F_T is the intensity value of the isophote, the F_S is the background value of the image in counts/second (462.556), t_{exp} is the exposure time of each individual

exposure (15 seconds), s is the pixel scale of the image (.306 arcseconds/pixel), ZP is the zero point of 20.037 $mag/arcsecond^2$, K_k=0.033 mag/arcsec is the first order extinction coefficient, and X=1.629 is the airmass.

Using the centre varying dataset for the reasons described in §4.3, we cut off all data after 7 kpc (279 arcseconds) in order to use only the ellipses which are completely contained within the CFHT image. Beyond 7 kpc, the profile approaches the noise limit of the image and the data does not provide a reliable surface brightness profile. In order to transform these data into a form in which they can be used for mass modelling in ROTMAS (§5), we needed to convert the profile units from $\frac{mag}{arcseconds^2}$ to $\frac{L_{\odot,K}}{pc^2}$, where $L_{\odot,K}$ is the luminosity of the sun in the K-band. This is done using (Binney and Merrifield, 1998):

$$SB\left(\frac{Luminosity}{pc^2}\right) = 10^{\left(SB\left(\frac{mag}{arcseconds^2}\right)-3.28-21.572\right)/-2.5} \tag{16}$$

and assuming that the solar absolute magnitude in the K-band is 3.28 (Binney and Merrifield, 1998, Table 2.1).

4.3 Results

Fig. 36 shows the surface brightness profiles derived from ELLIPSE for each of the three scenarios described in §4.1, compared with the K-band 2MASS data. Fig. 37 shows how the four parameters (x_c, y_c, ellipticity, and PA) vary with radius when none are fixed. It is not surprising that there is a decrease in ellipticity and a change in the position angle in the inner profile. There is a small bulge at the centre of NGC 6503, as can be seen as the sharp decrease in the surface brightness profile in Fig. 36 at r< 20″. There is also a kink at $r \simeq 45''$ in the profile (the slightly rising feature after that of the bulge) studied by Freeland et al. (2010) who attribute it to a ring formed by a small edge on bar. The effect of these features on our mass models is expected to be small and their study is beyond the scope of this thesis. It should also be noted that the increase in profile noise with radius in Fig. 37 and 36 is expected since as the galaxy gets fainter it is harder to pull information out of the background noise.

All in all, the variance seen in Fig. 37 is tolerable considering that all of the

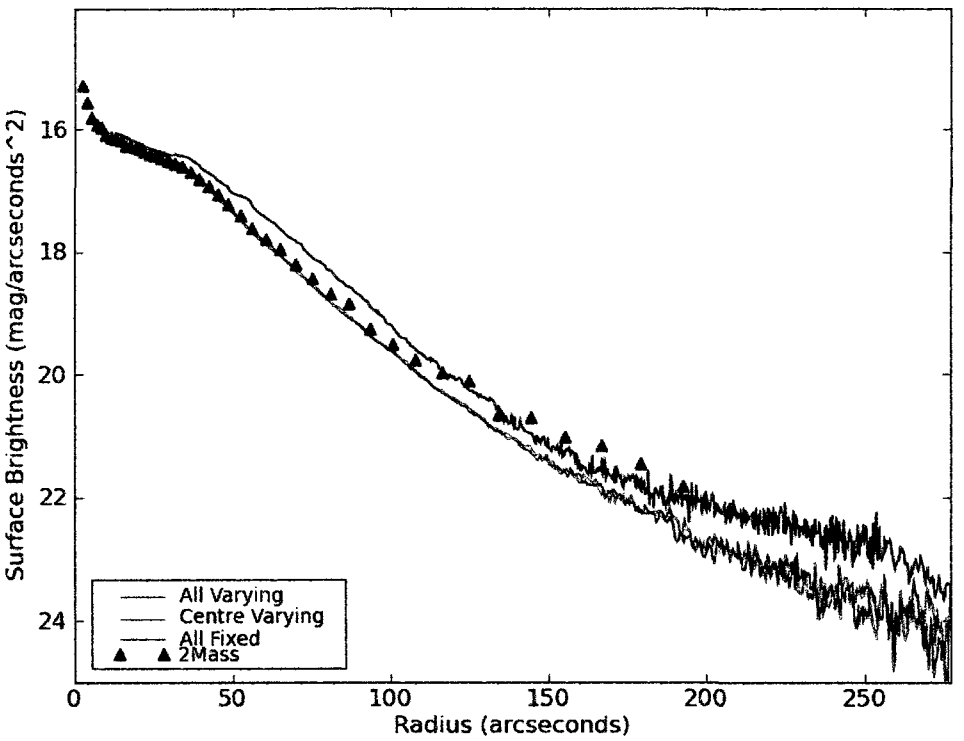

Figure 36 Surface brightness profiles derived from ELLIPSE when the disk PA, ellipticity, and centre were allowed to vary (solid blue line), just the centre was allowed to vary as a function of radius (solid green line), and when all variables were fixed to the kinematic values obtained by Velfit (solid red line). The literature 2MASS K-band data (Jarrett et al., 2003) are also shown (blue triangles).

parameters are assumed constant in Velfit. To compare with those values solved for by Velfit, Fig. 37 shows those values as horizontal black lines. A similar test was run to show the variance when just the centre values were allowed to change, and it was found that they settled on constant values essentially equivalent to the Velfit values within a few arcseconds.

The overplotted 2MASS surface brightness profile (blue triangles) in Fig. 36 also demonstrates an important motivation for our acquisition of a deeper dataset in the K-band. Extrapolating the 2MASS data into the outer disk would have significantly overestimated the stellar surface density. As can be seen from Fig. 36, when all the variables are fixed (as opposed to when the program has free range over all of the variables) there is a significant difference in the surface brightness profile. For consistency with the kinematic analysis of §3, however, we adopt a profile with the inclination and position angle fixed. Since the surface brightness profiles derived by

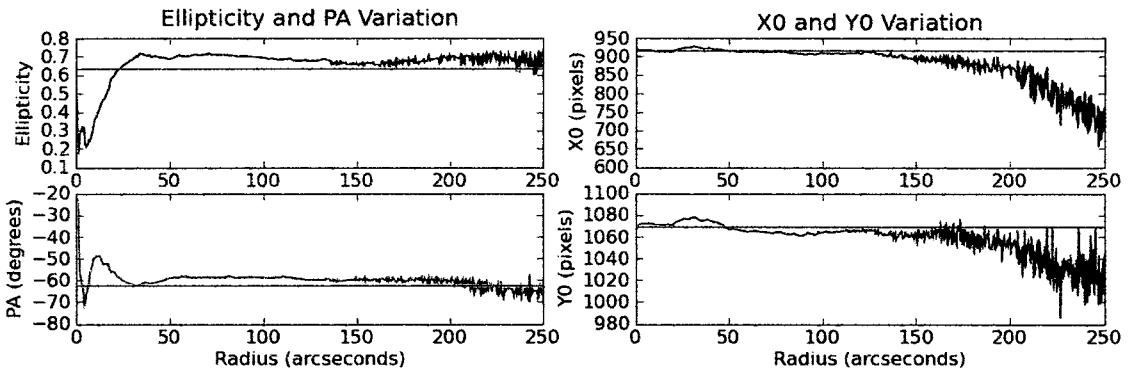

Figure 37 Variation in all disk parameters from ELLIPSE when all are allowed to vary. The right hand column shows the variation in the value of the centre with increasing radius and the left hand column shows the variation in PA (bottom) and ellipticity (top) with increasing radius. Horizontal black lines show the values for the parameters as solved by Velfit's multi-wavelength master dataset.

fixing all parameters and allowing the centre to vary are very similar Fig. 36, we proceed to use the one derived by allowing the centre to vary in our mass models of §5, since the photometric data we have has a higher resolution than the kinematic data used in Velfit program to calculate the centre coordinates of NGC 6503. If we were to choose the surface brightness profile where all the physical parameters were allowed to vary with radius, the value for m_d in the mass modelling of §5 would be affected. Since the blue curve in Fig. 36 is brighter than the red and green curves through all radii, the stellar contribution to the rotation curve is increased over all radii. This means that if the blue curve was used, a lower mass-to-light ratio would be obtained than if the red or green curve were chosen. Similarly, if the 2MASS surface brightness profile were to be used in the mass modelling, the stellar contribution to the rotation curve beyond approximately 120″ would be larger (although within 120″ it would be the same as the centre varying case).

5 Chapter 5 - Mass Modelling

Our detailed kinematic analysis in §3 showed no evidence for coherent non-circular flows in NGC 6503 and produced a multi-wavelength rotation curve. Our photometric analysis in §4 yielded a surface brightness profile that extends beyond that available in the literature. We now proceed to constrain the mass-to-light ratio and halo structure in NGC 6503 using mass models (see §1). A description of the modelling code and its inputs are in §5.1 and §5.2, respectively, and the mass model outputs are described in §5.3.

5.1 ROTMAS/ROTMOD

In order to fit the dark matter halo in NGC 6503 with a variety of models, the task ROTMAS in the Gipsy package (Van der Hulst et al., 1992) was used. ROTMAS takes the master, multi-wavelength rotation curve as derived in §3 and the photometric profile derived in §4 as inputs, as well as gas and bulge kinematics if available. As was alluded to in §1, the program sums the contributions from the stellar disk rotation curve, the gas rotation curve and the rotation from an assumed dark matter profile (as described in §5.3) to match the observed rotation curve using:

$$V_t(r) = \sqrt{m_g\, V_g(r)^2 + \Psi\, V_d(r)^2 + V_u(r)^2} \tag{17}$$

where $V_t(r)$ is the rotation curve and $V_g(r)$, $V_d(r)$, and $V_u(r)$ are contributions to the rotation curve from the gas disk, stellar disk, and the dark matter halo respectively, m_g is a dimensionless scaling factor applied to $V_g(r)$, and Ψ is a dimensionless scaling factor such that $\frac{m_d}{\Psi} = 1 M_\odot / L_{\odot,K}$. We fix $m_g = 1$ in all of our models (see §5.2.3) ROTMAS performs a χ^2 minimization in the fitting process and outputs the best-fit value for the mass-to-light ratio (Eq. 17 above) and for the two free parameters in each of the halo models described in §5.3. The uncertainties on these parameters given by ROTMAS are taken such that all fit parameters within the error bars correspond to a 1σ result. However this does not mean that all the possible 1σ results are within these error bars when the fit parameters are correlated. Further discussion of this is found in §6.2.

5.2 Rotmas Inputs

5.2.1 Rotation Curve

The most important input into ROTMAS is the observed rotation curve derived in §3. This rotation curve, $V_t(r)$ in Eq. 17, is what ROTMAS is trying to match when summing the stellar, gas, and dark matter components in quadrature. The observed rotation curve from the rotation-only model of the multi-wavelength, master dataset is therefore imported into ROTMAS, the radial axis is converted to kpc from arcseconds where 40 arseconds is equal to 1 kpc (see Table 1). We have assumed a minimum uncertainty of 3 $\mathrm{km\,s^{-1}}$ on observed rotation curve points in order to account for random motions. Similarly to the value of Δ_{ISM} in §3.2 assuming a lower minimum uncertainty for the observed rotation curve is going to affect our χ^2 statistics throughout the fit. We are able to place this lower limit for two main reasons. First, due to random motions, turbulence, and broadening effects we do not believe that we can accurately measure the value of V_t to less than 3 $\mathrm{km\,s^{-1}}$. By imposing a lower limit for the uncertainties we are sure to take into consideration these dynamical effects on the galaxy. Second, by imposing a lower limit of 3 $\mathrm{km\,s^{-1}}$ we allow our best fit model below to obtain a $\chi^2_{\mathrm{r,min}}$ of approximately 1. As long as the other models (those that were not the best fit model) are reasonably close to 1 as well, we can compare the models statistically with respect to the best fit model.

5.2.2 Photometry

The stellar mass contribution derived from photometric rotation curve is the next major input into ROTMAS. In §4 we derived the surface brightness profile for the CFHT K-band data and converted this into a luminosity density ($\frac{L_{\odot,K}}{pc^2}$) in §4.2, where $L_{\odot,K}$ is the luminosity of the Sun in the K-band. Once in this form, these densities can be imported into Gipsy and converted into the stellar mass contribution expressed in velocity units using ROTMOD (built into ROTMAS). ROTMOD calculates the rotation curve for a truncated disk or any other supplied density law from the surface brightness profile by assuming a thin disk. Since we only have photometric data out to approximately 7 kpc (279″) ROTMOD extrapolates an exponentially declining

disk beyond this point. In all of our fits, beyond 7 kpc the galaxy is very dark matter dominated and the details of this extrapolation should not affect our results. Due to the large number of data points output by the Iraf task ELLIPSE (after the aforementioned truncation at 7 kpc there were 934 data points) we read in every fifth point in order to comply with the input array limits. This resulting stellar mass contributions corresponds to $V_d(r)$ in Eq. 17. It should also be noted that m_d is not constrained by the surface brightness profile and is one of the variables in the fit.

5.2.3 Atomic and Molecular Gas

The CO and H I surface density profiles were derived by Kristine Spekkens using the Gipsy task ELLINT. The profile was extracted along a position angle of 300° and with an assumed inclination of 72°, roughly consistent with the values determined by Velfit. Since the CO data has a much higher resolution than the H I data (see Table 2), the surface density profile was re-evaluated in ELLINT for the H I data so that the radii were coincident for both datasets and such that both datasets were sampled every 8 arcseconds. A total surface density profile for the gas data was created simply by taking the sum of the two datasets at overlapping radii. Finally, the gas data was also multiplied by 1.33 to account for primordial helium. This data were then read into ROTMOD, just like the photometric data, and converted into a gas mass contribution represented in Eq. 17 as $V_g(r)$, assuming a thin disk. Since the gas is optically thin and therefore the gas mass is a known quantity, the scaling parameter m_g is fixed as $m_g = 1$ during mass modelling.

5.3 Mass Models

ROTMAS has the option to fit for multiple models for the dark matter halo. By changing the $V_u(r)$ term in Eq. 17 we are able to fit for Hernquist, Isothermal, and NFW dark matter profiles. We also ran the mass model using Gipsy's provided model for MOND. With inputs specified in §5.2, the mass models constrain m_d and halo properties. All halo profiles have two free parameters. The number of degrees of freedom (ν) used by the χ^2 statistics is therefore the sum of the number of data points in the observed rotation curve (since adjacent points on the rotation curve are

individually free parameters which have an influence on the fit) and the three free parameters in the fit (m_d and the two halo parameters). Below, we first run maximum disk fits to the inner part of the rotation curve, then fit for a dark matter halo. In all cases the weights on the fits were taken as the error bars in the observational data. The best-fitting parameters for all our mass model fits are given in Table 4.

5.3.1 Maximum Disk Fits

We first use ROTMAS to estimate a maximum disk mass-to-light ratio for the galaxy. As discussed in §1.3, the assumption of a maximum disk provides an upper limit on the mass-to-light ratio and some studies suggest that disks are maximal. We take the definition of maximum to mean that there is no dark matter in the inner few kiloparsecs of the galaxy. We therefore take the dark halo mass contribution, $V_u(r)$, as zero in Eq. 17 and scale the value of m_d such that the peak of the photometric rotation curve is at approximately the same velocity as the maximum in the observed rotation curve. In order to more accurately allow Gipsy to perform its χ^2 analysis, only the inner 2.62 kpc of the input data were used in the fit. This eliminated any pull from the data points in the outer rotation curve where dark matter is clearly needed. We understand that the final fit for the maximal disk mass-to-light ratio, seen in Fig. 38, does not correspond well to the observed data; dark matter seems to be needed even at small radii to match the rotation curve shape of NGC 6503. As well, the maximum disk mass-to-light ratio modelled for here slightly overshoots the observed rotation curve although this does not affect the mass modelling performed below. The value of this maximum disk mass-to-light ratio was found to be $m_d = 0.27 \pm 0.02$ $M_\odot/L_{\odot,K}$. This value for the mass-to-light ration serves as a point of reference only; the disk was fit to the maximum value in the observed rotation curve. This does not physically imply a hole in the dark matter halo, but rather a maximum disk m_d to which we can compare our fits. In Table 4, we express m_d found for other fits as a fraction of this maximum value.

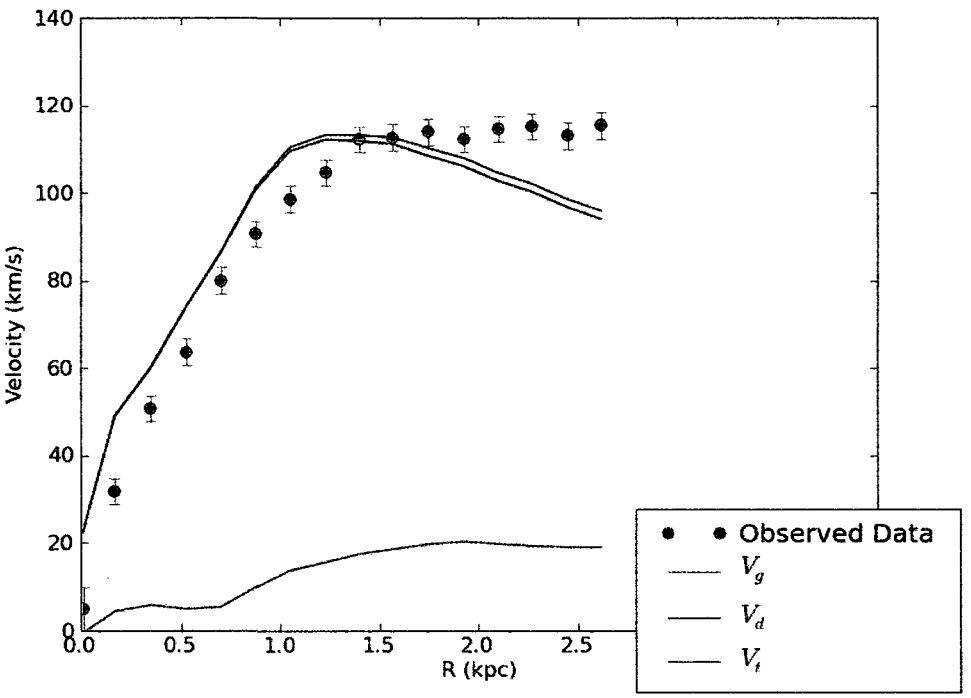

Figure 38 The maximum disk mass-to-light ratio fit for NGC 6503 from ROTMAS. The figure shows the contributions from the gas (green) and the photometric disk (purple) to make up a summed rotation curve (black) which is fit to the observed inner rotation curve (cyan).

5.3.2 Isothermal Profile Fits

The Isothermal profile is used for historical reasons since it is the simplest form for dark matter halos that gives a flat rotation curve. This empirical model has a density profile which goes as:

$$\rho_{ISO}(r) = \rho_0 \left[1 + \left(\frac{r}{r_c}\right)^2\right]^{-1} \tag{18}$$

where r_c is a core radius and ρ_0 is a constant central density. This spherically symmetric radial density profile gives rise to a halo rotation curve of the form:

$$V_u(r) = \sqrt{4\pi G \rho_0 r_c^2 [1 - (r_c/r)\arctan(r/r_c)]} \tag{19}$$

where the aforementioned parameters, r_c and ρ_0, are the halo parameters fit by ROTMAS. The results of fitting for m_d and this halo profile are shown in Fig. 39. In this figure the observed rotation curve is shown in cyan and the final $V_t(r)$ fit for the Isothermal model is shown in purple. The three velocity components which add in quadrature to equal $V_t(r)$ (Eq. 17) are also shown. The gas data is shown in green, the stellar disk is shown in black and the Isothermal dark matter halo is shown in blue. The best-fit values for the three free parameters are given in Table 4 and the χ^2 landscapes for the three free parameters are shown in Figs. 40, 41, and 42. In each of the plots the contours show different confidence intervals, derived from the χ^2 statistics as explained in §3.2. There is a clear correlation between the fit parameters, which we discuss in §6.2.

5.3.3 Hernquist Profile Fits

The Hernquist profile, introduced by Hernquist (1990), is a completely analytical model which closely approximates the de Vaucouleurs $R^{1/4}$ law. It is often used as an alternative to the isothermal sphere model as it allows for an analytic treatment of the distribution function. This model is given by:

$$\rho_{HERN}(r) = \frac{M_0}{2\pi R_0^2} \frac{1}{r(1 + \frac{r}{R_0})^3} \tag{20}$$

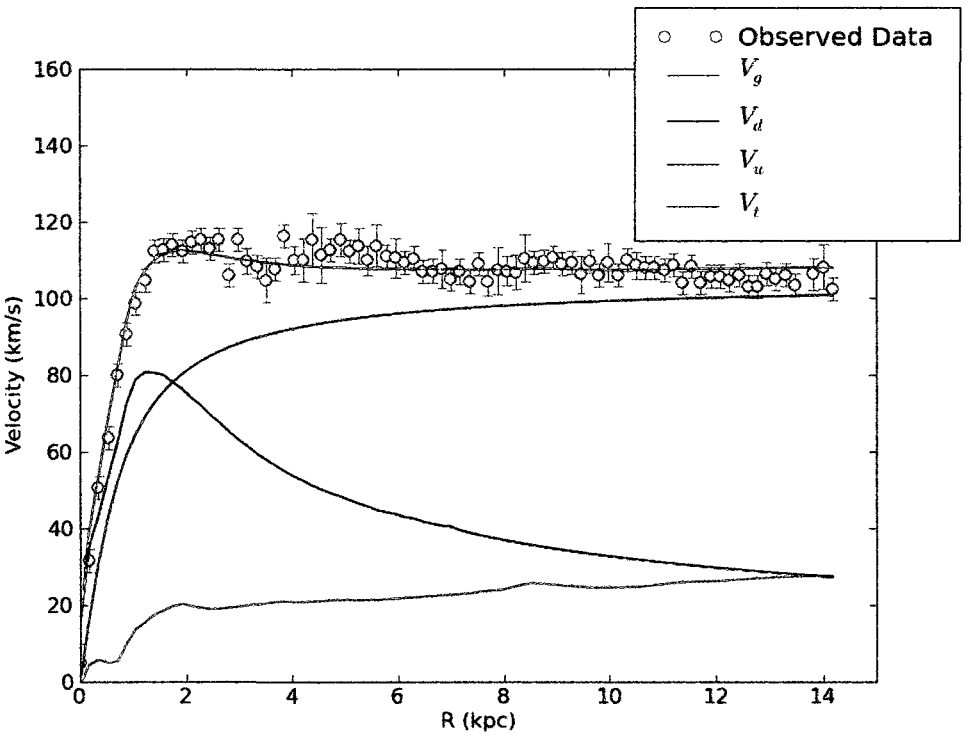

Figure 39 Mass model fit for the Isothermal dark matter profile. The multi-wavelength master dataset rotation curve is shown in cyan, the contribution from the dark matter halo is shown in blue, the stellar contribution is shown in black, and the gas contribution is shown in green. The sum in quadrature of the dark matter, stellar, and gas curves is given in red.

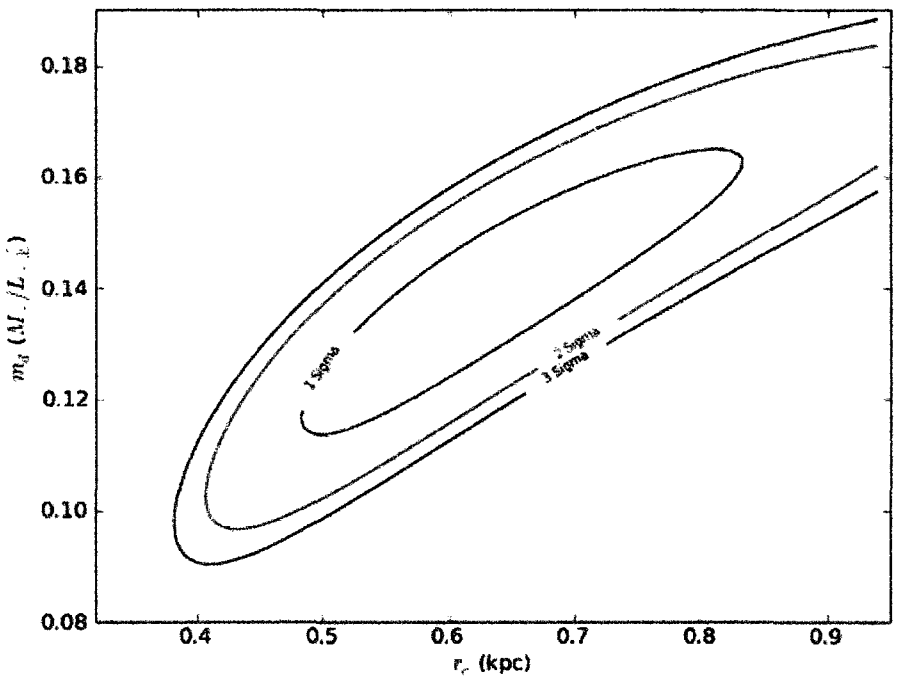

Figure 40 χ^2 landscape for the Isothermal halo core radius r_c and the mass-to-light ratio from the Isothermal profile fits. Contours show the fit values which are representative of a 1σ (red), 2σ (green), and 3σ (black) deviations from the bestfit.

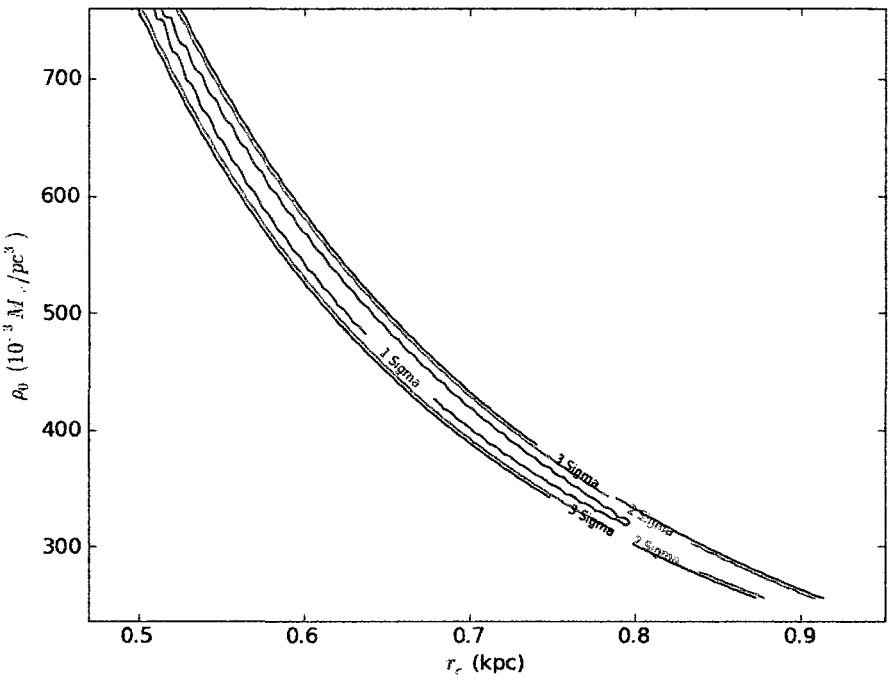

Figure 41 Same as Fig. 40 but for the Isothermal profile fit parameters r_c and ρ_0.

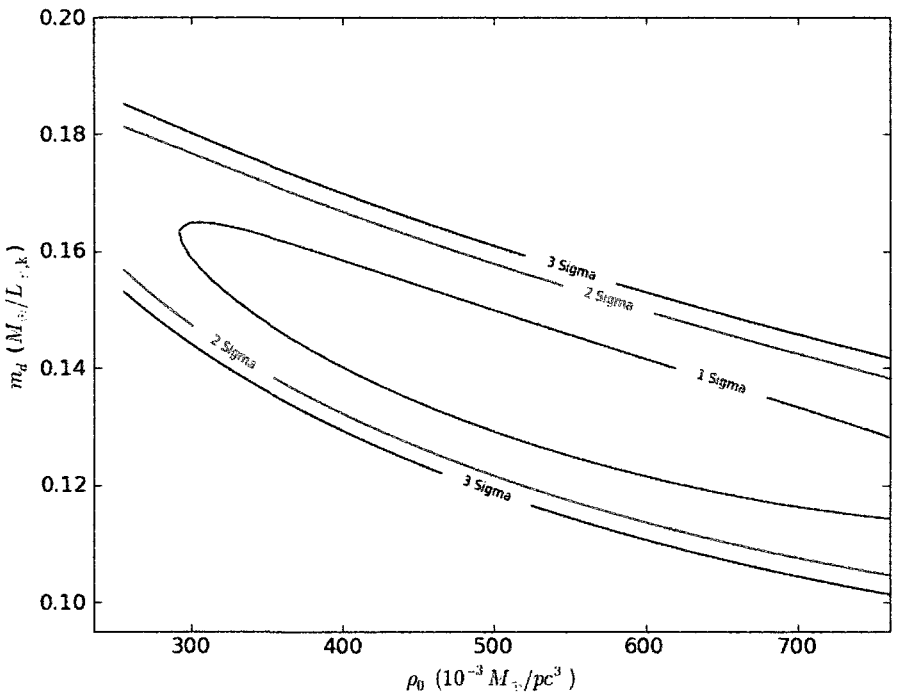

Figure 42 Same as Fig. 40 but for the Isothermal profile fit parameter ρ_0 and the disk m_d.

where M_0 is the total mass of the halo and R_0 is the truncation radius. This profile gives rise to a halo rotation curve with:

$$V_u(r) = \sqrt{G\ M_0\ 1e4}\frac{\sqrt{r}}{R_0 + r} \tag{21}$$

where the values R_0 and M_0, as defined above, are the free parameters for this model. The results of this fit are shown in Fig. 43 and the best-fitting parameters are given in Table 4. The χ^2 landscapes for the three free parameters are also shown in Figs. 44, 45, and 46.

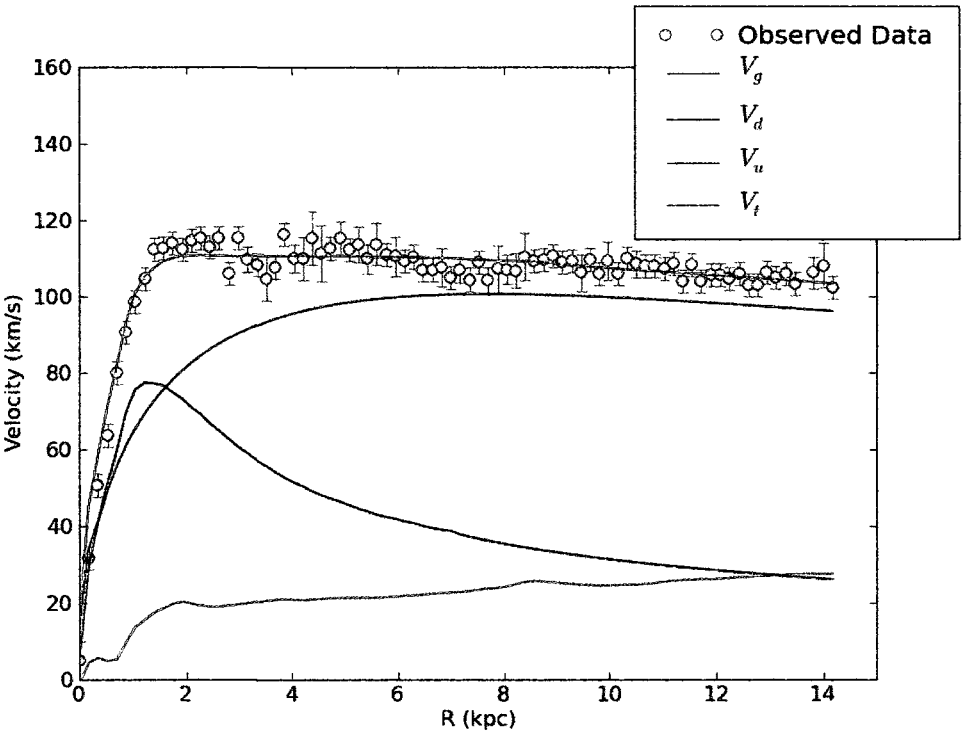

Figure 43 Same as Fig. 39 but for the Hernquist profile.

5.3.4 NFW Profile Fits

The NFW profile (Navarro et al., 1997), as introduced in §1.4, is an analytical dark matter halo profile motivated by cosmological N-body simulations. This model has a dark matter density profile that goes as:

$$\rho_{NFW}(r) = \rho_{crit}\left[\frac{\delta_0(c)}{cr/r_{200}(1 + cr/r_{200})^2}\right] \tag{22}$$

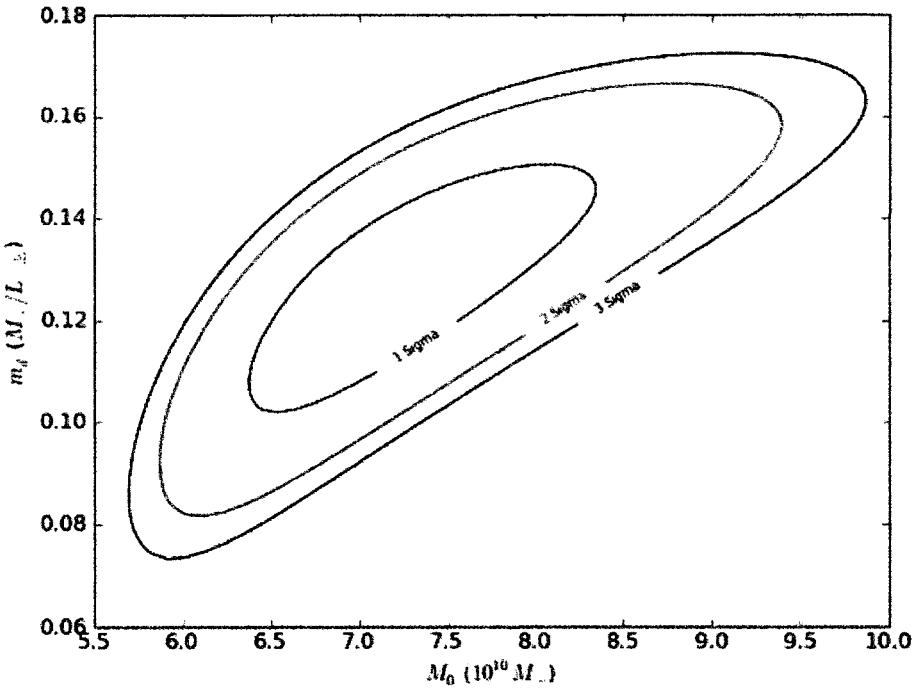

Figure 44 Same as Fig. 40 but for the Hernquist halo parameter M_0 and the disk m_d.

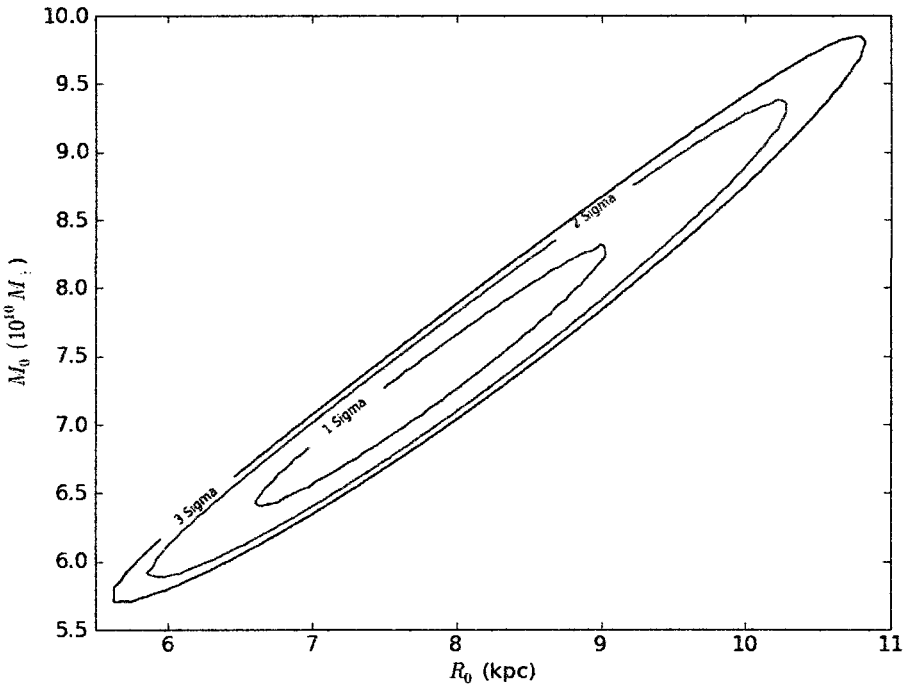

Figure 45 Same as Fig. 40 but for the Hernquist halo parameters R_0 and M_0.

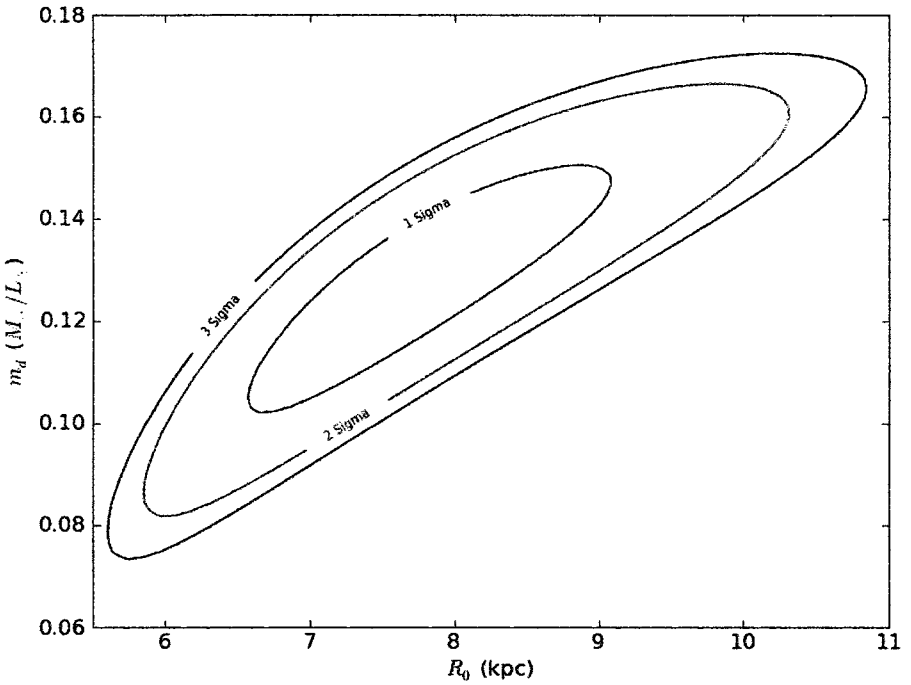

Figure 46 Same as Fig. 40 but for the Hernquist halo parameter R_0 and the disk m_d.

where ρ_{crit}, c, r_{200}, and δ_0 are as defined in §1.4. It is worthwhile to reiterate that a related parameter V_{200} can also be defined such that $r_{200} = \frac{V_{200}}{10H}$ [throughout this work adopt h=0.7 for our calculations, where $h = H/100$, which is consistent with current cosmological data (Komatsu et al., 2009)]. The NFW profile therefore has 2 independent variables. Using V_{200} and c as the free parameters, the halo rotation velocities can be defined as:

$$V_u(r) = \sqrt{\left(\frac{V_{200}^2}{x}\right)\left(\frac{\ln(1+cx) - cx/(1+cx)}{\ln(1+c) - c/(1+c)}\right)} \tag{23}$$

where $x = \frac{rh}{V_{200}}$. The results of this fit are shown in Fig. 47 and the best-fitting parameters are given in Table 4. The χ^2 landscapes for the three free parameters are shown in Figs. 48, 49, and 50.

Although N-body simulations, such as those from Navarro et al. (1997) predict that dark matter halos have essentially universal profiles, these simulations do not account for the formation of galaxies within halos. On average non-baryonic dark matter exceeds baryonic matter by a factor of $\Omega_{dm}/\Omega_b \approx 6$ in the Universe but at the

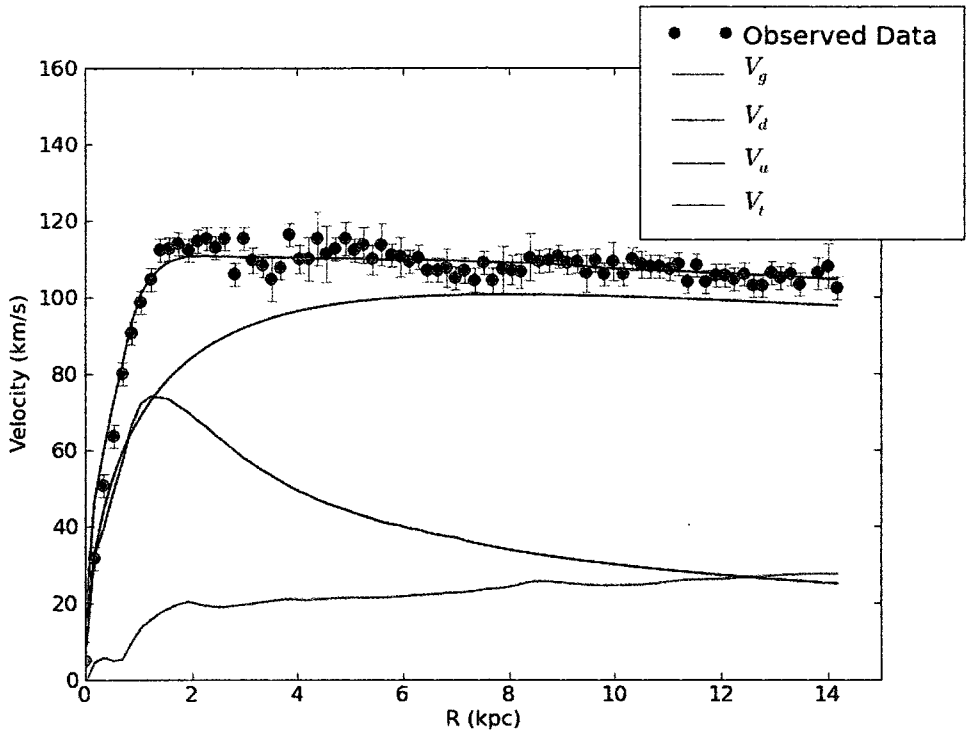

Figure 47 Same as Fig. 39 but for the NFW profile.

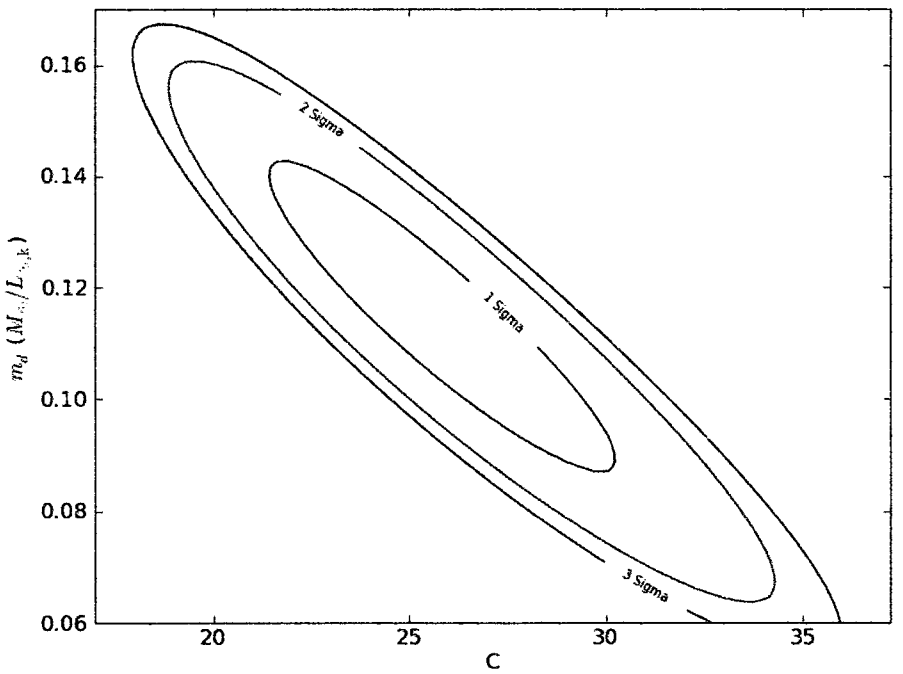

Figure 48 Same as Fig. 40 but for the NFW halo parameter c and the disk m_d.

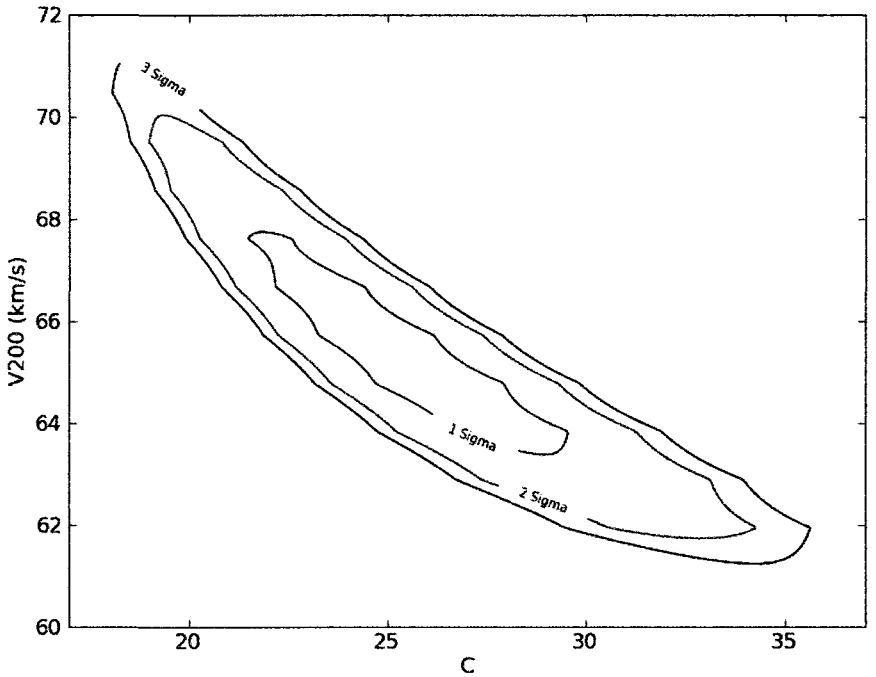

Figure 49 Same as Fig. 40 but for the NFW halo parameters c and V_{200}.

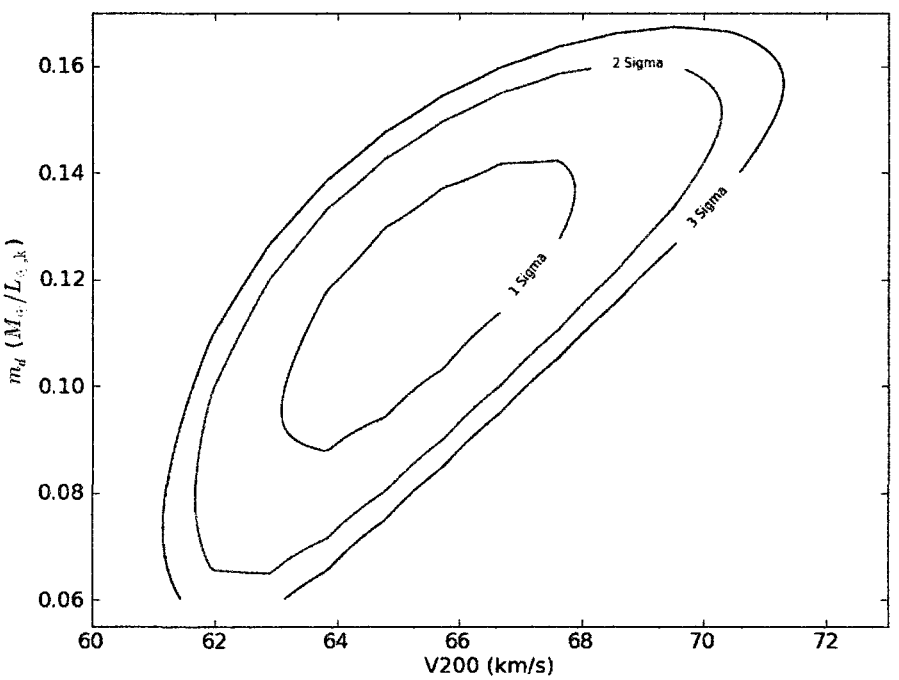

Figure 50 Same as Fig. 40 but for the NFW halo parameter V_{200} and the disk m_d.

centres of galaxies the density is dominated by stars (Gnedin et al., 2004). During the formation of a galaxy, as the baryons are in the process of condensing they pull the dark matter particles inward. This alteration of the dark matter halo would increase the density of dark matter in the central region relative to that predicted by collisionless simulations. A simple way to account for baryon collapse is to assume that the process occurs adiabatically. The current form of the model of adiabatic contraction was introduced and tested by Blumenthal et al. (1986) and is still routinely used for modelling galaxies. Assuming spherical symmetry, homologous contraction, circular particle orbits, and conservation of the angular momentum ($M(r)$=constant where $M(r)$ is the total mass enclosed within the radius r) the final dark matter distribution can be calculated by:

$$[M_{dm}(r) + M_b(r)]r = [M_{dm}(r) + M_b(r_f)]r_f \tag{24}$$

The final dark matter distribution is calculated given the initial mass profiles $M_{dm}(r)$, $M_b(r)$ and final baryon profile $M_b(r_f)$ (Gnedin et al., 2004). r_f is the final radius of the dark matter halo. Recent studies that relax some of the assumptions in the original Blumenthal et al. (1986) work suggest that Eq. 24 represents an upper limit on the impact of galaxy formation on the halo mass profile.

The ROTMAS NFW profile fits do not take adiabatic contraction into account. The next obvious step is to ask how this process affects the dark matter profile parameter fits. Since adiabatic contraction produces a more concentrated dark matter distribution, adiabatic contraction tends to worsen the discrepancy between theory and observations presented in §1.4 and specifically those of Fig. 7 (McGaugh et al., 2007). Preliminary tests for the effects of adiabatic contraction, using the publicly-available code contra (Gnedin et al., 2004), for our profile fits show only a relatively insignificant change in profile shape (and consequently only minor changes in c and V_{200}). We therefore make no attempt to correct the values listed in Table 4 for this effect and we return to this issue in §6.4.

5.3.5 MOND Fits

Gipsy also has a Modified Newtonian Dynamics (MOND) model built into ROTMAS. Briefly, MOND (Milgrom, 1983) seeks to explain the flat rotation curves of spiral galaxies by modifying the law of gravity (Eq. 6) at low accelerations rather than by invoking dark matter (see §1). This fits the data without a value for $V_u(r)$ (since that is representative of a dark matter component in a galaxy) and instead has a different value for $V_t(r)$ than was presented in Eq. 17. Instead, the summed velocity for the components in the MOND fit are described by:

$$V_t(r) = \sqrt{(m_g V_g^2 + m_d V_d^2)\frac{\sqrt{1+\sqrt{1+[2rA/(m_g V_g|V_g| + m_d V_d|V_d|)]^2}}}{\sqrt{2}}} \tag{25}$$

Since we fix $m_g = 1$ (§5.2.3), this model has only two free parameters: m_d and the acceleration scale A. The results of this fit are shown in Fig. 51, and the best-fitting parameters are given in Table 4. The χ^2 landscape for the 2 free parameters (A and m_d) is shown in Fig. 52.

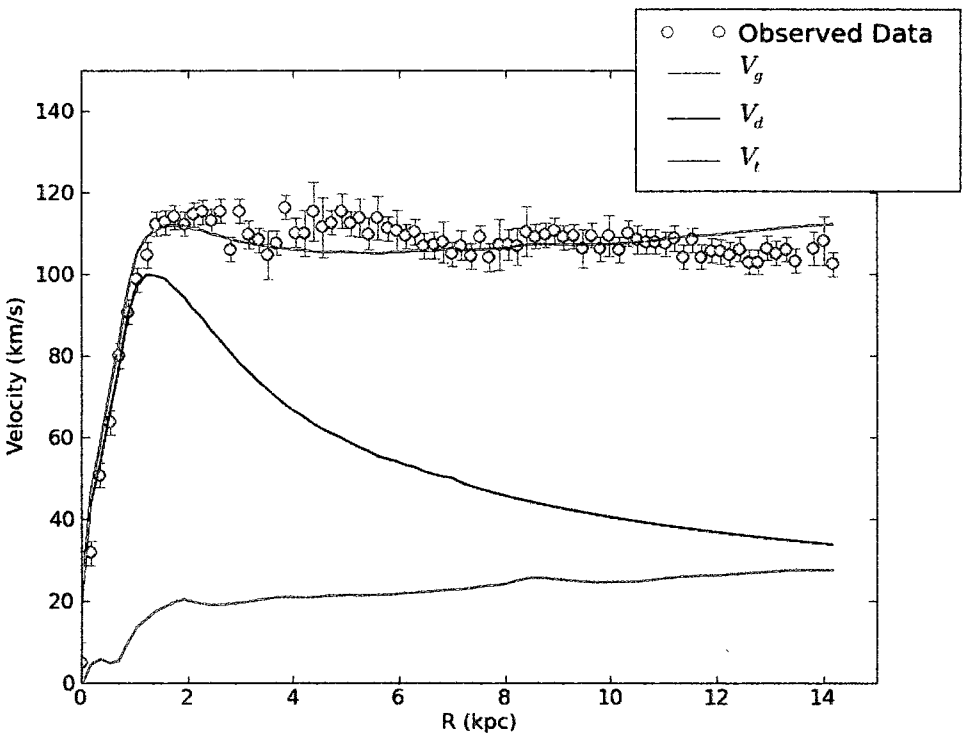

Figure 51 Mass model fit for the Modified Newtonian Dynamics (MOND) profile. The multi-wavelength master dataset rotation curve is shown in cyan, the stellar rotation curve is shown in black, and the gas rotation curve is shown in green. The gravitating mass from the stellar and gas rotation curves is given in red.

Table 4. Parameter Values Fit For Various Models in ROTMAS

Model	Parameter 1	Parameter 2	m_d $M_\odot/L_{\odot,K}$	% Max Disk m_d	$\chi^2_{\rm r,min}$
(1)	(2)	(3)	(4)	(5)	(6)
Maximum Disk			$m_d = 0.268 \pm 0.016$	100 %	13.8
Isothermal	$r_c = 0.626 \pm 0.158$ kpc	$\rho_0 = 510.97 \pm 253.055$ $(10^{-3} M_\odot pc^{-3})$	$m_d = 0.138 \pm 0.022$	51.5 %	0.98
Hernquist	$R_0 = 7.70 \pm 0.57$ kpc	$M_0 = 7.23 \pm 0.44$ $(10^{10} M_\odot)$	$m_d = 0.127 \pm 0.011$	47.4 %	1.12
NFW	$c = 25.45 \pm 2.35$	$V_{200} = 65.25 \pm 1.30$ km s^{-1}	$m_d = 0.116 \pm 0.014$	43.3 %	1.20
MOND	$A = -5824.44 \pm 293.45$		$m_d = 0.212 \pm 0.010$	N/A	2.37

Note. — Col. (1): Model. Col. (2): First free parameter for the given model, its solved value, and uncertainty. Col. (3): Second solved parameter for a given model, its solved value, and uncertainty. Col.(4): The solved value of the disk mass-to-light ratio Col.(5): Percent of maximum disk mass-to-light ratio for a given model assuming the solved maximum disk mass-to-light ratio is that from the Maximum Disk row. Col.(6): Minimum value of reduced χ^2 of the given model.

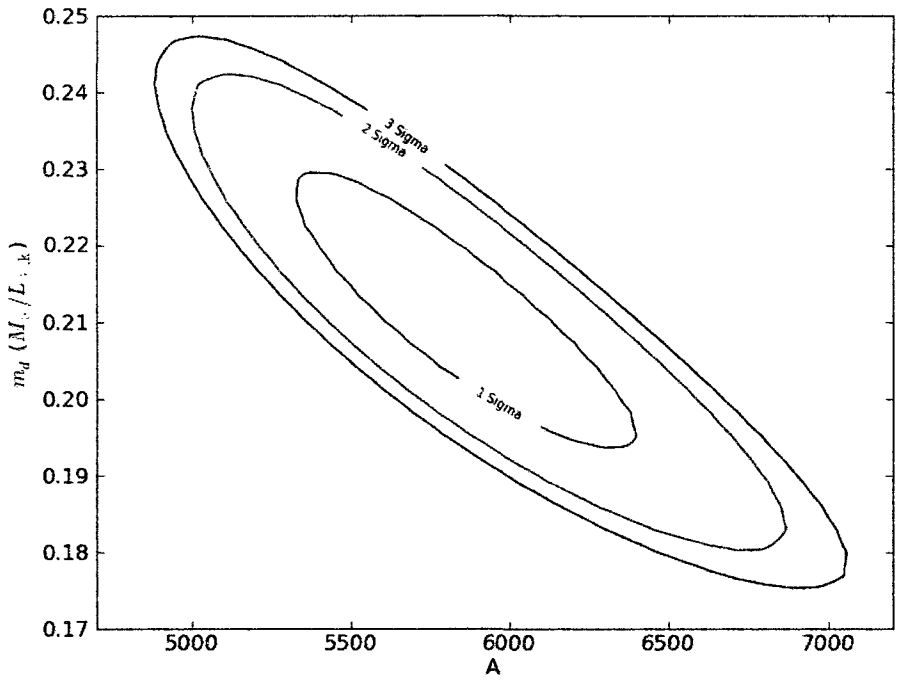

Figure 52 Same as Fig. 40 but for the MOND parameter A and the disk m_d.

6 Chapter 6 - Results and Discussion

A suite of mass models was evaluated in §5 to constrain the stellar mass-to-light ratio and dark matter halo properties of NGC 6503. Below, we discuss the implications of the fit results in the context of previous studies and cosmological predictions.

6.1 Halo Profile Fit Comparison

As can be seen from the best-fitting parameters in Table 4, each of the models, including a cosmologically motivated dark matter halo profile, produced acceptable fits to the observed rotation curve. In terms of the fit quality, the Isothermal halo fit was the best with $\chi^2_{\rm r,min}$= 0.98. Considering the χ^2 distribution statistics (see §3.2), however, the Hernquist profile fit is not statistically significantly worse than the Isothermal one. The NFW profile fit is statistically different from the Isothermal fit at approximately the 2σ level. Even though it is not the best-fitting profile, $\chi^2_{\rm r,min}$= 1.20 implies that a cosmologically motivated NFW halo is allowed by the data. We

discuss our results in the context of cosmological predictions in §6.4.

We note that the MOND mass model for NGC 6503 yields a much poorer fit to the data than models including a dark matter halo. While a full investigation of MOND models is beyond the scope of this thesis, the poor MOND fit to the data is unusual for a spiral galaxy (e.g. Sanders and McGaugh, 2002) and warrants further study.

6.2 χ^2 Landscape Contour Plots

Many interesting and significant conclusions can be made from the χ^2 landscape contour plots for each of the halo fits. Each of these contour plots are representative of the range of parameter values that fit the model equally well (within their respective contours). The degeneracy between m_d (the disk mass-to-light ratio) and the halo parameters is known as the "disk-halo degeneracy". We can see in Figs. 40, 42, 44, 46, 48, and 50 that for each of the different models, we can trade halo shape (parameter pairs [r_c and ρ_0], [R_0 and M_0], and [c and V_{200}]) for disk mass without sacrificing goodness of fit.

The contour plots more specifically show us how the mass-to-light ratio can vary for a given halo parameter's range of possible values. Although they seem to be indicative of a wide range of statistically equivalent values, it is interesting to notice how well constrained our mass-to-light ratio actually is. The NFW parameters (as seen in Fig. 48 and 50) constrain the mass-to-light ratio to values $\sim 0.09 < m_d <\sim 0.15\ M_\odot/L_{\odot,K}$ within 1σ. The Isothermal profile constrains the mass-to-light ratio to values $\sim 0.11 < m_d <\sim 0.17\ M_\odot/L_{\odot,K}$ within 1σ. Finally, The Hernquist profile constrains the mass-to-light ratio to values $\sim 0.10 < m_d \lesssim 0.15\ M_\odot/L_{\odot,K}$ within 1σ. Regardless of the halo model adopted, we therefore constrain m_d to a factor of 50%. Constraining the value of m_d with this accuracy allows us to say something about the maximality of the stellar disk in §6.3.

A traditional "banana plot" shape is seen in the χ^2 landscape contour plot for the two NFW parameters c and V_{200} in Fig. 49. This is a typical result (Bell and de Jong, 2001) and it signals a correlation between best-fitting values. Because of the aforementioned degeneracy between m_d and the halo, this relation between V_{200}

and c reflects how the halo is changing in response to varying m_d. This is one of the major issues plaguing mass modelling today. Equally good fits can be obtained for an increase in V_{200} and consequently a decrease in c. This being said, our NFW fit manages to constrain V_{200} to a range of approximately 10 $\mathrm{km\,s^{-1}}$ within 2σ. The concentration parameter c is not so well determined as it varies over a range > 15 within 2σ. The NFW fit is not the only one which exhibits a degeneracy between the halo parameters. The Isothermal contour plot for parameters ρ_0 and r_c also shows that even within 1σ, as r_c decreases by $\sim$0.4 kpc, the value of ρ_0 varies from $\rho_0 < 400$ to $\rho_0 > 700$ $10^{-3} M_\odot/\mathrm{pc}^3$ (Fig. 41). The Hernquist profile too shows that equally good fits can be obtained for a range of values of R_0 and M_0 (Fig. 45).

One final point that needs to be made about the χ^2 landscape plots relates to the uncertainties in the mass model fit parameters given in Table 4. The error bars quoted by ROTMAS for each of the parameters do not necessarily encompass all of the possible best-fit values. Due to the shape of the contours in the plots, the uncertainty is taken to be the best-fit value $\pm$ the value it takes to bring the parameter to the interior (horizontally or vertically) of the 1σ contour. This means that all of the values within the listed error are within 1σ but not all parameter fits within 1σ are found within those error bars. For example, Table 4 gives a value of $c = 24.45 \pm 2.35$ but the 1σ contour in Fig. 49 shows c ranging from ~ 21.5 to ~ 30.

It would be equally unsatisfactory if ROTMAS returned uncertainties corresponding to the absolute minimum and maximum values. If that were the case, all values within 1σ would be within the error bars, but not all values within the error bars would be representative of 1σ result. We are therefore able to make a statement about the practicality of the contour plots over error bars when the parameters are correlated; the contours provide us with much more information than the error bars, and caution should be taken when interpreting the derived uncertainties for the parameters.

6.3 Submaximal Disks

Column 5 of Table 4 shows the best-fitting m_d for each halo fit as a percentage of the maximum disk mass-to-light ratio. With this definition, a maximum disk fit would

have a value of 100%. As was discussed in §1.3, historically galaxies were modelled with a maximum disk but there is controversy as about whether disks in galaxies are actually maximal or not. In the case of NGC 6503, the NFW, Isothermal, and Hernquist models all produce significantly submaximal disks. Even at the extreme end of the range in m_d allowed by the data (up to $\sim 3\sigma$ in the χ^2 landscape plots), the mass-to-light ratios are barely maximal. When considering parameter fits within 1σ, no values in any of the 3 halo profiles exceed $m_d = 0.20\ M_\odot/L_{\odot,K}$ which corresponds to a ~75% maximum disk. The approximate upper value of m_d constrained by the 1σ contours, (described in §6.2) consistent with all three profiles, is ~0.15 $M_\odot/L_{\odot,K}$. This value corresponds to a ~56% maximum disk. This coincides very well with the results of Dutton et al. (2005) who, for a sample of six galaxies, find an average of 60% maximum disks at 2.2 disk scale lengths. Other independent studies also suggest that HSB galaxies have, on average, 60% maximal disks (Bottema (1993), Bottema (1997); Courteau and Rix (1999); Trott and Webster (2002) for example).

If we fit our data for the three different halo profiles, while keeping a 60% maximal disk (setting $m_d = 0.161\ M_\odot/L_{\odot,K}$ as a fixed parameter in the mass model fits) we get $\chi^2_{\rm r,min}$ = 1.27, 1.02, and 1.41 for the Hernquist, Isothermal, and NFW profiles respectively. These values of $\chi^2_{\rm r,min}$ are not statistically different from those presented in Table 4 (with the exception of the NFW fit which is statistically different at approximately the 2σ level). When we fix the mass-to-light ratio to the maximum disk value ($m_d = 0.268\ M_\odot/L_{\odot,K}$) we get considerably lower quality fits, with $\chi^2_{\rm r,min}$ = 4.86, 3.30, and 4.98 for the Hernquist, Isothermal, and NFW fits respectively. When these $\chi^2_{\rm r,min}$ values are compared to those in column 6 of Table 4 we see that a submaximal disk is strongly preferred for NGC 6503.

6.4 Comparison to Theory and Recent Work

As was shown in §1.4, McGaugh et al. (2007) gives an overview of the discrepancy between the halo profile parameters inferred from observations and the predictions for NFW halos. McGaugh et al. (2007) show that when maximum disks are adopted, only for low values of V_{200} do predictions and observations coincide. For larger values of V_{200} the concentration parameter, c, obtained by mass modelling, is

significantly lower than the values predicted by the current cosmology (as is seen in Fig. 7). Other factors such as adiabatic contraction (introduced in §5.3.4) do little to resolve this problem, as they would in fact further lower the concentration parameter. In order to compare our modelled values with the predicted and observed parameters of McGaugh et al. (2007) we over-plot the best-fitting values for V_{200} and c for NGC 6503 on Fig. 7. The result is shown in Fig. 53.

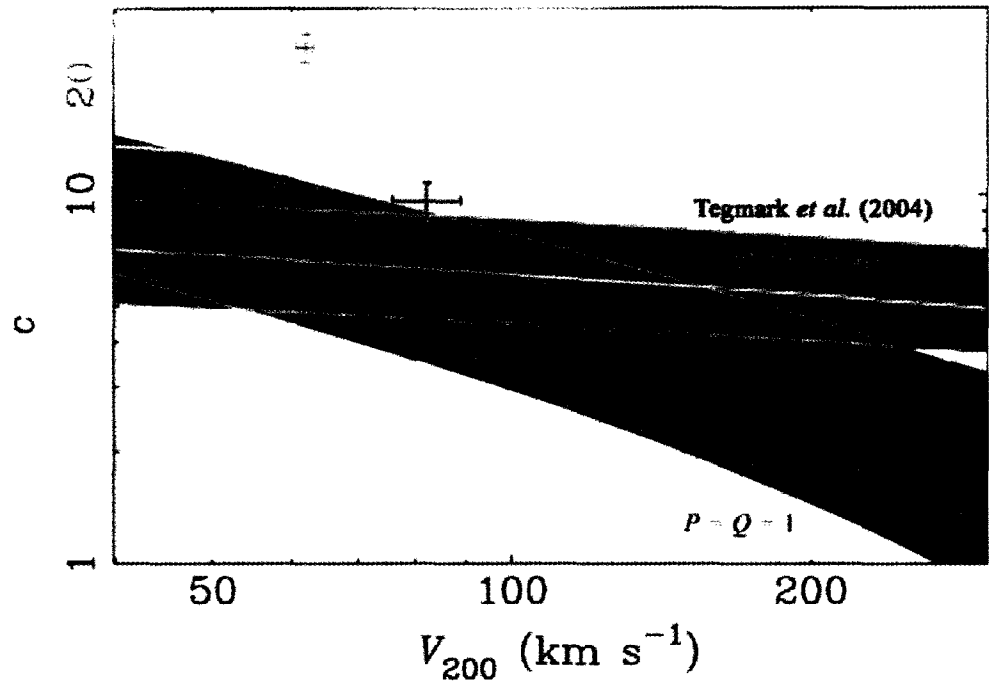

Figure 53 Figure 10 from McGaugh et al. (2007) with our best-fitting values for the NFW halo profile overplotted (green error bars). The black error bars in the centre of the observed and predicted values represents c and V_{200} obtained if m_d is fixed to the maximum disk value in ROTMAS and the error bars at the top of the plot show the value obtained if m_d is allowed to vary. See Fig. 7 for a description of the shaded regions of the plot.

Fig. 53 shows that our modelled value (in green) for the NFW parameter c lies well above both the values predicted by cosmology and the observations tabulated by McGaugh et al. (2007). This is particularly interesting since currently the measured values for c are usually on the low side and we are seeing the opposite. In fact, our values for the concentration parameter can be considered an upper limit for NGC 6503. As was discussed by McGaugh et al. (2007) and alluded to in §1.4 most current observational and model uncertainties have the effect of lowering the value of c for

a given V_{200}. Since adiabatic contraction leads to a more concentrated dark matter halo, this too results in a lower value for the concentration parameter in an NFW halo, further supporting the idea that our value for c is an upper limit (see §5.3.4). When adiabatic contraction and other effects are taken into consideration, the value of c may well be brought down to the range predicted by cosmology.

Recall that McGaugh et al. (2007) assumed a maximum disk when determining V_{200} and c for their sample, whereas we allowed for submaximal disks (which turned out to be the preferred case). Allowing for lower values for the mass-to-light ratio increases the concentration value for a given V_{200}, which can be seen in Fig. 48. In order to show that our fits do in fact correspond well with the McGaugh et al. (2007) predictions, we have also included the approximate c and V_{200} values for NGC 6503 when we fixed the mass-to-light ratio to that of the maximum disk. This is shown in Fig. 53 as the black lines and error bars near the centre of the plot. These values are still slightly high for both the predicted and observed values presented by McGaugh et al. (2007). One of the main conclusions that can be drawn from this is that allowing for submaximal disks in mass modelling can significantly raise the value of c for a given V_{200}. This could be particularly useful for high mass (high V_{200}) systems where values of c are consistently lower than predictions. In these regions allowing for submaximal disks may increase the value of c, thereby lowering the discrepancy between predictions and observations.

Although our best fitting value for c for the value of V_{200} is not significantly lower than the predicted values, this does not mean that our values are necessarily consistent with cosmology. In fact, our value of c is still much higher than the cosmology would predict. However it is plausible that additional physics not included in this thesis (effects such as adiabatic contraction) would lower our upper limit for c. By contrast, a low value of c with respect to cosmological predictions is much harder to reconcile by invoking additional physics. We can therefore conclude that although not currently consistent with cosmology, our data does not rule out a cosmologically motivated dark matter halo for NGC 6503.

Begeman et al. (1991) fit three-parameter dark matter halos to a sample of 10 galaxies with a range of luminosities, including NGC 6503. The mass-to-light

ratios solved by Begeman et al. (1991) are not directly comparable to ours due the difference in photometric band, but we can still see from their Fig. 1 that they too find a submaximal disk in their three parameter fits. However, our fits are visibly more submaximal than that found by Begeman et al. (1991). This gives further evidence towards our argument that NGC 6503 is better fit by a submaximal disk.

More recently, Puglielli et al. (2010) constructed dynamical models of NGC 6503 through the use of Bayesian statistics and Markov chain Monte Carlo techniques. Although a direct comparison with their mass-to-light ratios is not possible, due to their use of R and I band photometry, something can be said about their maximality. Three of the four of their considered scenarios (an inner truncated disk, an exponential disk with dust, a model where gas traces the gravitational potential, and a model in which the true underlying disk scale length is revealed in the outermost portion of the surface brightness profile) show a noticeably submaximal disk (see Fig. 5 of Puglielli et al., 2010) and the fourth model can be ruled out using stability arguments. They also adopt a slightly different form of the NFW halo (one where α in Eq. 9 is allowed to vary), making a direct comparison of the halo parameters difficult. However, they too obtain acceptable fits to the data with a cosmologically motivated dark matter halo, thereby strengthening one of our main conclusions that observations of NGC 6503 do not exclude models derived from cosmological simulations.

Our work is in agreement with previous studies in finding that a submaximal disk is preferred for NGC 6503. However, in our study we have now ruled out significant non-circular motions, have high quality optical data, and have eliminated issues concerning beam smearing and extinction. Comparing with the plots in McGaugh et al. (2007), we see that the data allow a much higher c than with maximum disk fits. This suggests that some of the discrepancies between theory and observations in disk galaxies can be solved if disks are submaximal at the high mass end.

7 Chapter 7 - Conclusions and Future Work

In this thesis we performed an in-depth study of the nearby, late-type spiral galaxy, NGC 6503. There were three key science goals of this thesis. First, we aimed to measure a reliable rotation curve for the system. Second, we explored the extent to which the mass-to-light ratio, m_d, of the galaxy could be constrained through mass modelling. Finally, for a given constraint on m_d, we determined whether the halo profile for NGC 6503 is consistent with cosmological predictions. In order to derive a reliable rotation curve, a comprehensive search for non-circular motions on our 2 Hα, H I, and CO datasets was performed using Velfit (§3). An extended surface brightness profile in the K-band (to trace the old stellar population and minimize the effects of dust extinction) was derived in §4. In §5 we attempted to constrain m_d (and halo parameters) through mass modelling with the Isothermal, Hernquist, and NFW profiles.

The detailed search for non-circular motions in the 4 kinematic datasets revealed no coherent radial or bisymmetric flows for NGC 6503. Any non-circular motions that are present are likely to be incoherent and at such a small scale that they should not bias the derived rotation curve. Having confirmed that coherent non-circular motions are not an issue in any of the datasets and that the datasets were coincident (Fig. 31) we combined them to form one master, multi-wavelength rotation curve.

A suite of mass models was evaluated in §5 to constrain the stellar mass-to-light ratio and dark matter halo properties in NGC 6503. The Isothermal profile provided the best fit to the data statistically but we were able to conclude that the cosmologically motivated NFW halo is also allowed by the data. We found that our constraints on m_d from the Isothermal, Hernquist, and NFW halos all suggest that a submaximal disk is strongly preferred for NGC 6503. Finally, we find that our value for the modelled NFW halo parameter c (for a given V_{200}) is larger than both those predicted by cosmology and the observations tabulated by McGaugh et al. (2007). Given that our value for c is an upper limit, once effects such as adiabatic contraction are taken into consideration the halo properties of NGC 6503 may be consistent with cosmological predictions.

Although our cursory investigation suggested that halo contraction was not important (§5.3.4), further work needs to be done to determine more accurately the effects of adiabatic contraction on the dark matter halo of NGC 6503. In order to understand the current state of the galaxy we need to determine the physical characteristics of the galaxy before adiabatic contraction compressed the halo. Carrying out a suite of calculations with the contra package (Gnedin et al., 2004) would be a good first step in this regard.

Further attention is also needed to study the mass modelling results using MOND. As was seen in §5.3.5 and discussed above, MOND was the only model not well able to reproduce the observed data (at least compared to the other three fits). This alone is justification for further study into why this is the case. MOND is known for its surprising ability to reproduce observed rotation curve data very well, but here we do not find that to be the case. A first look at this suggests that the falling rotation curve in NGC 6503 is the culprit since the MOND model prefers a rising one (Fig. 52). Further investigation into what makes NGC 6503 a unique case in this sense is needed.

Finally, mass modelling, such as that performed in this thesis, makes no requirement that the best fitting models produced be self consistent or stable with time. In order to verify that our solutions are stable, N-body simulations, such as those presented in Puglielli et al. (2010), should be run. If simulations with our best fitting model parameters give rise to a bar in the inner regions of the galaxy, the stability of this solution is in question (since we do not observe a significant bar in NGC 6503). In order for us to consider our best fitting models as accurate parameterizations of this galaxy, these simulations to check for stability need to be run.

References

Barazza, F., S. Jogee, and I. Marinova (2008). Bars in Disk-dominated and Bulge-dominated Galaxies at z=0: New Insights from 3600 SDSS Galaxies. *Astrophysical Journal 675*, 1194–1212.

Begeman, K., A. Broeils, and R. Sanders (1991). Extended Rotation Curves of Spiral Galaxies-Dark Haloes and Modified Dynamics. *Monthly Notices of the Royal Astronomical Society 249.*

Bell, E. and R. de Jong (2001). Stellar Mass-to-Light Ratios and the Tully-Fisher Relation. *The Astrophysical Journal 550*, 212–229.

Binney, J. and M. Merrifield (1998). *Galactic astronomy.* Princeton Univ Pr.

Blumenthal, G., S. Faber, R. Flores, and J. Primack (1986). Contraction of Dark Matter Galactic Halos due to Baryonic Infall. *Astrophysical Journal 301*(Part 1).

Bosma, A. (1978). The Distribution and Kinematics of Neutral Hydrogen in Spiral Galaxies of Various Morphological Types. *Groningen Univ., (1978).*

Bosma, A. (1981). 21-cm Line Studies of Spiral Galaxies. II. The Distribution and Kinematics of Neutral Hydrogen in Spiral Galaxies of Various Morphological Types. *The Astronomical Journal 86*, 1825.

Bottema, R. (1989). The Stellar Velocity Dispersion of the Spiral Galaxies NGC 6503 and NGC 6340. *Astronomy and Astrophysics (ISSN) 221*(2), 236–249.

Bottema, R. (1993). The Stellar Kinematics of Galactic Disks. *Astronomy and Astrophysics 275*, 16–16.

Bottema, R. (1997). The Maximum Rotation of a Galactic Disc. *Astronomy and Astrophysics 328.*

Bullock, J. S., A. Dekel, T. S. Kolatt, A. V. Kravtsov, A. A. Klypin, C. Porciani, and J. R. Primack (2001, July). A Universal Angular Momentum Profile for Galactic Halos. *The Astrophysical Journal 555*, 240–257.

Courteau, S. (1996). Deep R-Band Photometry for Northern Spiral Galaxies. *Astronomy and Astrophysics Supplement Series 103*(2), 363–426.

Courteau, S. and H. Rix (1999). Maximal Disks and the Tully-Fisher Relation. *The Astrophysical Journal 513*, 561–571.

De Blok, W. and S. McGaugh (1997). The Dark and Visible Matter Content of Low Surface Brightness Disc Galaxies. *Monthly Notices of the Royal Astronomical Society 290*, 533–552.

de Vaucouleurs, G., A. de Vaucouleurs, H. Corwin Jr, R. Buta, G. Paturel, and P. Fouque (1991a). *Third Reference Catalogue of Bright Galaxies*. Springer-Verlag New York.

de Vaucouleurs, G., A. de Vaucouleurs, H. Corwin Jr, R. Buta, G. Paturel, and P. Fouque (1991b). *Third Reference Catalogue of Bright Galaxies*. Springer-Verlag New York.

Dutton, A., S. Courteau, R. de Jong, and C. Carignan (2005). Mass Modeling of Disk Galaxies. *The Astrophysical Journal 619*, 218–242.

Épinat, B., P. Amram, M. Marcelin, C. Balkowski, O. Daigle, O. Hernandez, L. Chemin, C. Carignan, J. Gach, and P. Balard (2008). GHASP: an Ha kinematic survey of spiral and irregular galaxies-VI. New Ha data cubes for 108 galaxies. *Monthly Notices of the Royal Astronomical Society 388*(2), 500–550.

Freeland, E., L. Chomiuk, R. Keenan, and T. Nelson (2010). Evidence for a Strong End-On Bar in the Ringed Sigma-Drop Galaxy NGC 6503. *The Astronomical Journal 139*, 865–870.

Gentile, G., P. Salucci, U. Klein, D. Vergani, and P. Kalberla (2004). The Cored Distribution of Dark Matter in Spiral Galaxies. *Monthly Notices of the Royal Astronomical Society 351*, 903–922.

Gnedin, O., A. Kravtsov, A. Klypin, and D. Nagai (2004). Response of Dark Matter Halos to Condensation of Baryons: Cosmological Simulations and Improved Adiabatic Contraction Model. *Astrophysical Journal 616*, 16–26.

Greisen, E., K. Spekkens, and G. Van Moorsel (2009). Aperture Synthesis Observations of NGC 6503. *The Astronomical Journal 137*, 4718–4733.

Héraudeau, P. and F. Simien (1996). Optical and i-band surface photometry of spiral galaxies.i. the data. *Astronomy and Astrophysics Supplement Series 118*(111–155).

Hernquist, L. (1990). An Analytical Model for Spherical Galaxies and Bulges. *Astrophysical Journal 356*, 359–364.

Jarrett, T., T. Chester, R. Cutri, S. Schneider, and J. Huchra (2003). 2MASS Large Galaxy Atlas. *The Astronomical Journal 125*, 525–554.

Karachentsev, I. and M. Sharina (1997). Distance to the Spiral Galaxy NGC 6503 Situated in the Local Void. *Astronomy and Astrophysics 324*, 457–460.

Komatsu, E., J. Dunkley, M. Nolta, C. Bennett, B. Gold, G. Hinshaw, N. Jarosik, D. Larson, M. Limon, L. Page, et al. (2009). WMAP Five-Year Observations: Cosmological Interpretation. *The Astrophysical Journal Supplement Series 180*, 330–376.

Lira, P., R. Johnson, A. Lawrence, and R. Fernandes (2007). Multiwavelength Study of the Nuclei of a Volume-Limited Sample of Galaxies–II. Optical, Infrared and Radio Observations. *Monthly Notices of the Royal Astronomical Society: Letters 382*(4), 1552–1590.

Loveday, J. (1996). The APM Bright Galaxy Catalogue. *Monthly Notices of the Royal Astronomical Society 278*(4), 1025–1048.

McDonald, M., S. Courteau, and R. Tully (2009). Bulge-Disc Decompositions and Structural Bimodality of Ursa Major Cluster Spiral Galaxies. *Monthly Notices of the Royal Astronomical Society 393*(2), 628–640.

McGaugh, S., W. de Blok, J. Schombert, R. de Naray, and J. Kim (2007). The Rotation Velocity Attributable to Dark Matter at Intermediate Radii in Disk Galaxies. *The Astrophysical Journal 659*, 149–161.

McGaugh, S. S. (2005). Balance of dark and luminous mass in rotating galaxies. *Phys. Rev. Lett. 95*(17), 171302.

Milgrom, M. (1983). A Modification of the Newtonian Dynamics as a Possible Alternative to the Hidden Mass Hypothesis. *Astrophysical Journal 270*, 365–370.

Navarro, J., C. Frenk, and S. White (1997). Hierarchical Clustering. *The Astrophysical Journal 490*, 493–508.

Palunas, P. and T. Williams (2000). Maximum Disk Mass Models for Spiral Galaxies. *Astronomical Journal 120*, 2884–2903.

Peebles, P. and B. Ratra (2003). The Cosmological Constant and Dark Energy. *Reviews of Modern Physics 75*(2), 559–606.

Press, W., S. Teukolsky, W. Vetterling, and B. Flannery (1992). *Numerical Recipes in FORTRAN: the Art of Scientific Computing*. Cambridge Univ Pr.

Puglielli, D., L. Widrow, and S. Courteau (2010). Dynamical Models for NGC 6503 using a Markov Chain Monte Carlo Technique. *Arxiv preprint arXiv:1002.0819*.

Rhee, G., O. Valenzuela, A. Klypin, J. Holtzman, and B. Moorthy (2004, December). The Rotation Curves of Dwarf Galaxies: A Problem for Cold Dark Matter? *Astrophysical Journal 617*, 1059–1076.

Rubin, V., N. Thonnard, and W. Ford (1980). Rotational Properties of 21 SC Galaxies with a Large Range of Luminosities and Radii, from NGC 4605/R= 4 kpc/ to UGC 2885/R= 122 kpc. *The Astrophysical Journal 238*, 471–487.

Sackett, P. (1997). Does the Milky Way have a Maximal Disk? *The Astrophysical Journal 483*, 103–110.

Salucci, P. (2001). The Constant-Density Region of the Dark Haloes of Spiral Galaxies. *Monthly Notices of the Royal Astronomical Society 320*, L1–L5.

Sanders, R. and S. McGaugh (2002). Modified Newtonian Dynamics as an Alternative to Dark Matter. *Annual Review of Astronomy and Astrophysics 40*(1), 263–317.

Schoenmakers, R. H. M., M. Franx, and P. T. de Zeeuw (1997). Measuring Non-Axisymmetry in Spiral Galaxies. *Monthly Notices of the Royal Astronomical Society 292*.

Schoenmakers, R. H. M. and R. A. Swaters (1999, August). Kinematic Lopsidedness in Spiral Galaxies. In D. R. Merritt, M. Valluri, & J. A. Sellwood (Ed.), *Galaxy Dynamics - A Rutgers Symposium*, Volume 182 of *Astronomical Society of the Pacific Conference Series*.

Sellwood, J. and R. Sanchez (2009). Quantifying Non-circular Streaming Motions in Disc Galaxies.

Simon, J., A. Bolatto, A. Leroy, L. Blitz, and E. Gates (2005). High-Resolution Measurements of the Halos of Four Dark Matter-Dominated Galaxies: Deviations from a Universal Density Profile1. *The Astrophysical Journal 621*, 757–776.

Simon, J. D., A. D. Bolatto, A. Leroy, L. Blitz, and E. L. Gates (2005). High-Resolution Measurements of the Halos of Four Dark Matter-Dominated Galaxies: Deviations from a Universal Density Profile. *ApJ 621*, 757–776.

Sparke, L. and J. Gallagher (2007). *Galaxies in the Universe: an Introduction*. Cambridge Univ Pr.

Spekkens, K., R. Giovanelli, and M. P. Haynes (2005). The Cusp/Core Problem in Galactic Halos: Long-Slit Spectra for a Large Dwarf Galaxy Sample. *The Astrophysical Journal 129*, 2119–2137.

Spekkens, K. and J. Sellwood (2007). Modeling Noncircular Motions in Disk Galaxies: Application to NGC 2976. *The Astrophysical Journal 664*, 204–214.

Spergel, D., R. Bean, O. Dore, M. Nolta, C. Bennett, J. Dunkley, G. Hinshaw, N. Jarosik, E. Komatsu, L. Page, et al. (2006). Wilkinson Microwave Anisotropy Probe (WMAP) Three Year Results: Implications for Cosmology. *Astrophysical Journal Supplement Series 170*, 377–408.

Swaters, R. A., B. F. Madore, F. C. van den Bosch, and M. Balcells (2003, February). The Central Mass Distribution in Dwarf and Low Surface Brightness Galaxies. *Astrophysical Journal 583*, 732–751.

Tegmark, M., M. Blanton, M. Strauss, F. Hoyle, D. Schlegel, R. Scoccimarro, M. Vo-

geley, D. Weinberg, I. Zehavi, A. Berlind, et al. (2004). 3D Power Spectrum of Galaxies from SDSS. *The Astrophysical Journal 606*, 702–740.

Thilker, D., L. Bianchi, G. Meurer, A. Gil de Paz, S. Boissier, B. Madore, A. Boselli, A. Ferguson, J. Muñoz-Mateos, G. Madsen, et al. (2007). XUV-Disk Galaxies in the Local Universe. *The Astrophysical Journal Supplement Series 173*, 538–571.

Trott, C. M. and R. L. Webster (2002). Dissecting a galaxy: Mass Distribution of 2237+0305. *Monthly Notices of the Royal Astronomical Society 334*, 621–630.

Valenzuela, O., G. Rhee, A. Klypin, F. Governato, G. Stinson, T. Quinn, and J. Wadsley (2007). Is There Evidence for Flat Cores in the Halos of Dwarf Galaxies? The Case of NGC 3109 and NGC 6822. *Astrophysical Journal 657*, 773–789.

van Albada, T. S., J. N. Bahcall, K. Begeman, and R. Sancisi (1985). Distribution of Dark Matter in the Spiral Galaxy NGC 3198. *Astrophysical Journal 295*, 305–313.

Van der Hulst, J., J. Terlouw, K. Begeman, W. Zwitser, and P. Roelfsema (1992). The Groningen Image Processing System, GIPSY. In *Astronomical Data Analysis Software and Systems I, ed. DM Worall, C. Biemesderfer, & J. Barnes, ASP Conf. Ser*, Volume 25, pp. 131.

Weiner, B., J. Sellwood, and T. Williams (2001). The Disk and Dark Halo Mass of the Barred Galaxy NGC 4123. ii. Fluid-Dynamical Models. *The Astrophysical Journal 546*, 931–951.